*Technical Physics Letters, Vol. 26, No. 5, 2000, pp. 357–359. Translated from Pis'ma v Zhurnal Tekhnicheskoĭ Fiziki, Vol. 26, No. 9, 2000, pp. 1–6.*


# Pulsed Microwave Radiator for the Band System λ = 175 nm ArCl(B–X)/236 nm XeCl(D–X)/258 nm $Cl_2^*$/308 nm XeCl(B–X)

**A. K. Shuaibov**

*Uzhgorod State University, Uzhgorod, 214000 Ukraine*

Received October 12, 1999

**Abstract**—Parameters of a multiwave radiator pumped with transverse volume discharge in an Ar–Xe–$Cl_2$ mixture at a pressure of $P$ = 5–30 kPa were optimized. It is shown that, at a partial xenon pressure in the mixture below 0.4 kPa, the discharge may serve a multiwave radiation source operating on the electron-vibrational transitions with λ = 175 nm ArCl(B–X), 236 nm XeCl(D–X), 258 nm $Cl_2$(D'–A'), and 308 nm XeCl(B–X). The emission line intensities have comparable values, which may be of interest for applications in the short-wave pulsed photometry, microelectronics, and photochemistry. *© 2000 MAIK "Nauka/Interperiodica".*

At present, the excimer lamps using halides of inert gases RX* (R = Ar, Kr, Xe; X = F, Cl) excited by transverse volume discharge (TVD) offer most powerful and comparatively simple sources of spontaneous radiation pulses of submicrosecond duration [1]. Most developed are the pulsed electric-discharge radiators operating within fixed bands in the region of λ = 222 nm KrCl and 308 XeCl. The working media of these radiators use predominantly HCl as the chlorine carrier and He or Ne as the buffer gases [2, 3].

Recently [4], a TVD-pumped excimer lamp operating in a multiwave regime has been developed for a system of bands at 353 nm XeF/308 nm XeCl/249 nm KrF/222 nm KrCl using He–Kr–Xe–$SF_6$–HCl working gas media or $CF_2Cl_2$ molecules as the common carriers of chlorine and fluorine for the RX* formation [5]. To the present, multiwave radiators operating in a wider wavelength range (including vacuum ultraviolet) were not described.

Below, we report on the results of optimization of a multiwave excimer radiator for the vacuum ultraviolet (VUV) range, which employs an Ar–Xe–$Cl_2$ gas mixture. A special feature of this working medium is that the halogen molecule proper is a rather effective source of radiation with λ = 258 nm $Cl_2$(D'–A'), possessing a minimum intrinsic absorption in the region of λ < 200 nm. In addition, the plasma formed upon the RX* molecule formation features increasing role of the "harpooning" reaction R($m$) + $Cl_2$ ⟶ RCl* + Cl, where R($m$) denotes the inert gas atom in a metastable state [6].

The discharge was initiated in the TVD-pumped radiator described elsewhere [7]. The discharge plasma occupied a volume of $18 \times 2.2 \times 1.0$ cm$^3$, in which TVD was induced by a two-loop $LC$ circuit with automated spark preionization provided by a TGI1–1000/25 commutator. The storage battery was composed of capacitors of the K15–10 type (40 kV, 10 nF) and had a total capacitance of 30 nF. The differentiating capacitor comprised 20 capacitors of the KVI-3 type (20 kV, 470 pF). Emission from the TVD plasma was monitored using an 0.5-m vacuum monochromator equipped with a 1200 mm$^{-1}$ grating. The radiation was detected with a FEU-142 phototube (LiF window), the working wavelength range of the spectrophotometer extending from 130 to 350 nm. The setup was calibrated in the 165–350 nm region with respect to the $H_2$ continuum.

Figure 1 shows a typical emission spectrum of the TVD plasma in an Ar–Xe–$Cl_2$ gas mixture plotted without correction for the spectral sensitivity of the vacuum monochromator–phototube system. As seen, the UV–VUV range is represented by the simultaneous emissions at λ = 175 nm ArCl(B–X), 236 nm XeCl(D–X), 258 nm $Cl_2$(D'–A'), and 308 nm XeCl(B–X). By selecting an optimum gas mixture composition, the intensity of transitions in the ArCl, $Cl_2^*$, and XeCl molecules can be leveled.

We have studied the intensity of emission in the bands of ArCl(B– X) and $Cl_2$(D'–A') as function of the chlorine content and total pressure using TVD in the Ar–$Cl_2$ mixture. The experimental results showed that the optimum partial pressure of $Cl_2$ molecules (for $U_{charge}$ < 14 kV) falls within 0.2–0.4 kPa, while the total pressure of the double mixture exhibit a broad maximum at $P$ = 8–15 kPa. Further increase in the pressure detrimentally affected the discharge homogeneity. Subsequent optimization of the working mixture composition was performed at $P$ = 13.3 kPa.

1063-7850/00/2605-0357$20.00 © 2000 MAIK "Nauka/Interperiodica"

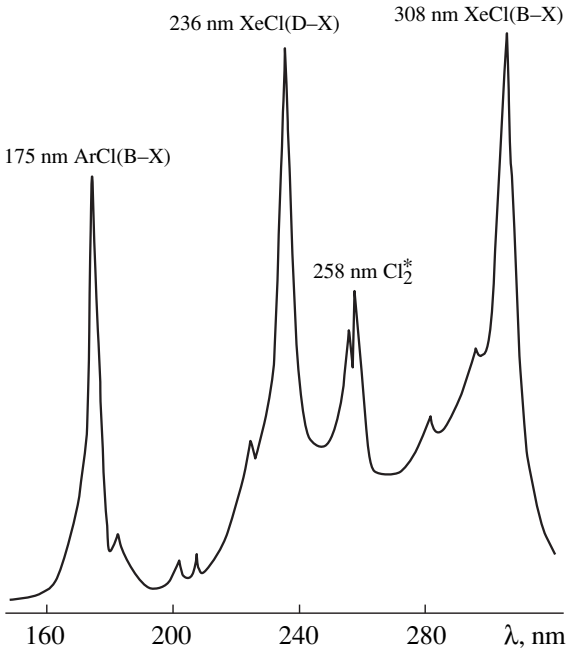


**Fig. 1.** Typical emission spectrum of TVD plasma in an Ar–Xe–$Cl_2$ mixture with the partial pressures 13.3, 0.4, and 0.24 kPa, respectively.

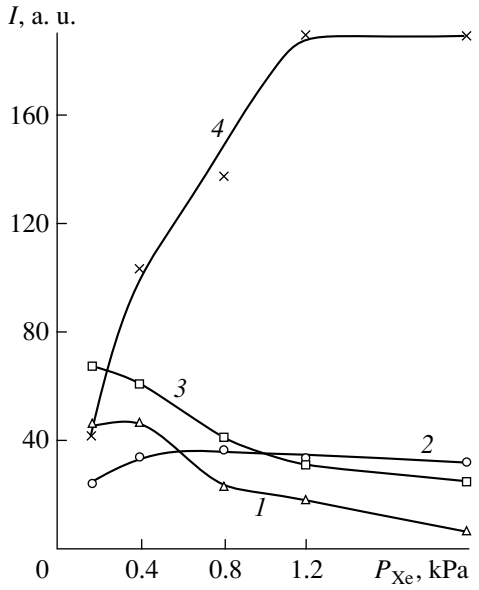


**Fig. 2.** The plot of emission intensity versus xenon partial pressure for the transitions with λ = 175 nm ArCl(B–X) (*1*), 236 nm XeCl(D–X) (*2*), 258 nm $Cl_2$(D'–A') (*3*), and 308 nm XeCl(B–X) (*4*) in an Ar–Xe–$Cl_2$ mixture with the partial pressures [Ar] = 13.3 kPa and [$Cl_2$] = 0.24 kPa ($U_{charge}$ = 12.5 kV).

Figures 2 and 3 show the plots of emission intensity versus Xe content in the mixture and the number of TVD pulses for the bands of ArCl(B–X), $Cl_2$(D'–A'), and XeCl(D, B–X). As seen from Fig. 2, the multiwave regime of the radiator with close values of the band intensities is realized at a xenon partial pressure in the range [Xe] = 0.15–0.4 kPa. When [Xe] = 0.2 kPa, the bands at 308 nm XeCl and 258 nm $Cl_2^*$ have equal intensities, while the emission from ArCl(B–X) and XeCl(D–X) is lower by a factor of 2–3. Increase in the xenon content above 0.4 kPa leads to a sharp growth of the emission at 308 nm XeCl(B–X) and a drop in the intensity of ArCl(B–X) and $Cl_2$(D'–A') transitions. The characteristic operating life for these transitions (i.e., the time after which the emission intensity decreases by half) is not less than (2–3) × $10^4$ pulses. The plot of intensity versus charging voltage for the bands of RCl* and $Cl_2^*$ is linear (for $U_{charge}$ = 4–12 kV, whereby the intensity increases by a factor of 3–5.

Physical processes most strongly affecting the formation of XeCl(D, B–X) and ArCl(B–X) molecules in plasma in the Ar–Xe–$Cl_2$ gas mixture include the reaction of energy transfer from metastable Ar atoms to Xe [8, 9] and the excitation of Xe atoms. For the plasma studied in this work (in contrast to the active media of high-pressure excimer lamps), the role of the recombination reaction $Ar^+(Xe^+) + Cl^- + (Ar) \longrightarrow ArCl^*(XeCl^*) + (Ar)$ decreases because the rate of this process drops (from $10^{-6}$ to $10^{-7}$ $cm^3/s$) in proportion to the buffer gas pressure (reduced from 100 to 10 kPa) [10]. In the initial TVD stage, the maximum contribution is due to the "harpooning" process of the type Xe(*m*) + $Cl_2 \longrightarrow XeCl + Cl$ [6] determined by the presence of excited atoms in the medium. The mechanisms of formation of RCl* and $Cl_2^*$ will be studied in more detail using high-resolution plasma emission spectroscopy.

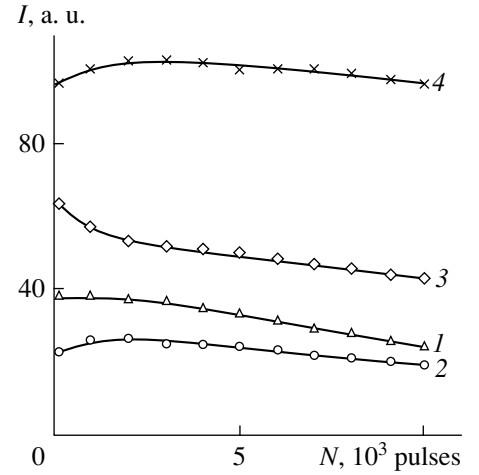


**Fig. 3.** The plot of emission intensity versus number of TVD pulses for the transitions with λ = 175 nm ArCl(B–X) (*1*), 236 nm XeCl(D–X) (*2*), 258 nm $Cl_2$(D'–A') (*3*), and 308 nm XeCl(B–X) (*4*) in an Ar–Xe–$Cl_2$ mixture with the partial pressures [Ar] = 13.3 kPa, [Xe] = 0.4 kPa, and [$Cl_2$] = 0.24 kPa ($U_{charge}$ = 12.5 kV).

Thus, we have developed a multiwave excimer radiator operating on the transitions with $\lambda$ = 175 nm ArCl(B–X), 236 nm XeCl(D–X), 258 nm $Cl_2^*$, and 308 nm XeCl(B–X) using medium-pressure TVD plasma. For the optimum partial pressure of chlorine (0.3–0.4 kPa), total gas pressure (10–20 kPa), and xenon pressure (0.15–0.4 kPa), the operating life of the radiator exceeds $(2–3) \times 10^4$ emission pulses.

The author is grateful to A.I. Dashchenko for his help in conducting experiments.

## REFERENCES

1. B. A. Koval', V. S. Skakun, V. F. Tarasenko, *et al.*, Prib. Tekh. Éksp., No. 4, 244 (1992).
2. V. A. Vizir', V. S. Skakun, É. A. Sosnin, *et al.*, Kvantovaya Élektron. **22**, 519 (1995).
3. A. N. Panchenko, É. A. Sosnin, and V. F. Tarasenko, Zh. Tekh. Fiz. **67**, 78 (1997) [Tech. Phys. **42**, 68 (1997)].
4. A. K. Shuaibov, Zh. Tekh. Fiz. **68**, 64 (1998) [Tech. Phys. **43**, 1459 (1998)].
5. A. K. Shuaibov, L. L. Shimon, and I. V. Shevera, Prib. Tekh. Éksp., No. 3, 142 (1998).
6. E. B. Gordon, V. G. Egorov, V. T. Mikhkel'soo, *et al.*, Kvantovaya Élektron. **15**, 285 (1988).
7. A. K. Shuaibov, Kvantovaya Élektron. **26**, 128 (1999).
8. C. H. Chen, I. P. Judish, and M. G. Payne, J. Phys. B: At. Mol. Phys. **11**, 2189 (1978).
9. I. Galy, K. Aouame, A. Birot, *et al.*, J. Phys. B: At. Mol. Opt. Phys. **26**, 477 (1993).
10. M. R. Flannery, in *Gas Lasers*, Ed. by E. McDaniel and W. Nighan (Academic Press, New York, 1982; Mir, Moscow, 1986).

*Translated by P. Pozdeev*

*Technical Physics Letters, Vol. 26, No. 5, 2000, pp. 360–362. Translated from Pis'ma v Zhurnal Tekhnicheskoĭ Fiziki, Vol. 26, No. 9, 2000, pp. 7–13.*


# Laser Third Harmonic Generation in Organic Dye Vapors

**R. A. Ganeev, Sh. R. Kamalov, M. K. Kodirov, M. R. Malikov, A. I. Ryasnyanskiĭ, R. I. Tugushev, Sh. U. Umidullaev, and T. Usmanov**

*"Akadempribor" Research and Production Corporation, Academy of Sciences of the Republic of Uzbekistan, Tashkent, Uzbekistan*

*Samarkand State University, Samarkand, 703005 Uzbekistan*

Received October 14, 1999

**Abstract**—The phenomenon of nonlinear optical conversion of a YAG:Nd laser radiation frequency from IR to UV spectral range in naphthalene vapors was studied. The optimum temperature of naphthalene vapors (170°C) was found at which the pumping radiation is synchronously converted into the third harmonic emission. A mechanism of the third harmonic generation is proposed based on the difference frequency generation in a six- photon process. The efficiency of conversion to the third harmonic generation varied within $10^{-10}$–$10^{-8}$, depending on the pumping intensity and cell temperature. Nonlinear optical characteristics of naphthalene vapors were calculated for the generation using nonlinearities of the third and fifth order. © *2000 MAIK "Nauka/Interperiodica".*

Nonlinear optical properties of the vapors of organic compounds were originally studied in benzene ($C_6H_6$) vapors [1], where conversion of the initial emission into the vacuum UV range was observed, and in acetylene ($C_2H_2$) vapors [2], where the third harmonic generation of a dye laser in the UV range was obtained. Subsequent investigations showed that nonlinear susceptibilities of some organic dye molecules with conjugated double bonds are comparable with nonlinear resonance atomic susceptibilities [3, 4], which was explained by the presence of delocalized $\pi$ electrons in these organic molecules. The latter factor accounts for increasing nonlinear susceptibility of these media and makes the molecules with conjugated double bonds promising nonlinear optical materials. Note that delocalization of the $\pi$ electrons in fullerenes ($C_{60}$) also accounts for a large nonlinear susceptibility of these molecules observed in the process of harmonic generation [5, 6] and wavefront reversal [7].

Nonlinear optical characteristics of some organic dye vapors were studied and various schemes for the laser radiation frequency conversion were suggested [4, 8]. However, there are still many open questions concerning determination of the conditions of phase synchronism for the frequency conversion by different channels, the signs of dispersion in the corresponding nonlinear optical processes, the effects of various nonlinear factors on the efficiency of conversion in these media, etc.

The purpose of our investigation was to study the process of frequency conversion in organic dye vapors from IR to UV range in picosecond laser pulses,

The dipole moments and nonlinear susceptibilities of the organic dye vapors were calculated using the free electron model. According to this theory, a system of conjugated double bonds is described assuming that $\sigma$ electrons of carbon atoms, responsible for the $\sigma$-bonds, determine a molecular skeleton of definite shape. This skeleton, being positively charged, creates a potential in which all $\pi$ electrons can move freely over the whole conjugated structure. Despite a somewhat simplified character [9], the free electron model provides for a sufficiently adequate description of the systems with conjugated double bonds and calculation of their major optical (in particular, nonlinear) characteristics [10].

We have studied the process of laser third harmonic generation using naphthalene ($C_{10}H_8$) as the organic dye. This selection is explained by the fact that naphthalene has a sufficiently high vapor density already at comparatively low temperatures (~200°C), which facilitates attaining of the regime of synchronized conversion of the pumping radiation into harmonic emission.

Using the results of calculations of the energy levels, transition frequencies ($\omega_{mn}$), and dipole moments of transitions ($d_{ij}$) of naphthalene summarized in the table, we determined the value of the third-order nonlinear susceptibility $\chi^{(3)}(3\omega)$ for the third harmonic generation of a YAG:Nd laser with $\omega = 9391$ cm$^{-1}$ ($\omega + \omega + \omega \Rightarrow 3\omega$ process). The calculation was performed using the formula [11]:

$$\chi^{(3)} = \frac{1}{4\hbar^3}\sum_{n,m,l}\left[\frac{d_{gn}d_{nm}d_{ml}d_{lg}}{(\omega_{gn}-\omega)(\omega_{gm}-2\omega)(\omega_{gl}-3\omega)}\right] \quad (1)$$

and yielded the value $\chi^{(3)}(3\omega) = 0.42 \times 10^{-34}$ CGSE units.

In isotropic media, the process of the third harmonic generation may proceed, besides the $\omega + \omega + \omega \Rightarrow 3\omega$ process, by the $\omega + \omega + \omega + \omega - \omega \Rightarrow 3\omega$ channel. We

1063-7850/00/2605-0360$20.00 © 2000 MAIK "Nauka/Interperiodica"

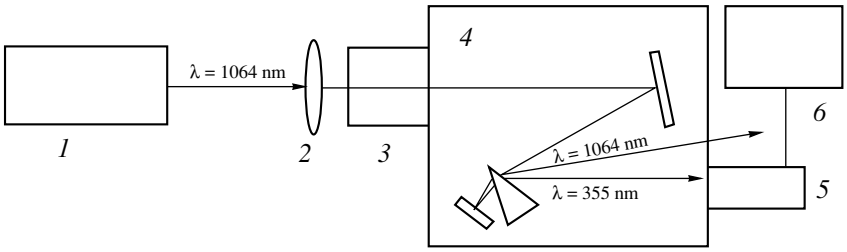


**Fig. 1.** Schematic diagram of the experiment on the third harmonic generation of a YAG:Nd laser in naphthalene vapors: (*1*) YAG:Nd laser; (*2*) focusing lens; (*3*) optical cell with naphthalene vapors; (*4*) spectrograph; (*5*) FEU-106 phototube; (*6*) V4-17 voltmeter.

have calculated the fifth-order nonlinear susceptibility for the latter process by analogy with the above third-order parameter and obtained $\chi^{(5)}(3\omega) = 1.3 \times 10^{-46}$ CGSE units.

The initial radiation was generated by a YAG:Nd laser producing a train of picosecond pulses [12] with the following characteristics: pulse train energy, 5 mJ; number of pulses, 7; pulse duration, 35 ps. The laser radiation was focused by a lens with a focal distance of 25 cm into the center of a gas cell containing dye vapors (Fig. 1). The cell comprised a stainless steel cylinder with entrance and exit quartz windows in the edge flanges. The cell was provided with heating and cooling systems. The dye vapor pressure was determined by measuring a temperature inside the cell with a thermocouple and using a calibration curve of vapor pressure versus temperature. The nonlinear optical medium was represented by naphthalene ($C_{10}H_8$) vapors obtained by heating the cell to 220°C, which corresponded to a naphthalene molecule concentration of $N \sim 10^{18}$ cm$^{-3}$. The pumping radiation and third harmonic emission were extracted via an exit window and separated by an ISP-30 spectrograph. The third harmonic emission ($\lambda$ = 354.7 nm) was detected by a FEU-106 phototube, the output signal of which was measured by a V4-17 voltmeter. The output third harmonic signal intensity was studied as function of the pumping radiation energy and the dye vapor temperature.

Figure 2 shows a plot of the third harmonic signal intensity versus naphthalene vapor temperature. As seen, a maximum intensity of the converted radiation was observed at a temperature of about 170°C. This behavior is typical of the regime of odd harmonic generation under the fine focusing conditions ($b \ll L_c$, $b$ = 8 mm is the confocal parameter of the focused radiation and $L_c$ = 180 mm is the pathlength in the nonlinear optical medium), observed in an isotropic nonlinear medium possessing negative dispersion or in the regime of difference frequency generation (irrespective of the sign of dispersion).

As noted above, the process of third harmonic generation in the naphthalene vapors may proceed either by the direct channel ($\omega + \omega + \omega \Rightarrow 3\omega$) or via a six-photon process of the difference frequency generation ($\omega + \omega + \omega + \omega - \omega \Rightarrow 3\omega$). A necessary condition for the synchronized third harmonic generation by the first channel using the initial radiation finely focused in a nonlinear medium is that the harmonic emission wavelength must fall within the region of negative dispersion (i.e., $k_3 - 3k_1 < 0$, where $k_3$ and $k_1$ are the harmonic and pumping wavevectors, respectively). Only this would ensure that the additional phase shift caused by the radiation passing over the region of focusing would be compensated by dispersion of the nonlinear medium. This necessary condition provides for the possibility of a synchronized transfer of the incident electromagnetic wave energy to the harmonic wave.

The region of negative dispersion may form only in a medium featuring anomalous dispersion ($dn/d\lambda > 0$) and possessing the corresponding electron transition lines. Analysis of the spectrum of single-photon absorption of naphthalene vapors shows that the wavelength region corresponding to the third harmonic generation (354.7 nm) contains no absorption bands of lines [13]. The medium exhibits normal dispersion in this region and, hence, the conditions of synchronized energy transfer by the direct channel $\omega + \omega + \omega \Rightarrow 3\omega$ in naphthalene vapors cannot be realized for a moderate

Dipole moments of transitions ($d_{ij} \times 10^{-18}$ CGSE units)

| $d_{ij}$ | 5 | 6 | 7 | 8 | 9 |
|---|---|---|---|---|---|
| 5 | 0 | 13.55073 | 0 | 1.454014 | 0 |
| 6 | 13.55073 | 0 | 13.5708 | 0 | 1.467431 |
| 7 | 0 | 13.5708 | 0 | 13.58422 | 0 |
| 8 | 1.454014 | 0 | 13.58422 | 0 | 13.59362 |
| 9 | 0 | 1.467431 | 0 | 13.59362 | 0 |

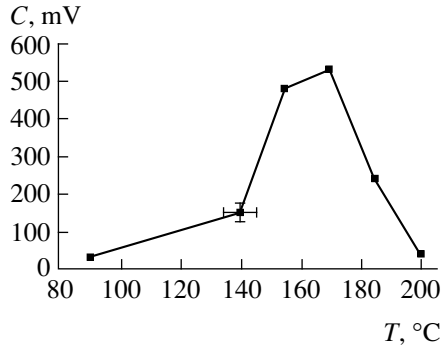


**Fig. 2.** A plot of the third harmonic signal intensity versus the temperature of naphthalene vapors in the cell. Each point presents the result of averaging over 15 measurements.

intensity of pumping radiation of the YAG:Nd laser, where the Kerr effect is insufficient for changing the sign of dispersion.

A different pattern and conditions for the third harmonic generation are observed in the second possible case. No region of negative dispersion is required for realization of the process $\omega + \omega + \omega + \omega - \omega \Rightarrow 3\omega$, since a difference frequency can be generated in the synchronous mode in a medium with arbitrary sign of dispersion [14, 15]. Thus, the nonlinear optical process of the fifth order seems to be most probable in our system. In this case, the nonlinear susceptibility ($\chi^{(5)}$) will be determined (like $\chi^{(3)}$ in the case considered above) by the presence of transition lines with high oscillator strengths near the four- photon resonance (37564 $cm^{-1}$). For the naphthalene vapors, the frequency shift is sufficiently large. A similar process of the difference frequency generation in naphthalene vapors in the region of third harmonic of a YAG:Nd laser was studied previously for a four-photon process of the type ($2\omega + 2\omega - \omega \Rightarrow 3\omega$) [8].

The absolute value of the conversion efficiency was determined taking into account transmission of the optical elements, photocathode efficiency and gain of the phototube, and the spectrometer transmission function. Absolute calibration of the registration system was performed with aid of two KDP (potassium dihydrophosphate) crystals mounted in front of the cell, in which the IR radiation was converted into the third harmonic and then measured using an energy meter and the phototube. The maximum conversion efficiency measured for the third harmonic generation process in naphthalene vapors was $10^{-8}$.

To summarize, we have studied the process of nonlinear optical conversion of the frequency of YAG:Nd laser radiation from IR into UV range in naphthalene vapors. The optimum temperature of naphthalene vapors (170°C) was found at which the pumping radiation energy is synchronously transferred to the third harmonic emission. A mechanism of the third harmonic generation is proposed based on the difference frequency generation in a six-photon process. The efficiency of conversion to the third harmonic varied within $10^{-10}$–$10^{-8}$, depending on the pumping intensity and cell temperature. Nonlinear optical characteristics of naphthalene vapors were calculated near the line of generation using nonlinearities of the third and fifth order.

## REFERENCES

1. K. K. Innes, B. P. Stoicheff, and S. C. Wallace, Appl. Phys. Lett. **29**, 715 (1976).
2. M. N. R. Ashfold, C. D. Heryet, J. D. Prince, *et al.*, Chem. Phys. Lett. **131** (1–2), 291 (1986).
3. V. F. Lukinykh, S. A. Myslivets, A. K. Popov, *et al.*, Appl. Phys. B **38**, 143 (1985).
4. K. S. Aleksandrov, A. S. Aleksandrovskiĭ, S. V. Karpov, *et al.*, Dokl. Akad. Nauk SSSR **296**, 85 (1987) [Sov. Phys. Dokl. **32**, 734 (1987)].
5. J. S. Meth, H. Vanherzeele, and Y. Wang, Chem. Phys. Lett. **197** (1–2), 26 (1992).
6. D. Neher, G. I. Stegeman, F. A. Tinker, *et al.*, Opt. Lett. **17**, 1491 (1992).
7. R. J. Knize and J. P. Partanen, Phys. Rev. Lett. **68**, 2704 (1992).
8. A. S. Aleksandrovsky, S. V. Karpov, S. A. Myslivets, *et al.*, J. Phys. B **26**, 2965 (1993).
9. K. Ruegenberg and C. W. Scherr, J. Chem. Phys. **21**, 1565 (1953).
10. J. Duckwing, in *Nonlinear Spectroscopy*, Ed. by N. Bloembergen (North-Holland, Amsterdam, 1977; Mir, Moscow, 1979).
11. R. B. Miles and S. E. Harris, IEEE J. Quantum Electron. *QE-9*, 470 (1973).
12. R. A. Ganeev, I. A. Kulagin, I. A. Begishev, *et al.*, Nonlinear Opt. **16**, 109 (1996).
13. T. Kitagava, J. Mol. Spectrosc. **26**, 1 (1968).
14. A. D. Dubovik, Vestn. Mosk. Univ., Ser. 3: Fiz., Astron. **18**, 82 (1977).
15. J. Reintjes, *Nonlinear Optical Parametric Processes in Liquids and Gases* (Academic Press, New York, 1984; Mir, Moscow, 1987).

*Translated by P. Pozdeev*

*Technical Physics Letters, Vol. 26, No. 5, 2000, pp. 363–365. Translated from Pis'ma v Zhurnal Tekhnicheskoĭ Fiziki, Vol. 26, No. 9, 2000, pp. 14–19.*


# Electroacoustic Wave Translation with Moving Stripe Domain in a Ferroelectric Crystal

**O. Yu. El'meshkin and N. S. Shevyakhov**

*Ul'yanovsk Department, Institute of Radio Engineering and Electronics, Russian Academy of Sciences, Ul'yanovsk, Russia*

Received August 19, 1999

**Abstract**—The possibility of translational transfer of the electroacoustic boundary waves with stripe domains moving in a tetragonal ferroelectric crystal is considered. It is shown that the stripe domain motion accounts for noncollinearity of the electroacoustic wave vector and the guiding boundaries. Conditions are determined for a pronounced boundary localization of the symmetric mode of the electroacoustic wave, which provides for the possibility of translational transfer. © *2000 MAIK "Nauka/Interperiodica".*

Devices with single stripe domain (SD) are widely employed in control systems featuring acoustodomain interactions [1]. The motion of SDs in these devices takes place only during readjustment and, in principle, is not employed in the working regime. This SD motion, appearing essentially as a side effect, by no means demonstrates all possibilities of data processing in devices implementing acoustodomain interactions. Below, we will theoretically justify the possible direct use of SD motion for the translational transfer of electroacoustic boundary waves capable of effective channeling under usual static conditions [2, 3].

In this context, we have to first verify the fact that electroacoustic waves may exist in the moving SD and check for the possibility of their sufficiently well pronounced boundary localization. This is important in order to exclude the effect of external boundaries and establish the conditions of translational transfer in real crystals of finite dimensions.

Taking into account a very simple character of the theoretical model employed in [2, 3], we will also proceed from the same assumptions. In addition, we will assume that SD moves uniformly at a subsonic velocity $\mathbf{V}_D \| y \| [010]$, $V_D < c_t$ ($c_t$ is the transverse shear wave velocity) in a ferroelectric crystal of the $BaTiO_3$ type occurring in the state far from the region of phase transitions. This assumption allows us, first, to neglect various possible processes of structural rearrangement involving SD boundaries. These boundaries are considered as geometrically thin 180° domain walls with the current coordinates $y_1 = V_D t$, $y_2 = V_D t + d$, where $t$ is the current time and $d$ is the SD wall thickness. Second, we may consider the motion of SD as a predetermined process.

The directions of spontaneous polarization and shear displacements in the electroacoustic waves propagating in the $x0y$ plane coincide with the $z$ axis (parallel to the [001] crystal axis) in the laboratory frame $x0yz$. The ferroelectric crystal is considered as a piezoelectric crystal of the 4 mm group, which exhibits twinning in the planes of SD boundaries [2, 3]. The values of the piezoelectric modulus $e_{15}$ are taken equal to $e$ for $y_1 < y < y_2$ and $-e$ for $y < y_1$ and $y > y_2$, where $e$ is the piezoelectric modulus of a monodomain sample.

Taking into account obvious limitations $V_D/c \ll 1$, $c_t/c \ll 1$ (where $c$ is the velocity of light), we pass to the SD rest coordinate system $\tilde{x}0\tilde{y}\tilde{z}$ (most adequately reflecting the character of the problem under consideration) in a nonrelativistic quasistatic approximation based on the Galilean transformation $\tilde{x} = x$, $\tilde{y} = y - V_D t$, $\tilde{z} = z$, $\tilde{t} = t$. This is equivalent to the change of differential operators by the scheme $\partial/\partial x \longrightarrow \partial/\partial\tilde{x}$, $\partial/\partial y \longrightarrow \partial/\partial\tilde{y}$, $\partial/\partial t \longrightarrow \partial/\partial\tilde{y} - V_D\partial/\partial\tilde{y}$ in the initial equations and boundary conditions. Finally, we obtain

$$\left[\frac{1}{c_t^2}\left(\frac{\partial}{\partial\tilde{t}} - V_D\frac{\partial}{\partial\tilde{y}}\right)^2 - \tilde{\nabla}^2\right]\begin{pmatrix} u \\ u_j \end{pmatrix} = 0,$$
$$\tilde{\nabla}^2\begin{pmatrix} \Phi \\ \Phi_j \end{pmatrix} = 0. \qquad (1)$$

Here, $u$ and $u_j$ are the shear displacements in SD ($0 < \tilde{y} < d$) and outside ($j = 1$ for $\tilde{y} < 0$; $j = 2$ for $\tilde{y} > d$), $\tilde{\nabla}^2 = \partial^2/\partial\tilde{x}^2 + \partial^2/\partial\tilde{y}^2$, and $\Phi$ and $\Phi_j$ are the parts of potentials

$$\varphi = \frac{4\pi e}{\varepsilon}u + \Phi, \quad \varphi_j = -\frac{4\pi e}{\varepsilon}u_j + \Phi_j, \qquad (2)$$

representing the electrostatic fields in SD and outside induced by the piezopolarization charges occurring at the boundaries, and $\varepsilon$ is the dielectric permittivity.

Aiming at constructing the solutions to equations (1) of the type $\exp i(k_\| \tilde{x} - \Omega\tilde{t})$ and taking into account the

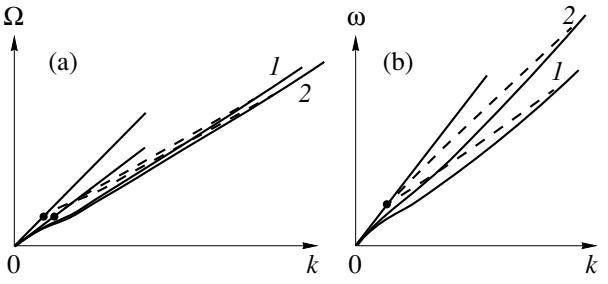


**Fig. 1.** Comparative spectral pattern of modes for the static (curves *1*) and moving (curves *2*) stripe domain in the (a) SD rest frame and (b) laboratory frame of reference.

condition that the quantities $u$, $\Phi$ and $u_j$, and $\Phi_j$ must be limited in the domains of their determination, we may show that

$$\begin{aligned} u_j &= U_j e^{i\xi} e^{ik_\perp \tilde{y}} \exp[(-1)^{j+1} s\tilde{y}], \\ u &= e^{i\xi} e^{ik_\perp \tilde{y}} (Ve^{-s\tilde{y}} + We^{s\tilde{y}}), \\ \Phi_j &= F_j e^{i\xi} \exp[(-1)^{j+1} k_\parallel \tilde{y}], \\ \Phi &= e^{i\xi} (Ae^{-k_\parallel \tilde{y}} + Be^{k_\parallel \tilde{y}}). \end{aligned} \tag{3}$$

Here, $\xi = k_\parallel \tilde{x} - \Omega \tilde{t}$ is the phase of the electroacoustic wave oscillations along SD, $\Omega$ is the frequency of oscillations in the SD rest frame, $k_\parallel$ and $k_\perp$ are the longitudinal and transverse components of the electroacoustic wave vector $\mathbf{k} = \mathbf{k}_\parallel + \mathbf{k}_\perp$ relative to the SD boundaries. The components obey the relationships

$$k_\perp = \frac{\Omega}{c_t} \frac{\beta}{1-\beta^2}, \quad s = \frac{1}{1-\beta^2} \sqrt{k_\parallel^2 (1-\beta^2) - \frac{\Omega^2}{c_t^2}}, \tag{4}$$

where $\beta = V_D/c_t$.

In addition to (4), a relationship (characteristic of the electroacoustic waves) between the amplitude decay coefficients and the longitudinal wave vector component can be obtained using the boundary conditions for $\tilde{y} = 0, d$. These conditions reflect continuity of the shear displacements, stresses, potentials, and normal components of the electric induction [2, 3]. Note that these quantities contain no derivatives with respect to time and, hence, do not change their forms upon going to the SD rest frame of reference. The condition of zero determinant of a system of equations obtained upon substituting expressions (2) and (3) leads to the following equation:

$$\begin{aligned} &\mathcal{K}^4 \kappa^2 (1 - e^{-2\kappa})(1 - e^{-2\sigma}) \\ &- 2\mathcal{K}^2 \kappa\sigma (1 - e^{-\sigma} e^{-\kappa} \cos k_\perp d) + \sigma^2 = 0, \end{aligned} \tag{5}$$

where $\kappa = k_\parallel d$, $\sigma = sd$, $\mathcal{K}^2 = 4\pi e^2 (\varepsilon\lambda^*)^{-1}$ is the square electromechanical coupling coefficient, $\lambda^* = \lambda + 4\pi e^2/\varepsilon$, and $\lambda$ is the shear modulus.

Similarly to the static case of $\beta = 0$ ($k_\perp = 0$) [2], equation (5) shows the existence of two spectral branches (modes) of the electroacoustic wave retained by the SD. By analogy with [2], these branches are called symmetric and antisymmetric–according to the predominant character of distribution of the shear displacements (3) with the transverse coordinate $\tilde{y}$ along the wavefront relative to the SD median plane $\tilde{y} = d/2$.

Figure 1 shows the spectral representation of the electroacoustic wave in the SD rest frame (Fig. 1a) and the laboratory frame (Fig. 1b) for the symmetric (solid lies) ad antisymmetric (dashed) modes with $\beta = 0$ (curves *1*) and $\beta \neq 0$ (curves *2*). The passage from the laboratory frame to the SD rest frame implies a parametric conversion of the frequency $\omega$ by the relationship $\omega = \Omega/(1 - \beta^2)$ established by applying the Galilean transformation to expressions (3). In Fig. 1, the angular deviation of the low-frequency asymptote of the symmetric mode from the common high-frequency asymptote depicted by straight segments continuing the corresponding spectral branches (this asymptote represents a spectrum of the Marfeld–Turnois mode of the electroacoustic wave on an isolated domain wall [4]) is intentionally exaggerated. A difference in the spectra of modes depicted in Figs. 1a and 1b can be explained by a relative character of the spectral description in various frames of reference.

According to equations (3) and (4), the motion of SD will be manifested in the electroacoustic wave structure by noncollinearity of the wave vector $\mathbf{k}$ and the guiding surfaces $\tilde{y} = 0, d$. For the waves on stationary (fixed) boundaries, this property (typical of outgoing or pseudosurface acoustic waves [5] and radiative polariton states [6]) is evidence of the energy losses as a result of emission into the underlying space volume or into the environment. For this reason, the surface waves of this type are always decaying.

In the case under consideration, the electroacoustic wave moving with SD can be formally associated with a decay wave of "leak" on one side of the SD ($\tilde{y} > d$). On the other side of SD ($\tilde{y} < 0$), the wave has a structure of the oncoming wave not typical of the known surface waves. Thus, the electroacoustic wave exhibits a common energy flux with a component parallel to the direction of SD motion. This component determines the level of energy consumption from an external source for the translational motion of the electroacoustic wave coupled with the SD by piezopolarization charges.

The spectra of modes presented in Fig 1 demonstrate the ability of the electroacoustic wave to travel in a steady-state manner along the carrying SD without decay or growth: $k > 0$, $\omega > 0$, $\Omega > 0$. Figure 2 shows the frequency dependence of the localization index $\Gamma = s/k$ calculated for the $BaTiO_3$ crystal ($\mathcal{K}^2 = 0.38$), which confirms the boundary character of the wave. The only exception is the point of the antisymmetric mode generation (black circle in Fig. 1), which is observed on the

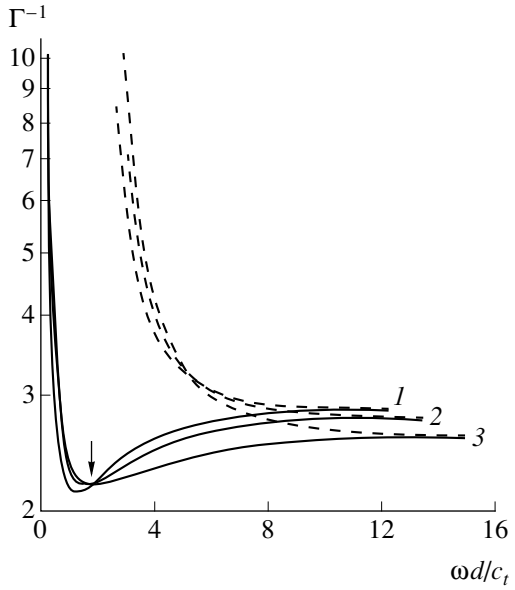


**Fig. 2.** Frequency dependence of the delocalization parameter $\Gamma^{-1} = k/s$ for the electroacoustic wave on a stripe domain in $BaTiO_3$ (laboratory frame) for $\beta = 0.6$ (*1*), 0.45 (*2*), 0 (*3*).

low-frequency asymptote $\Omega = kc_t(1 - \beta^2)$ (Fig. 1a) or at $\omega = kc_t$ (Fig. 1b), representing the law of dispersion of the bulk shear waves in a monodomain crystal. At this point, the antisymmetric mode degenerates into a simplest form of the discrete spatial spectrum of flat homogeneous shear waves carried by the SD, the so-called attached (better to say "entangled") waves predicted in [7].

Based on Fig. 2, we may conclude that the boundary localization of oscillations is best manifested in the symmetric mode (solid curves). As the value of $\beta$ increases, this mode decays rather slightly and (for not very thin SD, $kd > 1$) exceeds the level of boundary localization for the Marfeld–Turnois mode [4] determined by the high-frequency asymptotic limit. Note an interesting possibility of $\beta$-independent and almost maximum boundary localization of the symmetric mode in the region of frequency dependence of $\Gamma^{-1}(\omega)$ indicated by the arrow. In this region, the localization length of the electroacoustic wave slightly exceeds two wavelengths, which implies that the electroacoustic wave would be virtually absent at a somewhat distance (e.g., three wavelengths) from SD. For a transverse crystal size of the order of a longitudinal SD size, the process of translational transfer of the electroacoustic wave under these conditions may quite well establish.

The work was supported by the Federal Program "Integration" (project no. A 0065).

## REFERENCES

1. A. N. Alekseev, Izv. Akad. Nauk, Ser. Fiz. **57**, 92 (1993).
2. V. N. Lyubimov and D. G. Sannikov, Kristallografiya **24**, 5 (1979) [Sov. Phys. Crystallogr. **24**, 1 (1979)].
3. Li Xingjiao, J. Appl. Phys. **61**, 2327 (1987).
4. C. Maerfeld and P. Tournois, Appl. Phys. Lett. **19**, 117 (1971).
5. S. V. Biryukov, Yu. V. Gulyaev, V. V. Krylov, and V. P. Plesskiĭ, *Surface Acoustic Waves in Inhomogeneous Media* (Nauka, Moscow, 1991).
6. *Surface Polaritons*, Ed. by V. M. Agranovich and D. L. Mills (North-Holland, Amsterdam, 1982; Mir, Moscow, 1985).
7. L. M. Lyamshev and N. S. Shevyakhov, Pis'ma Zh. Tekh. Fiz. **17**, 13 (1991) [Sov. Tech. Phys. Lett. **17**, 611 (1991)].

*Translated by P. Pozdeev*

*Technical Physics Letters, Vol. 26, No. 5, 2000, pp. 366–368. Translated from Pis'ma v Zhurnal Tekhnicheskoĭ Fiziki, Vol. 26, No. 9, 2000, pp. 20–24.*


# Biological Activity of the Human Skin Studied by Method of Speckle Counting

**A. P. Vladimirov, A. L. Lisin, V. I. Mikushin, M. M. Kokhan, I. A. Kuklin, and E. V. Kononenko**

*Institute of Engineering Science, Ural Division, Russian Academy of Sciences, Ekaterinburg, Russia*
*Institute of Dermatovenerology and Immunopathology, Ekaterinburg, Russia*
*Ural State Technical University, Ekaterinburg, 620083 Russia*
Received September 22, 1999

**Abstract**—Experimental data on the real-time dynamics of speckles related to biological processes in the human skin are presented. © *2000 MAIK "Nauka/Interperiodica".*

**Introduction.** The dynamics of biospeckles related to the biological activity of cells were reported for various objects, including fruits [1] and microorganisms [2]. Utts [3] used the dynamics of speckles induced by a laser beam scanning over the skin to study the skin roughness. Bonch-Bruevich *et al.* [4] employed a picosecond laser for observation of the pattern of speckles in the image of a human arm skin area. It was found that the pattern of speckles exhibited partial variation with time.

Below, we report on the first results of our investigation into the free-field dynamics of biospeckles formed by laser radiation scattered from a human skin area. The quantitative analysis was performed using a speckle counting technique developed in [5–7]. A method is proposed for separation of the contributions of two processes affecting the speckle dynamics, namely, biological processes in the skin cells and uncontrolled arm movements. The proposed method was used for a comparative investigation of intact and damaged skin areas.

**Experimental methods and results.** The experimental techniques and methods were described in detail elsewhere [8]. Figure 1 shows a schematic diagram of the setup used in this work. Experiments were performed with the aid of an LG-38M He–Ne laser with a wavelength of $\lambda = 0.6328$ μm and a power of 50 mW. Uncontrolled movements of the arm of a patient were restricted by using a special fixing device. The beam of laser *1* was divided by a semitransparent mirror *3* into two beams, which were focused with the aid of mirrors *2* and lens *4* onto 0.5-mm-diam holes in the fixing device *5*. The skin in one hole was covered with a sheet of nontransparent paper fixed with a rubber cement. The skin areas in the fixing device were tightly pressed against the holes. The light beams scattered from two areas stroke the photodiode matrix detector (PMD) *8*. We have employed a PMD of the LF 1024-25/1 type accommodating 1024 photosensitive cells with dimensions $24 \times 25$ μm separated by 1-μm-wide gaps. The conditions of object illumination and scattered signal detection were selected so as to provide that the PMD would detect the laser radiation reflected within a skin layer of certain thickness.

The signal from PMD was fed to a computer via a special data interface similar to that described in [9]. The PMD cell interrogation frequency could be varied from 4 to 10 Hz. The data were acquisited and processed using a special program package [7], which provided real-time monitoring of the signal distribution over PMD cells and allowed noise filtration and determination of the number $N$ of points at which the signal intensity intersected floating threshold levels equal to the average signal intensities for a given group of cells. The $N_1$ and $N_2$ values corresponding to a skin area and a control paper surface were determined by averaging

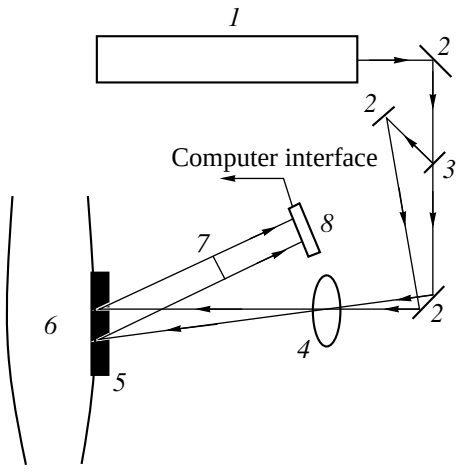


**Fig. 1.** Schematic diagram of the optical system: (*1*) laser; (*2*) mirrors; (*3*) semitransparent mirror; (*4*) lens; (*5*) arm holder with two holes; (*6*) object (arm); (*7*) screen; (*8*) PDM.

1063-7850/00/2605-0366$20.00 © 2000 MAIK "Nauka/Interperiodica"

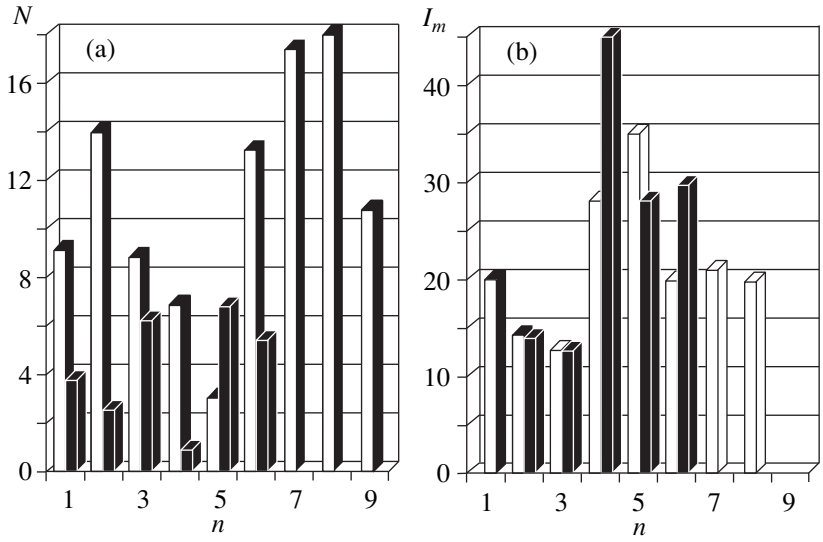


**Fig. 2.** Histograms of (a) the number of speckles $N$ and (b) their average intensity $I_m$ for various patients (indicated by number $n$).

over 100 cells with a unit step. The observations were performed on the forearm skin areas of three healthy people (control group) and six patients with various forms of allergic dermatitis and psoriasis. Data on the patients were reported elsewhere [8].

Observations of the variation of $N_1$ and $N_2$ values with time showed that both quantities represent almost linear functions with the average slope of $N_1 = N_1(t)$ being usually markedly greater compared to that of $N_2 = N_2(t)$. It was suggested that the process of random phase variation of the scattered radiation, related to biological processes occurring in the skin and the process of phase variation caused by the uncontrolled arm movements can be considered as steady-state statistically independent Gaussian stochastic processes. We have employed the fact that the number of threshold intersections and the correlation interval of the scattered radiation intensity for these processes are inversely proportional to one another [5, 6, 10]. It was also assumed that the proportionality factors are the same for various processes, provided that the thresholds are equal to the average signal values. Then, in the case of small phase variations, the value of $N$ representing a contribution due to the biological processes can be determined by the following formula [8]:

$$N = (N_1^2 - N_2^2)^{1/2},$$

where the vales of $N$, $N_1$, and $N_2$ refer to the same time instant $t$.

Figure 2a shows a histogram of $N$ values calculated by the above formula using the data for various patients (indicated by number $n$). Light columns refer to intact (undamaged) skin areas, and dark columns, to the areas bearing evident signs of damage; the $N$ values were determined for $t = 20$ s after the beginning of laser irradiation. Figure 2b shows the values of signals proportional to the radiation intensity $I_m$ within the same skin areas. The $I_m$ values were determined in the same cells upon smoothening of the signal variation over cells (also measured 20 s after the onset of irradiation).

**Discussion of results.** In this work, the $N$ values were determined assuming that the two different diffuse reflectors (skin area and the surface of a nontransparent paper glued onto skin) produce the same changes in the pattern of speckles related to the arm movements. Under this assumption, Fig. 2a shows that biological processes in the skin of various patients account for 0.05–0.9 speckles per second. Skin is the object with complicated optical properties and, hence, it would be difficult to indicate factors responsible for these variations in the scattered radiation intensity. These factors may include, in particular, the flows of blood and lymph, Brownian motions of various species in the intercellular fluid, intercellular framework deformations, and many others. As is seen from Figs. 2a and 2b, the average intensity of radiation reflected from the human skin is somewhat higher for the damaged skin areas, while the number of speckles is generally higher for intact skin areas. This is apparently indicative of the fact that undamaged areas exhibit somewhat higher transmission of the He–Ne laser radiation. However, the lack of reliable experimental data hinders justified explanation of a difference between the number of speckles observed on the intact and damaged skin areas.

Apparently, a different response of living cells in the intact and damaged areas to the incident laser radiation may also contribute to the observed dynamics of speckles.

We believe that the results of our investigation gave grounds for certain optimism. If the observed features will be confirmed for a sufficiently large number of

patients, the proposed method of counting speckles will be useful for the investigation of processes in the human skin, in particular, for the study of skin response to various external factors. In a more distant perspective, this technique may be used for the differential diagnostics of dermatitis.

## REFERENCES

1. A. Onlamara, G. Tribillon, and J. Duvemoy, J. Mod. Opt. **36**, 165 (1989).
2. B. Zheng, C. M. Pless, and Ch. S. Ih, Appl. Opt. **33**, 231 (1994).
3. S. R. Utts, Author's Abstract of Doctorate's Dissertation in Medicine (Moscow, 1998).
4. A. M. Bonch-Bruevich, S. D. Nikolaev, I. O. Starobogatov, *et al*., Pis'ma Zh. Tekh. Fiz. **20**, 42 (1994) [Tech. Phys. Lett. **20**, 538 (1994)].
5. N. Takai, T. Iwai, I. Ushizoka, and T. Asakura, J. Opt. (Paris) **11**, 93 (1980).
6. B. Ruth, D. Haina, and W. Waidelich, Opt. Acta **30**, 841 (1983).
7. A. P. Vladimirov, V. I. Mikushin, and O. V. Golub, Proc. SPIE **2300**, 243 (1995).
8. Research Report No. RK 01990007223 (Ural Div., Rus. Acad. Sci., Yekaterinburg, 1999).
9. A. P. Vladimirov and V. I. Mikushin, Prib. Tekh. Éksp., No. 3, 58 (1998).
10. V. I. Tikhonov, *Random Process Fluctuations* (Nauka, Moscow, 1970).

*Translated by P. Pozdeev*

*Technical Physics Letters, Vol. 26, No. 5, 2000, pp. 369–371. Translated from Pis'ma v Zhurnal Tekhnicheskoĭ Fiziki, Vol. 26, No. 9, 2000, pp. 25–30.*


# Multiplexed Counter-Beam Speckle Holograms in Bichromated Gelatin

**Yu. N. Denisyuk, N. M. Ganzherli, and D. F. Chernykh**

*Ioffe Physicotechnical Institute, Russian Academy of Sciences, St. Petersburg, 199026 Russia*

Received December 16, 1999

**Abstract**—Experimental data on the recording and multiplexing of shifted counter-beam holograms with a speckle reference beam are presented. The experiment confirmed the possibility of multiplexing shear speckle holograms by shifting the photosensitive material by a distance equal to the reference beam speckle size. As the number of multiplexed holograms increases, their lifetime in a layer of bichromated gelatin significantly decreases. © *2000 MAIK "Nauka/Interperiodica".*

A possible method of data compression consists in their recording by means of 3D holograms, which can be realized by multiply rewriting holograms in the same volume of a photosensitive material [1]. Previously [2, 3], we reported on the results of experiments with a new thick-layer photosensitive material for holography based on a glycerol-containing bichromated gelatin. This material has an advantage of self-development, whereby a restored image can be observed immediately in the course of the hologram recording. The thick-layer bichromated gelatin is sensitive in the blue spectral region and is characterized by a long time of storage for a pair of flat-wave holograms. However, the structure of a real multiplexed hologram significantly differs from that of a single three-dimensional lattice. In order to study behavior of the new material under real data storage conditions, we have performed experiments on the counter-beam hologram multiplexing using a speckle reference beam.

Recently [4, 5], we reported on the results of experiments in which 3D shifted speckle holograms were multiplexed using a special axial system. An advantage of this scheme for recording 3D holograms consists, besides simplicity, in the possibility of focusing the object and reference waves exactly onto a small area of the photographic material. In addition, this scheme is less sensitive with respect to system vibrations and the degree of coherency of the radiation employed (in comparison with an off-axis recording schemes.

The multiplexed recording is based on the property of shift selectivity of holograms recorded with the aid of a speckle reference wave [6–8]. According to this method, the multiplexing is performed using the following procedure. A radiation wave scattered from object 1 is recorded onto a photosensitive material with the aid of a speckle reference wave formed by the laser beam passing through a diffuser. Then, the photosensitive materials shifted by a distance equal to the transverse size of a speckle formed by the reference wave and the hologram of object 2 is recorded. The third and subsequent objects are recorded similarly, using the same reference wave. Moreover, the same reference wave is used in the hologram reconstruction stage as well. Readout of the required page is performed upon shifting the hologram to a preset position.

According to the theory of shifted speckle holograms, the step of shifts during the recording and reconstruction of the multiplexed hologram is determined by an average speckle size in the reference wave field on the hologram surface. The average transverse size $\delta$ of a speckle, formed by the speckle wave passing through a hole of diameter $d$ situated at a distance $F$ from the surface on which the speckle pattern is observed, is given by the well-known relationship

$$\delta = 1.22\lambda F/d.$$

The intensity of the reconstructed wave reaches maximum when the speckle pattern of the restoring wave exactly coincides with the pattern recorded in the hologram. The intensity drops with decreasing overlap of the two patterns and is zero if the patterns do not overlap.

Let us consider experimental results on the multiplexing of shifted counter-beam speckle holograms in a volume photosensitive medium. The optical scheme of the hologram multiplexing is depicted in the figure. This process is based on the splitting and converging of colored beams by a scheme close to the Mach–Zender interferometer. According to this, a laser beam is divided into two by the beam-splitting cube BS. The transmitted light beam is expanded by a collimator comprising microobjective lens ML and lens $L_1$, after which the beam is reflected by mirror M to the object transparency O positioned in the front focal plane of lens $L_2$. The recording medium H is placed in the rear focal plane of this lens, performing the Fourier transform. The second beam is passed through diffuser D and a system of lenses $L_3$ and $L_4$ to form the reference

1063-7850/00/2605-0369$20.00 

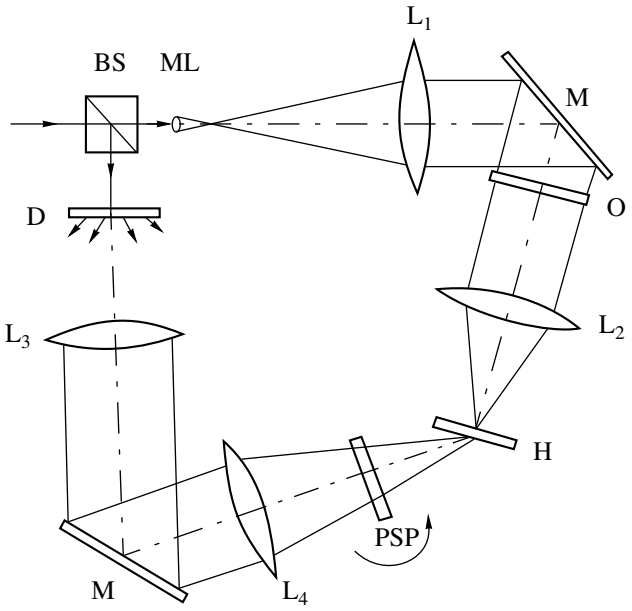


Schematic diagram of the system of hologram recording in the counter-beam mode with reference speckle beam: (BS) beam slitting cube; (ML) microobjective lens; (D) diffuser; ($L_1$–$L_4$) lenses; (M) mirrors; (O) object transparency; (PSP) plane-parallel glass plate; (H) recording holographic medium.

beam. Diffuser D is positioned in the front focal plane of lenses $L_3$ and $L_4$, with the recording medium H occurring in the rear focal plane of this lens system. Adjustment of the system consists in providing that the object and reference beams (counter-beams), entering the recording medium from opposite sides, would intersect and interfere in this medium. It is also desired that the objective beam would be normal to the surface of recording medium H.

Multiplexed recording can be performed by the following methods: (i) small shifts of the speckle reference beam in the recording plane achieved by rotating plane-parallel glass plate PSP positioned between lens system and recording medium; (ii) shift of the recording medium in two mutually perpendicular directions in the recording plane or rotation of the medium in this plane; and (iii) translation or rotation of diffuser. In our experiments, the holograms were multiplexed by very small shifts of the speckle pattern along the photosensitive material surface, which was achieved by rotating plane-parallel plate PSP through small angles.

First, we have determined the shift of the speckle pattern of the reconstructing wave relative to the hologram, for which the reconstructed image disappears. For this purpose, a single hologram was recorded in the photosensitive layer. Since the optical scheme employed allowed us to concentrate the laser beam onto a small area of the photosensitive material, the exposure time varied from 3 s to 1.5 min at a laser power of 16 mW. During the image reconstruction, the object beam was stopped by a shutter. The quality of the restored image was good, although the noise level was somewhat higher as compared to that during a real object observation. The experiment showed that the restored image intensity became nonzero when the speckle pattern was shifted by 6 μm.

We have studied multiplexed recording of the speckle holograms of an object transparency, representing a matrix of randomly arranged emitting points modeling a page of bit data. Taking into account that the "zero-to-zero" step is 6 μm, we have selected a step of 10 μm, which corresponded in our scheme to the angle of 1-cm-thick PSP plate rotation by 10 seconds of arc. Shifting the speckle wave after every exposure by 10 μm, we recorded 17 shifted speckle holograms in the same volume of thick-layer bichromated gelatin. The exposure time was gradually increased from 3 s for the first hologram to 90 s for the last one.

A comparison of this variant with the recording of shifted speckle holograms by the axial scheme showed a better signal-to-noise ratio and somewhat greater number of recorded holograms in the case described above. However, reliability of the multiply repeated readout can be increased only by decreasing thickness of the PSP plate so as to provide that the rotation angle would be 30 minutes of arc. This increased the accuracy of matching of the positions of reference beam speckle patterns during record and readout

Resolution in the images reconstructed with this multiplexed hologram was sufficiently high, but the noise of restored image markedly increased with the number of multiplexed holograms. However, it was a rather unexpected behavior of the photosensitive material, rather than the increasing noise of restored images, that limited the number of multiplexed holograms. The experiment showed that the lifetime of multiplexed holograms, even provided their limited number, decreased to a few hours. This behavior of the multiplexed speckle holograms is rather unexpected, since the lifetime of a single speckle hologram exceeded one week.

Thus, the results of our experiments confirmed the possibility of recording and multiplexing holograms in the counter-beam mode with speckle reference beam. The multiplexed holograms recorded in a thick-layer bichromated gelatin have a limited lifetime. Use of the self-developing thick-layer bichromated gelatin allowed the features of this multiplexing method to be experimentally studied in a real time. It was also possible to change the exposure time, the PSP plate rotation angle at which the restored image of preceding hologram vanished, and other parameters immediately during experiment.

This work was supported by the Russian Foundation for Basic Research, project no. 99-02-18481.

## REFERENCES

1. P. J. Van Heerden, Appl. Opt. **2**, 393 (1963).
2. Yu. N. Denisyuk, N. M. Ganzherli, I. A. Maurer, and S. A. Pisarevskaya, Pis'ma Zh. Tekh. Fiz. **23**, 62 (1997) [Tech. Phys. Lett. **23**, 279 (1997)].
3. Yu. N. Denisyuk, N. M. Ganzherli, I. A. Maurer, and S. A. Pisarevskaya, Pis'ma Zh. Tekh. Fiz. **25**, 64 (1999) [Tech. Phys. Lett. **25**, 194 (1999)].
4. Yu. N. Denisyuk, Opt. Spektrosk. **85**, 317 (1998) [Opt. Spectrosc. **85**, 293 (1998)].
5. Yu. N. Denisyuk, N. M. Ganzherli, I. A. Maurer, and S. A. Pisarevskaya, Opt. Spektrosk. **86**, 1023 (1999) [Opt. Spectrosc. **86**, 922 (1999)].
6. V. B. Markov and A. M. Darskiĭ, Opt. Spektrosk. **65**, 661 (1988) [Opt. Spectrosc. **65**, 392 (1988)].
7. V. B. Markov and A. M. Darskiĭ, Opt. Laser Technol. **21**, 198 (1989).
8. V. B. Markov, Yu. N. Denisyuk, and R. Amezquita, Opt. Mem. Neural Netw. **6**, 91 (1997).

*Translated by P. Pozdeev*

*Technical Physics Letters, Vol. 26, No. 5, 2000, pp. 372–374. Translated from Pis'ma v Zhurnal Tekhnicheskoĭ Fiziki, Vol. 26, No. 9, 2000, pp. 31–35.*


# Atomic Relocations in a Two-Layer Al/Ni System Bombarded with Ions Having Energies Close to the Sputtering Threshold

**G. V. Kornich[1], G. Betz[2], and A. I. Bazhin[3]**

[1] *Zaporozhskiĭ State Technical University, Zaporozh'e, Ukraine*
[2] *Institut für Allgemeine Physik, Technische Universität Wien, A-1040 Wien, Austria*
[3] *Donetsk State University, Universitetskaya ul. 24, Donetsk, 340055 Ukraine*

Received November 19, 1999

**Abstract**—Collision cascades developed at 300 K in a Ni single crystal and in a system comprising a monolayer of Al atoms on the Ni(100) single crystal face bombarded at normal incidence by 25- and 50-eV Ar and Xe atoms were simulated by method of molecular dynamics. It was found that the number of atoms relocated through the Al–Ni interface markedly exceeds the number of analogous relocations in the nickel single crystal.


During the ion bombardment of a multicomponent spatially inhomogeneous system, the chemical interactions determining mutual solubility of the system components may affect the broadening of boundary regions between components related to the bombardment-induced collisional processes [1–3]. Simulation of these processes by methods of molecular dynamics allows the effect of chemical interactions on the relocation of atoms in collision cascades to be described in terms of the interatomic potentials [4, 5].

In this work, we have simulated the collision cascades induced in the target by the bombardment with 25- and 50-eV Ar and Xe atoms at normal incidence onto the target surface. We have studied the room-temperature (300 K) bombardment of two targets: (i) a two-component system comprising a monolayer of Al atoms on the Ni(100) crystal surface and (ii) a Ni single crystal with the same surface orientation. The purpose of this investigation was to assess the effect of interatomic forces on the cascade relocations of atoms in the Al–Ni system and compare the average numbers of relocations at the Al–Ni interface and in the Ni single crystal.

In the molecular dynamics stimulation, we have employed an algorithm describing the interactions between atoms in terms of a many-body potential [6] matched at high energies with the ZBL potential [7]. The equations of motion of the particles were solved by the Verlet method [8].

A nickel single crystal was composed of 4032 atoms, and the Al–Ni two-layer crystal contained 3944 atoms, both systems comprising 14 atomic layers. In the uppermost atomic layer of the Al–Ni crystal, two rows of Al atoms were missing from the perimeter of the sample; these atoms were excluded in order to avoid nonphysical surface distortions caused by a difference of the lattice constants of aluminum (4.05 Å) and nickel (3.52 Å) [9, 10]. Aluminum atoms in this surface layer repeated the lattice order of the Ni(100) substrate. The ambient temperature was simulated by immersing the target into a medium with preset temperature [11]. The initial coordinates of ions falling within a given elementary region of the target surface [12] were calculated based on the law of random numbers. All simulations involved 200 cascades. Each cascade was followed in the initial crystal during 4 ps.

As seen from Tables 1 and 2, the numbers of atoms relocated from the uppermost surface layer (Al) into the substrate (Ni) and vice versa in the Al–Ni two-layer crystal bombarded by 50-eV Ar atoms were greater by the factors 2.5 and 3.2 than the numbers of analogous relocations in the Ni single crystal. The proportion of

**Table 1.** The numbers of adatoms, exchange transitions between 1st and 2nd layers, and relocations from the 1st layer into bulk in the Ni crystal

| Ni | | Adatoms | 1 ⟷ 2 | 1 ⟶ bulk | 1 ⟵ bulk |
|---|---|---|---|---|---|
| Ar | 50 eV | 0.52 | 0.31 | 0.46 | 0.34 |
| | 25 eV | 0.125 | 0.13 | 0.13 | 0.13 |
| Xe | 50 eV | 0.48 | 0.32 | 0.56 | 0.33 |
| | 25 eV | 0.255 | 0.26 | 0.26 | 0.27 |

1063-7850/00/2605-0372$20.00 

**Table 2.** The numbers of adatoms, exchange transitions between 1st and 2nd layers, and relocations from the 1st layer into bulk in the Al–Ni two-layer crystal

| Al/Ni | | Adatoms | 1 ⟷ 2 | 1 ⟶ bulk | 1 ⟵ bulk |
|---|---|---|---|---|---|
| Ar | 50 eV | 2.195 | 0.955 | 1.145 | 1.085 |
| | 25 eV | 0.95 | 0.295 | 0.295 | 0.295 |
| Xe | 50 eV | 2.91 | 1.29 | 1.51 | 1.5 |
| | 25 eV | 0.95 | 0.495 | 0.505 | 0.515 |

relocations from the first atomic layer into bulk, compensated by the chains of substitutions resulting in the reverse relocation of atoms from bulk to the uppermost surface layer (including direct exchange between the first and second layers) were 74 and 95%, respectively (the direct exchange between the first and second layers accounting for 67 and 83% with respect to the total number of transitions from the first layer into bulk). In the system bombarded by 50-eV Xe ions, the numbers of Al atoms relocated from the uppermost surface layer into the substrate (Ni) and vice versa in the Al–Ni two-layer crystal were greater by the factors 2.7 and 4.5 than in the Ni single crystal. The proportion of atoms relocated from the first atomic layer into bulk as a result of compensated transitions in the Al–Ni and Ni crystals was 98 and 60%, including 85 and 57% of direct exchange transitions between the first and second layers, respectively.

The number of relocations between first and second layers in the Ni single crystal bombarded by 25-eV Xe ions was two times that in the case of bombardment by Ar ions of the same energy, the proportion of direct exchange being 96 and 100%, respectively. In the Al–Ni two-layer system, Ar ions of this energy also induced only exchange transitions of atoms between the first and second layer, the number of which was more two times that in the Ni single crystal. Bombardment of this system by Xe ions produced, besides exchange transitions between the Al monolayer and Ni substrate (the number of which was twice that for the Ni bombarded by Xe ions or the Al–Ni system bombarded by Ar ions), about ~0.05 relocations per ion in the substrate.

For 50-eV ions of both types (Ar and Xe), atoms from 3rd to 6th layers of the Al–Ni system more frequently (by a factor of 3.7–4.0) exhibited relocations of Ni atoms toward the surface than did atoms of the same layers in the Ni single crystal. This large difference in the number of reverse transitions of atoms inside the crystals of two types is explained by a large number of non-exchange near-surface relocations in the Al–Ni system that leads eventually to relocations toward deeper layers.

During the bombardment by 50-eV Ar ions, the number of atoms emerged at the crystal surface (adatoms) in the Al–Ni two-layer system was 4.3 times that in the Ni crystal, while the bombardment by 25-eV ions increased this ratio to 7.5. For Xe ions with the energies 50 and 25 eV, the number of adatoms formed in the Al–Ni system was also greater than that in Ni by the factors 6.0 and 3.7, respectively. Note that the number of adatoms emerged at the surface from the second layer under the 50-eV bombardment never exceeded 5% of their total amount, and no adatoms came from the second atomic layer under the action of bombardment at 25 eV. The greater number of adatoms on the Al–Ni surface is explained primarily by the relatively low binding energy of the surfacer Al atoms. Indeed, the difference of potential energies between the ideal Al–Ni crystal and the same crystal with one surface atom missing is (at 0 K without allowance for the lattice relaxation) 3.9 eV, while the same difference in the Ni crystal is 5.2 eV [6, 9]. A large role of the surface binding energies is also confirmed by the fact that a model sputtering coefficient for the Al–Ni system bombarded by 50-eV Ar ions is 0.06 atom/ion, while the Ni crystal is not sputtered at all. The bombardment by Xe ions led to sputtering in one of the cases studied.

In all systems under consideration, backscattered ions carried away about 10% of the incident energy for the primary ion energy 50 eV and about 20% of the energy, for 25 eV (except for the case of Ni crystal bombarded by Ar ions, where the fractions of lost energy were about 20 and 40%, respectively). The bombarding ions did not penetrate into the target crystals below the first atomic layer, except for the case of 50-eV Xe ions, which lost on the average about 8.5 eV in the second layer. Thus, a difference in the distribution of elastic ion energy losses in Al–Ni and Ni crystals may only insignificantly (e.g., in Ni bombarded by Ar ions) affect the resulting difference in the number of relocations. On the other hand, modeling of the Al–Ni system at 0 K (details of this process fall outside the scope of this paper) showed that mutual exchange in a single air of Al and Ni atoms in the first two layers decreases the potential energy of the two-layer Al–Ni system by 0.6 eV [9]. This result qualitatively agrees with a negative value of the enthalpy of mixing in the AlNi system [2].

Therefore, the process of bombardment-stimulated exchange and mutually compensated relocations of Al and Ni atoms between the first and second atomic layers in the Al–Ni system is energetically favorable. This accounted for the total increase in the number of relo-

cations from the uppermost Al layer to substrate bulk and in the reverse direction. For the bombarding ion energy 50 eV, the exchange and compensated relocations account for a greater proportion of the total number of relocations from the uppermost layer into substrate in the Al–Ni two-layer system than in the Ni crystal, which qualitatively agrees with the results of modeling in a Ni–Au two-layer system [13].

Under the conditions studied in this work, Xe ions generate more adatoms and induce a greater number of relocations in both Ni and Al–Ni crystals than do Ar ions. This is caused to a considerable extent by a greater damage of the crystal lattice produced by Xe ions in the initial stage of the cascade process, which results in a local temporal (~0.5 ps) decrease in potential barriers for the atoms migrating in the collision cascades.

## REFERENCES

1. R. Collins, Radiat. Eff. **98**, 167 (1986).
2. A. Miotello and R. Kelly, Surf. Sci. **314**, 275 (1994).
3. Y.-T. Cheng, Mater. Sci. Rep. **5**, 45 (1990).
4. J. Chladek and G. Betz, Rad. Eff. Defects Solids **142**, 51 (1997).
5. H. Gades and H. M. Urbassek, Phys. Rev. B **51**, 14559 (1995).
6. F. Gao, D. J. Bacon, and G. J. Ackland, Philos. Mag. A **67**, 275 (1993).
7. J. P. Biersack and J. F. Ziegler, Nucl. Instrum. Methods Phys. Res. B **141**, 93 (1982).
8. J. M. Haile, *Molecular Dynamics Simulation—Elementary Methods* (Wiley, New York, 1992).
9. G. V. Kornich and G. Betz, Nucl. Instrum. Methods Phys. Res. B **143**, 455 (1998).
10. G. V. Kornich, G. Betz, and A. I. Bazhin, Nucl. Instrum. Methods Phys. Res. B **153**, 383 (1999).
11. H. J. Berendsen, J. P. M. Postma, W. F. V. Gunsteren, *et al.*, J. Chem. Phys. **81**, 3684 (1984).
12. G. Betz, M. J. Pellin, J. W. Burnett, and D. M. Gruen, Nucl. Instrum. Methods Phys. Res. B **58**, 429 (1991).
13. J. A. Sprague and C. M. Gilmore, Thin Solid Films **272**, 244 (1996).

*Translated by P. Pozdeev*

*Technical Physics Letters, Vol. 26, No. 5, 2000, pp. 375–376. Translated from Pis'ma v Zhurnal Tekhnicheskoĭ Fiziki, Vol. 26, No. 9, 2000, pp. 36–40.*


# Effect of the Physicochemical Properties of the Point Material on the Surface Modification by Voltage Pulses in a Scanning Tunneling Microscope

**G. G. Vladimirov, A. V. Drozdov, and A. N. Rezanov**

*Institute of Physics, St. Petersburg State University, St. Petersburg, 199164 Russia*

Received November 11, 1999

**Abstract**—The surface morphology of gold samples in a scanning tunneling microscope was modified using points of various materials. The results indicate that a threshold level of the modifying voltage pulses depends on the physicochemical properties of the point material. This relationship can be explained within the framework of a modification mechanism involving the point–surface contact formation due to the thermal expansion of the point. *© 2000 MAIK "Nauka/Interperiodica".*

The phenomenon of surface modification on the nanometer or atomic scale in a scanning tunneling microscope opens new ways in nanolithography [1]. The most attractive possibilities, from the standpoint of reliability simplicity of realization, are offered by the surface modification under the action of electric field (voltage pulses applied to the point–surface system). Several mechanisms were suggested previously in order to explain processes involved in the surface modification, including heating of the sample surface [2], field evaporation [3], field-induced diffusion [4], stimulated chemical reactions [5], etc. However, not one of these models could adequately explain the course of the surface modification.

In our opinion, the most realistic and adequate is the mechanism based on the mechanical contact formation between point and sample surface as a result of thermal expansion of the point [6–8]. This mechanism implies that voltage pulses applied to the system lead to heating of the point by high-density current, which results in thermal expansion of the point and the formation of electric contact between point and sample.

It was demonstrated [6] that the initial stage of the pulse action (with the voltage polarity corresponding to electron emission from the point) is characterized by a change in the tunneling distance $\Delta Z$, which can be described by the relationship

$$\Delta Z = K\frac{I\varepsilon_N t}{\pi e}, \quad \text{where} \quad K = \frac{\alpha}{\rho c}, \qquad (1)$$

where $I$ is the current density; $\varepsilon_N$ is the energy liberated on the emitter due to the Nottingham effect; $t$ is the time; $e$ is the electron charge; and $c$, $\rho$, $\alpha$ are the specific heat, density, and linear thermal expansion coefficient of the point material, respectively. This relationship implies that elongation of the point depends on a combination of the physicochemical constants of the point material. In connection with this, the purpose of our experiments was to study the features of surface modification by voltage pulses applied using points made of various materials.

The experiments were conducted at room temperature in air using a scanning tunneling microscope of usual design [6] operated in a dc current mode. The stabilization current was 1 nA for a bias voltage between point and sample having a magnitude of 0.1 V and the polarity corresponding to electron emission from the point. The surface of a ~1 μm-thick gold film used as the sample represented a vacuum-deposited replica of the KBr crystal cleavage surface prepared in a vacuum of $10^{-5}$ Torr.

The points were prepared from wires of various metals by electrochemical etching at an alternating voltage of 6 V in a corresponding etchant: tungsten (initial diameter 0.14 mm, 4% NaOH solution), nichrome (0.14 mm, 20% $H_3PO_4$), constantan (0.20 mm, 20% $H_3PO_4$), copper (0.16 mm, concentrated $H_3PO_4$), and silver (0.35 mm, 25% $H_2SO_4$).

The process of Au surface modification consisted in applying single electric pulses of rectangular shape and a duration of 10 μs via a point scanning over the sample surface. The pulse amplitude could be varied within 0–6 V. All experiments were performed in the same setup, which excluded differential effects related to variable parameters of the electronic circuit [9].

Application of the single rectangular voltage pulses to the gold surface resulted in the formation of nanostructures in the form of hills with a typical radius of 20–30 nm and a height of 1–3 nm.

The process of nanostructural surface modification has a stochastic character, with the probability of hill formation $P$ (which is a function of the applied pulsed voltage amplitude $U$) determined as a ratio of the number of pulses resulting in the surface modification to the

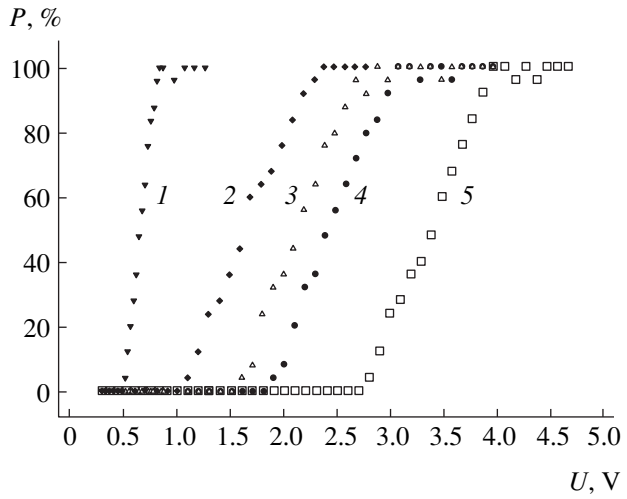


**Fig. 1.** Plots of the probability $P$ of nanostructure formation on the gold surface versus the applied pulsed voltage amplitude $U$ for the points made of various materials: (*1*) silver; (*2*) copper; (*3*) constantan; (*4*) nichrome; (*5*) tungsten.

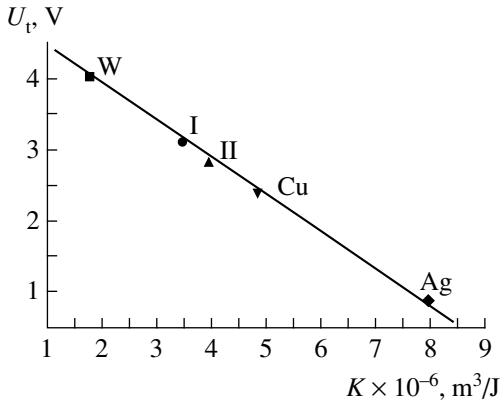


**Fig. 2.** Plot of the threshold pulse amplitude for the nanostructure formation on the gold surface versus the coefficient $K = \frac{\alpha}{\rho c}$ for the points made of various metals and alloys (I, nichrome; II, constantan).

total number of applied pulses. For each of the point materials studied, this probability exhibited a threshold character.

Figure 1 shows the plots of the probability of hill formation $P$ versus the applied pulsed voltage amplitude $U$ for the points made of various materials. Each experimental point in the $P(U)$ curves represents the result of averaging over 25–30 independent measurements. As seen, the probability $P$ sharply increases when the pulse amplitude exceeds certain level and rapidly reaches saturation as the voltage grows further (within a few tenths of volt). The pulse amplitude corresponding to attaining the probability saturation was taken as the threshold voltage $U_1$.

As seen from the data presented in Fig. 1, a change of the point material strongly affects the threshold voltage corresponding to 100% probability of the surface modification. It was established that the $U_1$ value varies linearly with the parameter $K = \alpha/\rho c'$ characterizing the point material (Fig. 2).

A relationship between the point material characteristics and the threshold voltage for the surface modification can be adequately explained within the framework of a model based on the thermal expansion mechanism. Indeed, it is the material and its properties that determine thermal expansion of the point heated with pulsed current passing upon voltage application to the point–surface contact. Therefore, the voltage-induced modification of the surface in contact with the points made of various materials is naturally characterized by different threshold pulse amplitudes. The smaller the $K$ value, the lower pulse voltage is sufficient to heat the point tip and form the point–surface contact.

Thus, the above relationship between $K$ and $U_1$ can be considered as additional evidence for validity of the surface modification mechanism based on the concept of contact formation between the point and sample surface as a result of thermal expansion of the point caused by its heating with the current passing in the point–sample circuit [6–8].

## REFERENCES

1. G. M. Shedd and P. E. Russel, Nanotechnology **1**, 67 (1990).
2. U. Staufer, R. Wiesendanger, L. Eng, *et al.*, Appl. Phys. Lett. **51**, 244 (1987).
3. C. S. Chang, W. B. Su, and T. T. Tsong, Phys. Rev. Lett. **72**, 574 (1994).
4. J. Méndez, J. Gómez-Herrero, J. I. Pascual, *et al.*, J. Vac. Sci. Technol. B **14**, 1145 (1996).
5. J. A. Dagata, J. Schneir, H. H. Harary, *et al.*, Appl. Phys. Lett. **56**, 2001 (1990).
6. G. G. Vladimirov, A. A. Drozdov, and L. M. Baskin, Pis'ma Zh. Tekh. Fiz. **21**, 66 (1995) [Tech. Phys. Lett. **21**, 426 (1995)].
7. L. M. Baskin, A. V. Drozdov, and G. G. Vladimirov, Surf. Sci. **369**, 385 (1996).
8. G. G. Vladimirov and A. V. Drozdov, J. Vac. Sci. Technol. B **15**, 482 (1997).
9. G. G. Vladimirov, A. V. Drozdov, and A. N. Rezanov, Pis'ma Zh. Tekh. Fiz. **22**, 67 (1996) [Tech. Phys. Lett. **22**, 764 (1996)].

*Translated by P. Pozdeev*

*Technical Physics Letters, Vol. 26, No. 5, 2000, pp. 377–379. Translated from Pis'ma v Zhurnal Tekhnicheskoĭ Fiziki, Vol. 26, No. 9, 2000, pp. 41–46.*


# Measurement of Time–Frequency Parameters of Picosecond Optical Pulses

**A. S. Shcherbakov and A. Yu. Kosarskiĭ**

*St. Petersburg State Technical University, St. Petersburg, 195251 Russia*

Received December 22, 1999

**Abstract**—A method is proposed that permits accurate and reliable measurement of the train-average pulse duration as well as the value and sign of the frequency chirp of picosecond optical pulses in high-repetition-rate trains. © *2000 MAIK "Nauka/Interperiodica".*

In investigations of the evolution of optical solitons in active and passive waveguide structures, a simple method is frequently required for the measurement of current time–frequency parameters of low-power picosecond and subpicosecond optical pulses travelling in high-repetition-rate trains. Most widely used is a method based on the formation of a train-average autocorrelation function of the field strength, which is coupled through the Fourier transform with the spectral power density. From the recorded power spectral density, one can determine an average width of the radiation spectrum. However, in this case, information on the average field phase is lost and it is impossible to determine the time variation of the field amplitude $A(t)$. Exact determination of the train-average pulse duration from the width of the radiation spectrum is only possible when the shape of the pulse envelope is known a priori and, in addition, the pulse spectrum is limited [1]. An approximated estimate of the pulse duration is also correct [2–4] if the frequency chirp is sufficiently small. In the general case, it is necessary either to pass to determination of the function autocorrelation intensity [5] or the cross-correlation functions [6, 7], or to take special measures to obtain information on the field phase, which often require the application of complicated experimental facilities or special computer algorithms [8–10]. The purpose of this work is to demonstrate possibilities of providing experimental conditions, under which the train-average autocorrelation function of the field strength can serve as a source of exact and reliable information on the average values of both duration and frequency chirp of low-power optical pulses travelling in high-repetition-rate trains.

We proceed from the assumption that all pulses in the train are identical and the pulse envelope $F(t)$ and the character of its frequency modulation are known:

$$A(t) = A_0 F(t) \exp\left(-\frac{ibt^2}{2\tau^2}\right), \qquad (1)$$

where $A_0$, $\tau$, and $b$ are the amplitude, duration, and frequency chirp of the pulse; $A_0 = \sqrt{P}$; and $P$ is the pulse peak power. These assumptions are not specific for the proposed method and are typical of most of the other measurement methods [5, 8]. For a Gaussian envelope, the relationships between the train-average pulse parameters $\tau$ and $b$ and the autocorrelation function with $T$ measured on a level of $\exp(-0.5) \approx 0.606$ are given by

$$F(t) = \exp\left(-\frac{t^2}{2\tau^2}\right), \quad \tau = T\sqrt{\frac{1+b^2}{2}}. \qquad (2)$$

Usually, the real-time autocorrelation function of the field strength averaged over a train of optical pulses is obtained with a scanning Michelson interferometer [1–4], which allows one to measure the value of $T$. However, it follows from formula (2) that information on the width $T$ of the field strength autocorrelation function is insufficient to determine the time–frequency parameters of the train pulses. We propose to perform two additional measurements of the autocorrelation function width $T$ with the help of a scanning Michelson interferometer. During the second and third measurement, additional optical elements, changing parameters $\tau$ and $b$ in a predetermined way but not influencing the envelope $F(t)$ of investigated pulses, should be placed in front of the beam-splitting mirror. The autocorrelation function widths $T_m$ ($m$ = 1, 2) obtained from the repeated measurements are coupled with the new values of pulse duration $\tau_m$ and frequency chirp $b_m$ through formula (2). Assume that $\tau_m = a_m\tau_0$ and $b_m = b_0 + \beta_m$, where $\tau_0$ and $b_0$ are the unknown values of parameters $\tau$ and $b$ and the quantities $a_m$ and $\beta_m$ are determined by additional optical elements. Using the above relationships, we can obtain two different quadratic equations for the quantity $b_0$. The corre-

1063-7850/00/2605-0377$20.00 

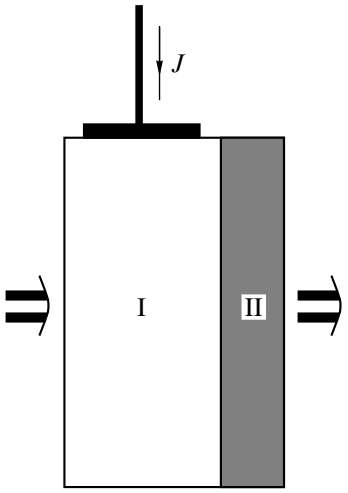


**Fig. 1.** Additional semiconductor optical element comprising (I) zone of linear amplification controlled by the pumping current $J$ and (II) zone of fast absorption saturation.

sponding solutions are given by the formulas

$$b_0 = (q_m a_m^2 - 1)^{-1} \times [\beta_m \pm \sqrt{q_m a_m^2(\beta_m^2 + 2) - (q_m^2 a_m^4 + 1)}], \quad (3)$$

where $q_m = T_0^2 T_m^{-2}$ and $T_0$ is the width of the field strength autocorrelation function obtained without additional optical elements. For $m = 1$ and 2, expressions (3) give four $b_0$ values, of which two coincide with each other and correspond to the true value of the train-average frequency chirp of the pulses. The proposed measurement method allows one to determine not only the value, but the sign of the frequency chirp as well, which is often impossible even with the help of substantially more complicated methods, such as, for example, the method described in [9]. Once the pulse frequency chirp $b_0$ is determined, one can use formula (2) to calculate the pulse duration $\tau$ by setting $T = T_0$ and $b = b_0$.

For the additional controlled optical element, it is recommended to use a device based on an InGaAsP single-mode travelling-wave semiconductor laser heterostructure, which is similar to a saturable-absorber laser [11] with clarified faces. The device comprises two zones (Fig. 1). Zone I of the linear amplification controlled by pumping current $J_m$ has the length $L_1$ and is characterized by the low-signal gain factor $\kappa_1(J_m)$. Zone II of fast absorption saturation, created by the deep implantation of oxygen ions into the output end of the heterostructure, has the length $L_2$ and is characterized by the low-signal absorption coefficient $\kappa_2$ and the saturation power $P_{sat}$. Zone I can modify the peak power $P_m$ of pulses entering zone II: $P_m = P\exp[\kappa_1(J_m)L_1]$. The peak power $P_m$ determines, in its turn, the values of parameters $a_m$ and $\beta_m$ reflecting the action of zone II on the pulses. In this case, $a_m = (\sqrt{2}\,\rho P_m + 1)^{-1/2}$ and $\beta_m = -\sqrt{2}\,\zeta\rho P_m$, where $\zeta = 5$ (see [12]) is the absorption line broadening coefficient and $\rho = (2P_{sat})^{-1}\kappa_1 L_1$ is the absorption parameter which, judging from data reported in [11], may be of the order of $\rho \le 1\ \mathrm{W}^{-1}$.

Such a device makes it possible to perform repeated measurements without readjustment of the optical circuit and ensures additions up to $\beta_m \le 5.0$ to the frequency chirp. The shape of the pulse envelope at the output of the additional semiconductor element is retained with sufficient accuracy.

Figure 2 demonstrates variation of the autocorrelation function after insertion of an additional electron-controlled semiconductor optical element into the measurement circuit. It shows calculated oscillograms of the autocorrelation functions of Gaussian pulses

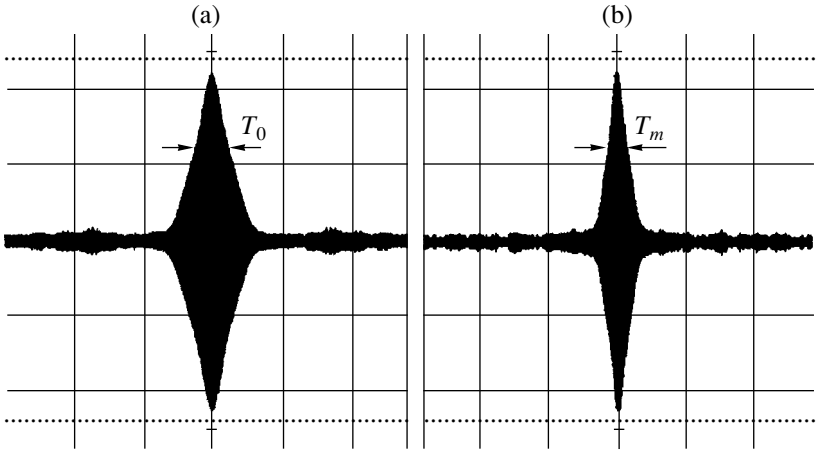


**Fig. 2.** Results of numerical simulation of the formation of an autocorrelation function in the scanning Michelson interferometer (a) without and (b) with an additional optical element included in the measurement circuit.

formed in a scanning Michelson interferometer (a) without and (b) with inserted semiconductor element (for the case of $\beta_m = -2$). Arrows mark a level of exp(–0.5) used to determine the $T$ value. The numerical simulation was performed for a signal-to-noise ratio of 10, which corresponds to typical experimental conditions [2–4]. Data obtained from triply repeated measurements of $T$ allows us to determine the pulse duration in a range of 1–50 ps and the pulse frequency chirp in a range of 0–±10 with an account for the chirp sign. The measurement accuracy is determined by the instability of radiation source and uncertainty of the scanning circuit characteristics, as well as by errors arising during the recording. The total measurement errors for both the pulse duration and the frequency chirp do not exceed 5%. In conclusion, we should note that this method can also be used to measure the time–frequency parameters of pulses with envelope of the type $F(t) = \mathrm{sech}\left(\frac{t}{\tau_S}\right)$ (where $\tau_S$ is the pulse duration measured on a level of sech(1) = 0.65), which is typical of picosecond optical solitons. Such an envelope can be well approximated by the Gaussian function with the relationship between durations $\tau_0 = 2^{1/4}\tau_S$ [13].

Thus, we demonstrated that the proposed method allows one, using the autocorrelation function for the field strength formed by the Michelson interferometer, to perform an exact and reliable measurement of train-average pulse duration as well as the value and sign of the frequency chirp of picosecond optical pulses travelling in high-repetition-rate trains.

## REFERENCES


1. A. S. Shcherbakov, Pis'ma Zh. Tekh. Fiz. **19**, 34 (1993) [Tech. Phys. Lett. **19**, 615 (1993)].
2. I. A. Knyazev, A. S. Shcherbakov, Yu. V. Il'in, *et al.*, Pis'ma Zh. Tekh. Fiz. **17**, 14 (1991) [Sov. Tech. Phys. Lett. **17**, 82 (1991)].
3. E. I. Andreeva, A. S. Shcherbakov, I. É. Berishev, *et al.*, Pis'ma Zh. Tekh. Fiz. **18**, 23 (1992) [Sov. Tech. Phys. Lett. **18**, 803 (1992)].
4. A. S. Shcherbakov and E. I. Andreeva, Pis'ma Zh. Tekh. Fiz. **20**, 44 (1994) [Tech. Phys. Lett. **20**, 873 (1994)].
5. É. Ippen and Ch. Schenk, in *Ultrashort Light Pulses*, Ed. by S. Shapiro (Springer, Heidelberg, 1977; Mir, Moscow, 1980).
6. J. E. Rothenberg, IEEE J. Quantum Electron. **22**, 174 (1986).
7. J. E. Rothenberg and D. Grischkowsky, Opt. Lett. **12**, 99 (1987).
8. J.-C. Diels, J. J. Fontaine, I. C. McMichael, and F. Simoni, Appl. Opt. **24**, 1270 (1985).
9. K. Naganuma, K. Mogi, and H. Yamada, IEEE J. Quantum Electron. **25**, 1225 (1989).
10. D. J. Kane and R. Trebino, Proc. SPIE **1861**, 150 (1993).
11. A. B. Zhuravlev, A. G. Plyavenek, E. L. Portnoĭ, *et al.*, Fiz. Tekh. Poluprovodn. (Leningrad) **22**, 1208 (1988) [Sov. Phys. Semicond. **22**, 766 (1988)].
12. G. P. Agrawal and N. A. Olsson, IEEE J. Quantum Electron. **25**, 2297 (1989).
13. D. Anderson, Phys. Rev. A **27**, 3135 (1983).


*Translated by A. Kondrat'ev*

*Technical Physics Letters, Vol. 26, No. 5, 2000, pp. 380–381. Translated from Pis'ma v Zhurnal Tekhnicheskoĭ Fiziki, Vol. 26, No. 9, 2000, pp. 47–51.*


# A Simple Method for Monitoring Ohmic Contacts in FET Heterostructures

**M. A. Stovpovoĭ**

*Institute of Semiconductor Physics, National Academy of Sciences of Ukraine, Kiev, 252028 Ukraine*

Received September 15, 1999

**Abstract**—A simple method is proposed for determining positions of the fusion fronts in a conductor, which can be implemented in the FET technology. *© 2000 MAIK "Nauka/Interperiodica".*

Ohmic contacts are among the major elements of the field-effect transistors (FETs) determining their noise and gain characteristics. The ohmic contacts of high electron mobility transistors (HEMTs) exhibit certain distinguishing features in comparison with the contacts of usual GaAs-based FETs. In particular, the main contact criterion in the GaAs–GaAlAs structures used as a base of HEMTs is the depth of the fusion front relative to the dopant distribution profile.

The fusion front in HEMTs must reach the depth of the two-dimensional gas localization [1, 2], which makes determination of the fusion front position in a semiconductor structure an important task. Solving this task by direct methods is rather difficult and can be reached only by the depth profiling using fine analytical tools such as the Auger electron spectroscopy (AES) or secondary ion mass spectrometry (SIMS). Unfortunately, these destructive methods are complicated, labor-consuming, and require preparation of special test samples.

The purpose of this work was to develop a comparatively simple method capable of monitoring the position of ohmic contacts immediately during the technological process of FET heterostructure formation.

Heterostructures of the $n^+$-GaAs, $n^+$-GaAlAs, $n$-GaAlAs, $n$-GaAs (i), and $n$-GaAs (ii) types with the thicknesses 60 nm, 50 nm, 3 nm, 0.5 μm, and 300 μm, respectively, were grown by the molecular-beam epitaxy (MBE) technique. The electron mobility in the two-dimensional electron gas region was ~4000 $cm^2/(V\ s)$ at 300 K and increased to about 40000 $cm^2/(V\ s)$ at 77 K. The control samples of the $n^+$-GaAs, $n$-GaAs (i), $n$-GaAs (ii), and $n$-GaAs (iii) types with the thicknesses 0.25, 0.25, 0.75, and 300 μm, respectively, were grown by the liquid-phase epitaxy (LPE) method. The samples were prepared using conventional technological regimes (see, e.g., [3]). The sample heat treatment conditions were as follows: fusion temperature 410°C, fusion time 30 and 60 s (samples 1 and 2, respectively); 430°C and 25, 40, 25 s (samples 3–5, respectively). Then, the samples were etched in a strongly diluted ammonia–peroxide solution, whereby the surface metallization layers served as masks. During this, semiconductor was gradually (at a step of 1 s) removed from the region between contacts A and B (in control samples, C and D) and a total resistance between the contacts was measured in every step at room (300 K) and liquid-nitrogen (77 K) temperatures.

Figure 1 shows experimental plots of the ratio of resistances $R$(300 K)/$R$(77 K) versus the etching time. Let us consider the behavior of this ratio. As seen, resistance of the control GaAs structure (sample 5) is virtually unchanged (a 5–7% variation in the initial state and in the course of etching). Behavior of the heterostructures exhibits principal difference both from that of the control sample and between each other.

Sample 1 shows a relatively small decease in resistance upon removal of the $n^+$-GaAs and $n^+$-GaAlAs lay-

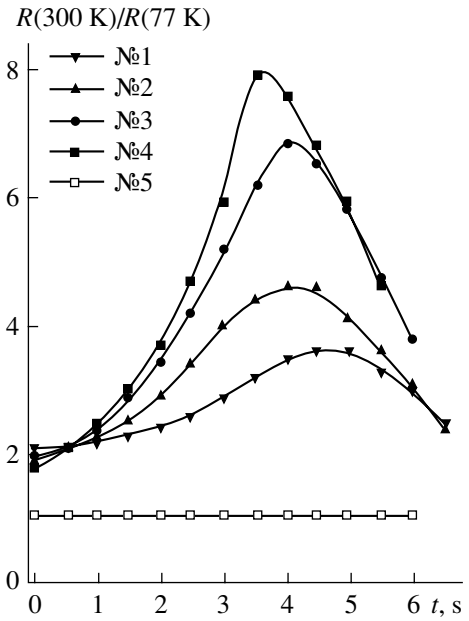


**Fig. 1.** The experimental plots of the ratio of resistances $R$(300 K)/$R$(77 K) versus the etching time for samples 1–5 (see the text for explanations).

1063-7850/00/2605-0380$20.00 © 2000 MAIK "Nauka/Interperiodica"

ers between contacts, from which we infer that the fusion front in this sample did not reach the two-dimensional electron gas region. A large serial resistance of the $n^+$-GaAlAs layer separating the fusion front from the two–dimensional electron gas region masks a decrease in resistance of the latter region upon cooling from 300 to 77 K.

Sample 2 exhibits a greater change in the resistance, which indicates that the fusion front penetrated deeper into the sample but yet not reached the two–dimensional electron gas region (the serial resistance of the $n^+$-GaAlAs layer is lower than that in sample 1 and the behavior of the electron gas is manifested to a greater extent).

In sample 4, the maximum value of the ratio $R(300\ \mathrm{K})/R(77\ \mathrm{K})$ is somewhat greater than that in sample 3 and corresponds by the order of magnitude to the growth in the electron mobility in the two-dimensional electron gas region upon cooling the structure from 300 to 77 K. We believe that the fusion front in samples 3 and 4 reached the two–dimensional electron gas region. A kind of saturation observed in the decrease of resistance on cooling apparently indicates that the fusion front has reached the two– dimensional electron gas region. Lying below this region are the undoped buffer layer and a semiinsulating substrate carrying negligibly small currents (as compared to those in the $n^+$-GaAs layer and the two–dimensional electron gas region).

In the initial state (prior to etching), samples 1–4 possess virtually equal total resistances determined primarily by contribution of the highly-doped $n^+$-GaAs layer. This layer, possessing a small resistance weakly dependent on the temperature (see Fig. 1, the curve of sample 5), shortens the two– dimensional electron gas region even at 77 K. As the $n^+$-GaAs layer is gradually etched off, the two–dimensional electron gas behavior (with a tenfold increase in the carrier mobility and the corresponding drop in resistance upon cooling from 300 to 77 K) becomes more pronounced. When the $n^+$-GaAs layer is completely removed and the $n^+$-GaAlAs layer (representing a source of electrons for the two–dimensional electron gas region) is involved, the two–dimensional electron gas region exhibits depletion leading to a sharp growth of the sample resistance both at 300 and 77 K. Finally, the $n^+$-GaAlAs layer is also removed and the sample resistance variation is determined by the properties of undoped GaAs, approaching behavior of the control sample 5.

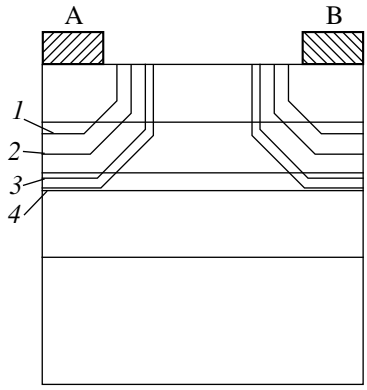


**Fig. 2.** Schematic diagram of the model of fusion front penetration into a FET heterostructure for samples 1–4.

Note that, as the heat treatment regime becomes more rigid, the maximum of the resistance ratio $R(300\ \mathrm{K})/R(77\ \mathrm{K})$ shifts on the left. This is probably explained by increasing lateral diffusion in the heat treated samples, which somewhat reduces the effective gap width between metal contacts. Analysis of the curves presented in Fig. 1 allowed us to propose a model describing the fusion front penetration into FET heterostructures, which is schematically depicted in Fig. 2.

Data of the AES depth profiling of the ohmic contacts in the heterostructures studied showed that the heat treatment at $T = 410°\mathrm{C}$ allows the fusion front to reach a depth of 50–60 nm after 30 s and 80–90 nm after 60 s. Therefore, the results obtained by our method well agree with the data of fine analytical investigations. Thus, we have developed a comparatively simple method for evaluation of the fusion front penetration depth in the course of ohmic contact formation in HEMTs. The proposed procedure does not involve special test structures, requires comparatively short time, and can be performed directly on a semiconductor wafer employed in the technological process.

## REFERENCES

1. S. J. Lee and C. R. Crowell, Solid-State Electron. **28**, 659 (1985).
2. A. J. Hill and P. H. Ladbrooke, GEC J. Res. **4**, 1 (1986).
3. V. I. Osinskiĭ and M. A. Stovpovoĭ, Optoélektron. Poluprovodn. Tekh. **29**, 18 (1995).

*Translated by P. Pozdeev*

*Technical Physics Letters, Vol. 26, No. 5, 2000, pp. 382–385. Translated from Pis'ma v Zhurnal Tekhnicheskoĭ Fiziki, Vol. 26, No. 9, 2000, pp. 52–59.*


# Effect of Metal Clusters on the Absorption and Emission Spectra of High-Density Sodium Vapors

**A. G. Leonov, A. A. Rudenko, A. N. Starostin, and D. I. Chekhov**

*Moscow Physicotechnical Institute, Dolgoprudnyĭ, Moscow oblast, 141700 Russia*

*Troitsk Institute of Innovation and Thermonuclear Investigations (TRINITI), Troitsk, Moscow oblast, 142092 Russia*

Received December 7, 1999

**Abstract**—The optical absorption spectra of high-density ($10^{16}$–$10^{19}$ cm$^{-3}$) sodium vapors were studied in a broad spectral range (0.35–1.1 μm). The intensity of thermal radiation from sodium vapors was measured in the 2–3 μm wavelength interval. It is established that the effect of metal clusters can account neither for the observed structure of absorption spectra nor for the increased intensity of emission in the near-IR range reported in some works (in particular, for the emission spectra of high-pressure gas-discharge sodium lamps). © *2000 MAIK "Nauka/Interperiodica".*

The optical properties of alkali metal vapors are of importance from the standpoint of various applications and have been extensively studied. Nevertheless, there are still many open questions concerning the origin and structure of some regions in the absorption and emission spectra of these objects, For example, there is a long discussion about the nature of intense emission in the near-IR range observed for the high-pressure gas-discharge sodium lamps [1] widely used for illumination. Inefficient IR losses, which may account for up to 20–30% in the total energy balance of these sources, were referred to as "mysterious" [2]. Not one of the existing theoretical models can provide for at least a qualitative explanation of this phenomenon.

Intense IR emission was also observed in the spectra of purely thermal radiation from the high-density vapors of potassium [3] and sodium [4]. A theoretical model developed in [4] for explanation of the far-IR wings of D-lines in the spectra of sodium vapors, based on the Boltzmann spectral distribution of the population of resonance levels [4, 5] described the experimental results to within the order of magnitude. In contrast to this, deviation of the conventional theory of the radiation transfer [6] from experimental data in the region of $\Delta\omega \sim \omega$ reached 4–5 orders of magnitude (here $\Delta\omega = \omega - \omega_0$ is the frequency deviation, and $\omega$ and $\omega_0$ are the current and resonance frequencies). However, the model proposed in [4] was based on the assumption that the line contour is related to quasistatic broadening due to the buffer gas, which is not as obvious in the region of large frequency deviations. Thus, the question concerning the origin of intense IR emission from high-density vapors of alkaline metals is still open.

It was suggested [3] that this emission might be due to the possible presence of metal clusters that can form under nonequilibrium conditions in a stream of potassium vapors [3], in a heated cell of the "thermal tube" type [7] (also used for the obtaining of high-density sodium vapors in [4]), and in high- pressure gas-discharge sodium lamps. It should be noted that this point is also of interest from the standpoint of development of the cluster lamps [8] by offering possibility of creating radiation sources with optimum and controlled spectral characteristics.

The possible effect of metal clusters on the optical characteristics of high-density sodium vapors can be estimated by measuring the absorption spectra. Indeed, sufficiently large (albeit still small compared to the emission wavelength) sodium clusters must exhibit a resonance absorption peak in the UV range (near 0.4 μm) due to the surface plasmon excitation. In order to verify the hypothesis concerning the cluster effect, we have studied for the first time the optical absorption spectra of high-density ($10^{16}$–$10^{19}$ cm$^{-3}$) sodium vapors in a broad spectral range (0.35–1.1 μm) and measured the intensity of thermal radiation from sodium vapors in the IR (2–3 μm) wavelength interval.

The experiments were performed in a system comprising a cylindrical cell of the "thermal tube" type with the active region length $L$ = 15 cm and a set of special equipment described in more detail elsewhere [4]. Prior to the spectral measurements, the cell containing a source of metal sodium was evacuated to a residual vacuum of $10^{-5}$ Torr, filled with an inert gas (argon or helium) to a pressure of 0.1–1 atm, and heated to a required temperature. In order to determine the optical absorption of metal vapors, the intensity of a signal $I_0$ transmitted through the cell at room temperature was also measured in each experiment. The absorption coefficient was determined by the formula

$$K = -z_{\text{eff}}^{-1}\ln((I - I_v)/I_0), \quad (1)$$

where $I$ is the intensity of radiation transmitted through the cell with sodium vapors at a given temperature, $I_v$ is the intensity of intrinsic emission from sodium vapors (in all experiments $I_v$ was negligibly small compared to $I$), $z_{\text{eff}} = (1/T_c)\int T(z)dz$ is the effective length of the active zone determined with an allowance for the measured temperature profile in the cell, and $T_c$ is the temperature at the center of the cell.

The results of the optical absorption measurements are presented in Figs. 1 and 2. Figure 1 shows the optical absorption spectrum of sodium vapors measured in the range from 0.35 to 1.1 μm for three values of $T_c$. As is seen from these plots, the spectrum exhibits three clearly pronounced regions of absorption. The first, with a center at $\lambda = 0.59$ μm, corresponds to absorption die to the resonance transition $3S$–$3P$. The second band, which is centered at 0.49 μm, represents absorption primarily due to the molecular transition $X^1\Sigma_g^+$–$B^1\Pi_u$ in the $Na_2$ dimer. The third region represents a broad absorption band at 0.6–0.82 μm, which corresponds to the $A^1\Sigma_u^+$–$X^1\Sigma_g^+$ transition in the sodium dimer. In addition, there is certain increase in absorption in the short-wavelength region ($\lambda < 0.37$ μm), which is due to proximity of the $3S$–$4P$ atomic transition ($\lambda = 0.330$ μm). However, no distinct peaks that could be assigned to absorption in the sodium clusters were observed in the region of 0.4 μm, although we may still suggest that this absorption is masked by the wings of strong absorption bands indicated above.

The results of our measurements presented in Figs. 1 and 2 also show a significant absorption in the region of 0.9–1.1 μm where, according to the theoretical calculations [3, 10, 11] based on the potential curves of $Na_2$ obtained in [12], no absorption bands of molecular sodium are expected. The absorption at 0.9 μm corresponds to a long-wavelength edge of the absorption–emission band for a free-bound transition $a^3\Sigma_u^+$–$c^3\Sigma_g^+$ [3, 10, 11]. Note that the atomic absorption lines of Na cannot be manifested in this region either because of a negligibly small thermal population of the resonance and higher levels in the absence of external excitation.

Therefore, we have to conclude that the absorption in the region of 0.9–1.1 μm must be related to some other factors, in particular, to the above-mentioned absorption in sodium metal clusters. In order to estimate this possibility at maximum, let us assume that, despite the absence of clearly pronounced peaks in the region of 0.4 μm, all the absorption in this region is due to clusters. Then, we may estimate the value of this coefficient for the near-IR range using formulas for the spectral dependence of the absorption coefficient of metal clusters [9]. According to this, the absorption coefficient of a gas composed of spherical metal clusters with a radius $r(r \ll \lambda)$ can be determined from the following expression

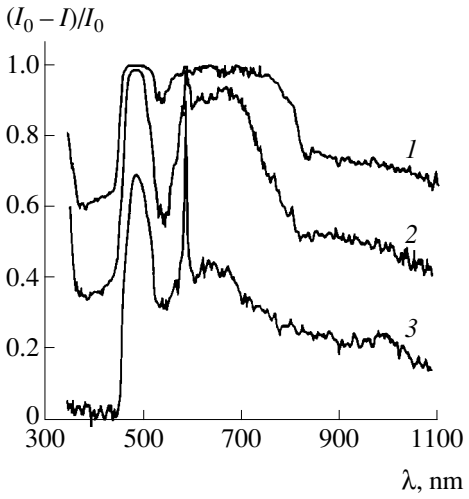


**Fig. 1.** Experimental absorption spectra of sodium vapors measured for various temperatures at the center of the cell $T_c$ = 903 (*1*), 806 (*2*), 709 K (*3*).

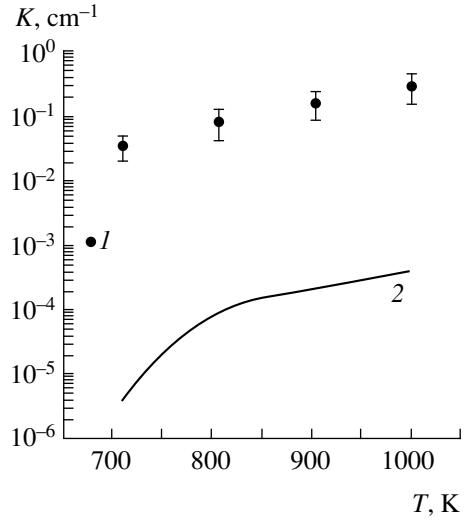


**Fig. 2.** The plot of absorption coefficient at $\lambda = 1.0$ μm versus temperature at the center of the cell: (*1*) experimental data; (*2*) upper estimate calculated for clusters.

$$K(\bar{\lambda}) = (18\pi Q/\lambda)\varepsilon_2((\varepsilon_1 + 2)^2 + \varepsilon_2^2)^{-1}, \qquad (2)$$

where $Q = \int (4/3)\pi r^3 f(r)dr$ is the volume fraction of clusters, $f(r)$ is the function of cluster size distribution, $N = \int f(r)\,dr$ is the number of clusters per unit volume, $\varepsilon_1$ and $\varepsilon_2$ are the real and imaginary parts of the complex permittivity of metal sodium (see [9]). Formula (2) has a Lorentzian resonance character, with the value $\varepsilon_1 = -2$ determining the absorption peak position. Note that, according to [13], for $Q \ll 1$, this formula ade-

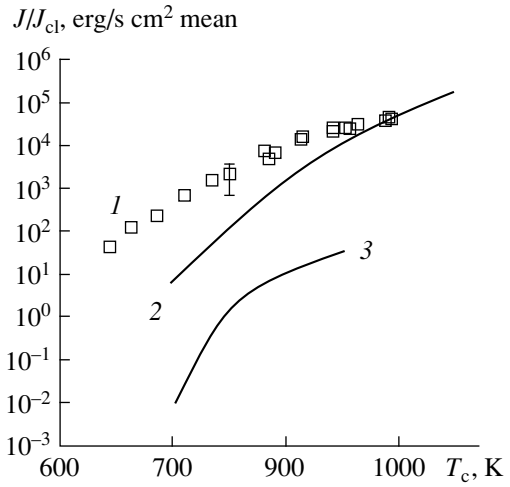


**Fig. 3.** The plot of integral intensity of emission from sodium vapors in the IR range versus temperature at the center of the cell: (*1*) experimental data; (*2*) theoretical calculation according to a model proposed in [4, 5]; (*3*) upper estimate calculated for clusters.

quately describes the absorption in silver clusters for a broad spectral range up to the far-IR region.

Assuming the absorption coefficient at $\lambda = 0.4$ μm equal to the measured value (Fig. 1) and substituting this into formula (2), we obtain an upper estimate for the $Q$ value, which varies from $6.6 \times 10^{-10}$ (at $T_c$ = 709 K) to $6.1 \times 10^{-8}$ ($T_c$ = 1000 K). Using these values of the maximum volume fraction of clusters, we may obtain an upper estimate for the spectral dependence of the absorption coefficient of sodium clusters and, in particular, estimate the $K$ value at a wavelength of 1.0 μm fort various vapor temperatures. The results of these calculations are presented by the curve in Fig. 2. A comparison of the theory and experiment shows that, under the assumptions adopted above, the absorption in clusters extrapolated to the near-IR spectral region is negligibly small (two orders of magnitude lower) as compared to the measured values. If the absorption measured in the near-IR region were nevertheless assigned to clusters, than analogous extrapolation of the absorption coefficient to the UV region would yield a value two orders of magnitude greater than the experimentally observed one. This would imply that the metal vapor column must be absolutely nontransparent in the wavelength gage studied.

Figure 3 presents experimental data on the integral intensity $J$ of emission from sodium vapors in the wavelength region of 2–3 μm. In this spectral interval, no direct measurements of the optical absorption were possible under our experimental conditions. For this reason, the experimental data were compared to the extrapolated curve of the absorption coefficient of clusters by recalculating $K(\lambda)$ to the emissive ability of clusters $E(\lambda)$ with the aid of Kirchhoff's formula

$$E(\lambda) = K(\lambda)F(\lambda), \quad (3)$$

where $F(\lambda) = (c^2/4\pi^3)(\exp(\hbar\omega/kT) - 1)^{-1}$ is the Planck emission intensity. For the comparison with experiment, we have calculated the values

$$J_{cl} = \int (S(\lambda)E(\lambda)d\lambda, \quad (4)$$

where $S(\lambda)$ is the known spectral characteristic of IR detector and the integration is performed over the detector sensitivity band.

The calculated emission characteristics $J_{cl}$ are also depicted in Fig. 3. A comparison of theory with experiment shows that, in the entire range of vapor temperatures, the calculated $J_{cl}$ values are lower by several orders of magnitude than the measured ones. Accordingly, the extrapolated absorption coefficient is also lower by two orders of magnitude than the real absorption measured in sodium vapors. For the comparison, Fig. 3 also shows a theoretical curve of emission from sodium vapors constructed using a model proposed in [4, 5].

Thus, the hypothesis that a considerable number of metal clusters, corresponding to the description proposed in [8, 9], may form in the thermal tube provides no adequate interpretation of the experimental data on the optical properties of high-density sodium vapors in the near-IR spectral range. Data available on the absorption and emission of $Na_2$ molecules also cannot explain features observed in the IR absorption and emission spectra. As a result, the question concerning the formation of absorption and emission spectra of high-density sodium vapors in the near-IR range also remain open. We may suggest that the spectral features observed in our work, as well as those reported in [3, 4], can be related to low-molecular sodium oligomers such as $Na_3$, $Na_4$, etc. (this possibility was already mentioned in [14]), the absorption properties of which cannot be described by a simple formula (2) applicable to usual metal clusters. On the other hand, these features can be related to a multiparticle shift of the resonance line frequency, which would significantly modify the resonance absorption line contour as compared to that corresponding to a simple quasistatic model taking into account only pair collisions within the framework of the nearest-neighbor approximation. All these factors require additional investigation.

This work was supported by the Russian Foundation for Basic Research, project no. 99-02-18176.

## REFERENCES

1. G. N. Rokhlin, *Gas-Discharge Light Sources* (Énergoatomizdat, Moscow, 1991).
2. D. O. Wharmby, IEE Proc., Part A: Phys. Sci., Meas. Instrum., Manage. Educ. **127**, 165 (1980).
3. J. Huennekens, S. Schaefer, M. Ligare, and W. Happer, J. Chem. Phys. **80**, 4794 (1984).
4. Yu. K. Zemtsov, A. Yu. Sechin, A. N. Starostin, *et al.*, Zh. Éksp. Teor. Fiz. **114**, 135 (1998) [JETP **87**, 76 (1998)].

5. Yu. K. Zemtsov and A. N. Starostin, Zh. Éksp. Teor. Fiz. **103**, 345 (1993) [JETP **76**, 186 (1993)].
6. L. M. Biberman, V. S. Vorob'ev, and I. T. Yakubov, *Nonequilibrium Low-Temperature Plasma Kinetics* (Nauka, Moscow, 1982).
7. C. R. Vidal and J. Cooper, J. Appl. Phys. **40**, 3370 (1969).
8. B. M. Smirnov, Usp. Fiz. Nauk **167**, 1169 (1997) [Phys. Usp. **40**, 1117 (1997)].
9. Yu. I. Petrov, *Physics of Small Particles* (Nauka, Moscow, 1982).
10. J. P. Woerdman and J. J. De Groot, Chem. Phys. Lett. **80**, 220 (1981).
11. M. Ligare and J. B. Edmonds, J. Chem. Phys. **95**, 3857 (1991).
12. D. D. Konovalov, M. E. Rozenkrantz, and M. L. Olson, J. Chem. Phys. **72**, 2612 (1980).
13. R. P. Devaty and A. J. Sievers, Phys. Rev. B **41**, 7421 (1990).
14. A. Vasilakis, N. D. Bhaskar, and W. Happer, J. Chem. Phys. **73**, 1490 (1980).

*Translated by P. Pozdeev*

*Technical Physics Letters, Vol. 26, No. 5, 2000, pp. 386–388. Translated from Pis'ma v Zhurnal Tekhnicheskoĭ Fiziki, Vol. 26, No. 9, 2000, pp. 60–64.*


# Thermostimulated Exoelectron Emission from Uranium-Activated LiF and NaF Crystals

**A. I. Slesarev[1], A. A. Zhamangulov[2], M. M. Kidibaev[2], V. S. Kortov[1], and B. V. Shul'gin[1]**

[1] *Ural State Technical University, Ekaterinburg, 620002 Russia*

[2] *Issyk-Kul State University, Karakol, Kirgiz Republic*

Received November 16, 1999

**Abstract**—New high-temperature peaks of thermostimulated exoelectron emission (TSEE) from uranium-activated LiF and NaF Crystals were observed. TSEE parameters for various (Li,Na)– (U+Me) systems were determined. © *2000 MAIK "Nauka/Interperiodica".*

Uranium-activated lithium and sodium fluoride (Li,Na)–U crystals belong to a class of unique polyfunctional materials [1–5]. Related coactivated compositions (Li,Na)–U(Me) (where Me = Cu, Zn, Ti, Pb, Sc, Sr) were used for the creation of thermoluminescent, scintillation, absorption, paramagnetic-resonance, and thermoexoemission detectors of electromagnetic and corpuscular radiations, working elements for color center lasers, and the optical media for data recording and storage [5]. Materials based on (Li,Na)–U(Me) crystals, developed for the thermoexoemission detectors capable of operating at elevated temperatures, are also of interest from the standpoint of high-temperature dosimetry of ionizing radiations. There are special cases (e.g., radiation control in superdeep bore holes and radioactive waste storages, where the temperature may rise up to 200°C and above) in which thermoexoemission detectors may be advantageous.

According to the results of previous investigations, the high-temperature thermostimulated exoelectron emission (TSEE) peaks were observed at 613 K (340°C) in LiF–U(Me) and 663–673 K (390–400°C) in NaF–U(Me) crystals [5]. However, our TSEE measurements for the known and new compositions based on LiF–U and NaF–U crystals with coactivators showed evidence that TSEE peaks may exist at still higher temperatures. Below, we report on the results of these investigations.

**Sample preparation.** The experiments were performed with LiF–(U+Cu), LiF–(U+Sr), NaF–(U+Cu), and NaF–(U+Sr) crystals grown by the Kiropulos method from a special-purity charge at the Institute of Physics (National Academy of Sciences of Kirgizstan). The content of activators in the charge was 0.01–0.1 mol %. The samples, cleaved from single-crystal ingots, had the shape of 10 × 10-mm squares with a thickness of 0.3–0.4 mm. Prior to measurements, the plates were annealed for 10 min at $T$ = 800 K.

**Instrumentation.** The TSEE measurements were performed in a vacuum of ~$10^{-5}$ Pa using an automated exoemission spectrometer [6]. The samples were irradiated for 1 s with 1-keV electrons at a beam current density of ~1 μA/cm$^2$ and then heated at a linear temperature growth rate of ~20 K/s. The TSEE spectra were measured and processed with the aid of a computer using the PROCESS program [7]. Complex spectra were separated into elementary bands upon smoothening of the envelopes performed assuming the first-order process kinetics. The TSEE activation energy was calculated using halfwidths of the elementary emission bands obtained upon decomposition of the initial spectrum.

**Results and discussion.** The curve of TSEE from LiF–(0.01U+0.1Cu) measured in the temperature interval 300–650 K (Fig. 1) shows a high yield of electron emission at 320–450 K. The activation energy of trapping centers responsible for these emission peaks is 0.7–0.9 eV (see table). A characteristic feature of TSEE from the LiF–(U+Cu) crystals is the high-intensity nonoverlapping emission at 543 K with the activation energy $E \cong 1.17$ eV. If only deep traps are filled by high-

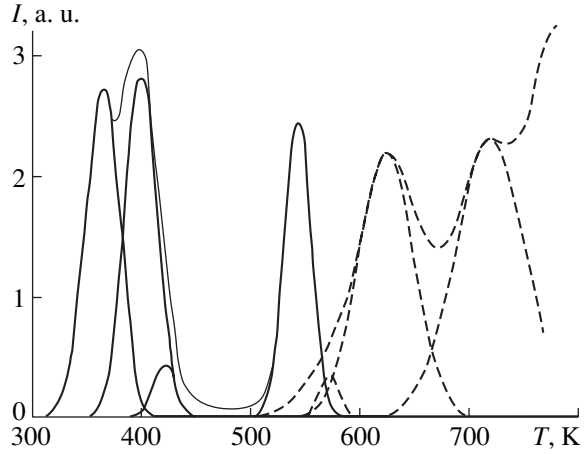


**Fig. 1.** Curves of thermostimulated exoelectron emission from electron-irradiated LiF–(U+Cu) crystals.

1063-7850/00/2605-0386$20.00 © 2000 MAIK "Nauka/Interperiodica"

temperature irradiation ($T \geq 450$ K), the TSEE curves exhibit additional peaks at 610 and 714 K and the onset of a peak at $T > 775$ K (Fig. 1, dashed curve). A small peak at ~573 K depicted in Fig. 1 is not explicitly manifested in the spectrum: this component was obtained upon decomposition of the total spectrum into elementary bands.

The TSEE curves of LiF–(0.01U+0.1Sc) display four overlapping bands with activation energies within 0.7–1.0 eV. The dominating peak, observed at 332 K, has $E = 0.72$ eV. No maximum was observed for this crystal in the region of 543 K (characteristic of the copper-containing samples).

The samples of LiF–(U+Sr) also exhibited high-temperature TSEE peaks (see table), with a new feature observed at 737 K. Figure 2a shows a typical TSEE curve of the LiF–(U+Sr) crystal. As seen from the data presented in Figs. 1, 2 and the table, the character of TSEE from the LiF–(U+Me) crystals depends on the type of metal-coactivator.

For the NaF–(U+Sr) crystals, the main TSEE yield is observed in the temperature interval 470–750 K (Fig. 2b). In this system, a new peak was observed at 702 K. This emission takes place from traps with an activation energy of 1.52 eV.

Analysis of the results obtained in this work, together with the data from [1], shows that the temperature interval of active thermionic emission from LiF–(U+Me) crystals coincides with that featuring thermal decomposition of both simple F-electron color centers and cluster color centers of the types $F_2$, $F_2^+$, and $F_3$ (with the absorption bands at 440, 643, and 834 nm, respectively. The temperature region corresponding to the onset of maximum decrease in emission from the $F_2$ centers ($\lambda = 440$ nm, the most intense band for all the cluster color centers) agrees with the main maximum observed in the TSEE curves (363–400 K). The high-temperature peaks of TSEE from LiF–(U+Me) are apparently related to degradation of the F and $F_A$ color centers (250 and 262 nm). Degradation of the electron color centers can be explained by their recombination with the hole centers (e.g., H-centers, representing interstitial halogen atoms), which exhibit increased thermal stability in the coactivated LiF–(U+Me) crystals. Hole centers of other types may also participate in degradation of the electron color centers.

For the crystals of NaF–(U+Me), where dominating cluster color centers are of the $F_3^+$ type ($\lambda = 518$ nm), the observed thermoactivation processes can be related to degradation of the $F^{3+}$ and F centers. The crystal samples studied in this work exhibited, in addition to TSEE, a thermostimulated luminescence with the optical emission peaks observed at approximately the same temperatures as the TSEE peaks. Finally, it should be noted that dependence of the TSEE peak intensity on the irradiation dose (checked for the samples irradiated with electron and X-ray beams) exhibits a linear portion for doses up to ~$10^3$ Gy. This behavior indicated that these crystals can be used in high-temperature thermoexoemission dosimeters intended for the radiation

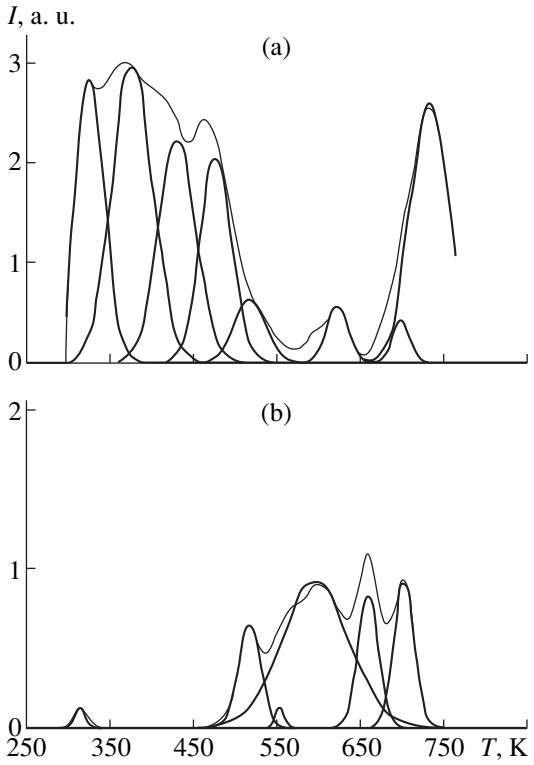


**Fig. 2.** Curves of thermostimulated exoelectron emission from electron-irradiated (a) LiF–(U+Sr) and (b) NaF–(U+Sr) crystals.

Parameters of thermostimulated exoelectron emission from LiF–(U + Me) crystals

| Crystal | $T_{max}$, K | Halfwidth, K | $E$, eV |
|---|---|---|---|
| LiF–(U+Cu) | 363 | 44 | 0.78 |
| | 399 | 40 | 0.86 |
| | 421 | 28 | 0.91 |
| | 543 | 36 | 1.17 |
| | 573 | 28 | 1.19 |
| | 610 | 80 | 1.32 |
| | 714 | 100 | 1.54 |
| LiF–(U+Sr) | 327 | 48 | 0.71 |
| | 377 | 68 | 0.81 |
| | 431 | 64 | 0.93 |
| | 477 | 52 | 1.03 |
| | 517 | 52 | 1.12 |
| | 623 | 36 | 1.34 |
| | 699 | 28 | 1.51 |
| | 737 | 68 | 1.59 |

control (e.g., in superdeep bore holes and radioactive waste storages.

## REFERENCES

1. W. A. Runciman, Nature **175** (4468), 39 (1955).
2. P. P. Feofilov, Opt. Spektrosk. **7**, 126 (1959).
3. A. A. Kaplyanskiĭ and N. A. Moskvin, Opt. Spektrosk. **13**, 542 (1962).
4. L. M. Belyaev, G. F. Dobrzhanskiĭ, and P. P. Feofilov, Izv. Akad. Nauk SSSR, Ser. Fiz. **25**, 548 (1961).
5. M. M. Kidibaev, *Radiation-Stimulated Processes in (Li, Na) F-U, Me Crystals* (ISBN 5–230–06574–5) (Issyk-Kul Univ., Karakol; Ural. Univ., Ekaterinburg, 1999).
6. V. S. Kortov, V. G. Isakov, A. I. Slesarev, *et al.*, Defektoskopiya, No. 1, 50 (1996).
7. V. G. Isakov, I. A. Glavatskikh, and V. S. Kortov, Defektoskopiya, No. 12, 14 (1998).

*Translated by P. Pozdeev*

*Technical Physics Letters, Vol. 26, No. 5, 2000, pp. 389–391. Translated from Pis'ma v Zhurnal Tekhnicheskoĭ Fiziki, Vol. 26, No. 9, 2000, pp. 65–69.*


# Criteria of Rigid Instability on a Flat Surface of Dielectric Fluid in External Electric Field

**N. M. Zubarev and O. V. Zubareva**

*Institute of Electrophysics, Ural Division, Russian Academy of Sciences, Ekaterinburg, 620219 Russia*

Received December 8, 1999

**Abstract**—Subcritical behavior of a free surface of the ideal dielectric liquid in an external electric field has been theoretically studied. A system of amplitude equations is obtained, which describe nonlinear interaction of three standing waves forming a hexagonal structure. Within the framework of a model described by these equations, a sufficient integral criteria are formulated for the rigid instability excitation on the flat surface of the liquid medium. © *2000 MAIK "Nauka/Interperiodica".*

As is known [1], a flat surface of a liquid dielectric medium exposed to a normal electric field becomes unstable if the electric field strength exceeds certain critical value given by the formula

$$E_c^2 = \frac{8\pi\varepsilon(\varepsilon+1)}{(\varepsilon-1)^2}\sqrt{g\alpha\rho},$$

where $g$ is the acceleration of gravity, $\alpha$ is the surface tension coefficient, $\rho$ is the density of medium, and $\varepsilon$ is the dielectric permittivity of the medium. For small values of the supercritical parameter $\delta = (E^2 - E_c^2)/E_c^2$, the system features increasing perturbations with the wavenumbers close to $k_0 = \sqrt{g\rho/\alpha}$. A nonlinear interaction between standing waves with the wavevectors forming angles multiple of $\pi/3$ drives the system to a state possessing hexagonal surface structure [2, 3].

It should be noted that the formation of a wavy surface relief is also possible in the subcritical region of field strengths (i.e., where $\delta < 0$), which is typical for the rigid excitation regime. The purpose of this work was to determine sufficient conditions for the rigid instability development caused by three-wave processes on the flat surface of a liquid dielectric medium.

Let us consider a potential motion of the ideal dielectric liquid, bounded by a free surface $z = \eta(x, y, t)$, in an external electric field directed along the $z$ axis. The velocity potential of the liquid $\Phi$ and the electric potentials of the liquid $\varphi$ and vacuum $\varphi'$ obey the Laplace equations

$$\Delta\Phi = 0, \quad \Delta\varphi = 0, \quad \Delta\varphi' = 0.$$

Since the functions $\eta(x, y, t)$ and $\Psi(x, y, t) = \Phi|_{z=\eta}$ are canonically conjugated values [3, 4], the equations of motion can be written in the Hamiltonian form

$$\frac{\partial\psi}{\partial t} = -\frac{\delta H}{\delta\eta}, \quad \frac{\partial\eta}{\partial t} = \frac{\delta H}{\delta\psi},$$

where the Hamiltonian function

$$H = \int\limits_{z\le\eta}\frac{(\nabla\Phi)^2}{2}d^3r - \int\limits_{z\ge\eta}\frac{(\nabla\varphi')^2}{8\pi\rho}d^3r - \int\limits_{z\le\eta}\frac{\varepsilon(\nabla\varphi)^2}{8\pi\rho}d^3r + \int\left[\frac{g\eta^2}{2} + \frac{\alpha}{\rho}\left(\sqrt{1+(\nabla\eta)^2}-1\right)\right]d^2r$$

coincides (to within a constant) with the total energy of the system. The system of equations is closed by the following boundary conditions

$$\varphi' \longrightarrow -Ez, \quad z \longrightarrow \infty,$$

$$\varphi \longrightarrow -\varepsilon^{-1}Ez, \quad z \longrightarrow -\infty,$$

$$\Phi \longrightarrow 0, \quad z \longrightarrow -\infty,$$

$$\varphi = \varphi', \quad z = \eta,$$

$$\frac{\partial\varphi}{\partial n} = \varepsilon^{-1}\frac{\partial\varphi'}{\partial n}, \quad z = \eta,$$

where $\partial/\partial_n$ denotes a derivative along the normal

Let us assume that the characteristic slope angles of the surface $|\nabla_\eta|$ are small. Then, upon writing the Hamiltonian in the form of a surface integral in terms of the Green function and expanding the integrand into series with respect to canonical variables $\eta$ and $\psi$, we obtain (to within higher powers of the small parameter)

$$H = \frac{1}{2}\int[\psi\hat{k}\psi + g\eta^2 + \alpha\rho^{-1}(\nabla\eta)^2]d^2r - \frac{E^2(\varepsilon-1)^3}{8\pi\rho\varepsilon(\varepsilon+1)^2}\int\left[\frac{(\varepsilon+1)}{(\varepsilon-1)}\eta\hat{k}\eta - \eta(\nabla\eta)^2 + \eta(\hat{k}\eta)^2\right]d^2r, \quad (1)$$

where $\hat{k}$ is the two-dimensional integral operator with a difference nucleus, the Fourier image of which equals the absolute value of the wavevector $(\hat{k}\,e^{ikr}) = |\mathbf{k}|e^{ikr}$.

1063-7850/00/2605-0389$20.00 

Let us pass to the envelopes by substituting

$$\eta(\mathbf{r}, t) = \frac{2(\varepsilon + 1)}{3k_0(\varepsilon - 1)}\sum_{j=1}^{3} A_j(x_j, y_j, t)\exp(i\mathbf{k}_j\mathbf{r}) + (\text{c.c.}),$$

$$\psi(\mathbf{r}, t) = \frac{2(\varepsilon + 1)}{3k_0^2(\varepsilon - 1)}\sum_{j=1}^{3} \frac{\partial A_j(x_j, y_j, t)}{\partial t}\exp(i\mathbf{k}_j\mathbf{r}) + (\text{c.c.}),$$

where the wavevectors $\mathbf{k}_j$ ($|\mathbf{k}_j| = k_0$) are rotated relative to one another by the angle $2\pi/3$ and the variables $x_j$ and $y_j$ correspond to orthogonal coordinate systems with the abscissa axes parallel to the wavevectors $\mathbf{k}_j$. This representation of the functions $\eta$ and $\psi$ corresponds to hexagonal structure of perturbations on the surface. Substituting these expressions for $\eta$ and $\psi$ into equation (1) and accomplishing averaging and scaling according to

$$\mathbf{r} \longrightarrow \frac{\mathbf{r}}{\sqrt{2}k_0}, \quad t \longrightarrow \frac{t}{\sqrt{2gk_0}}, \quad H \longrightarrow \frac{8g(\varepsilon + 1)^2}{9k_0^2(\varepsilon - 1)^2}H,$$

we obtain the following expression for the averaged Hamiltonian:

$$H = \int\Bigg[\sum_{j=1}^{3}(|A_j|_t^2 + |\hat{L}_jA_j|^2 - \delta|A_j|^2) - A_1A_2A_3 - A_1^*A_2^*A_3^*\Bigg]d^2r, \tag{2}$$

where $\hat{L}_j = \frac{\partial}{\partial x_j} - \frac{i}{2}\frac{\partial^2}{\partial y_j^2}$ are differential operators. Equations for the complex amplitudes $A_j$ ($j = 1, 2, 3$) corresponding to this Hamiltonian are as follows:

$$\frac{\partial^2 A_j}{\partial t^2} = \delta A_j + \hat{L}_j^2 A_j + \frac{A_1^*A_2^*A_3^*}{A_j^*}. \tag{3}$$

These equations describe nonlinear interaction of three standing waves. Let us establish conditions sufficient for the infinite growth of amplitudes $A_j$ during a finite time, in other words, for the collapse. To this end, consider a nonnegative quantity

$$X = \sum_{j=1}^{3} X_j, \quad X_j(t) = \int|A_j|^2 d^2r.$$

Using equations (3) and Hamiltonian (2), we obtain a relationship

$$X_{tt} + 3H = -\delta X + \sum_{j=1}^{3}\int[5|A_j|_t^2 + |\hat{L}_jA_j|^2]d^2r. \tag{4}$$

Sequentially using the integral inequality of Bouniakowsky and the algebraic Cauchy's inequality, we arrive at

$$\sum_{j=1}^{3}\int|A_j|_t^2 d^2r \geq \sum_{j=1}^{3} X_{jt}^2/(4X_j) \geq X_t^2/(4X).$$

Taking into account that $\int|\hat{L}_jA_j|^2 d^2r \geq 0$ and using relationship (4), we obtain the following differential inequality:

$$X_{tt} + 3H \geq 5X_t^2/(4X) - \delta X. \tag{5}$$

It should be noted that analogous inequalities arise in deriving sufficient criteria for the collapse within the framework of the nonlinear Klein–Gordon equation [5], various modifications of the Boussineck equation [6], etc. (see [7] and references therein).

Upon introducing the function $Y = X^{-1/4}$, we may write inequality (5) in the form of the second Newton's law:

$$Y_{tt} \leq -\frac{\partial P(Y)}{\partial Y}, \quad P(Y) = -\frac{1}{8}(\delta Y^2 + HY^6), \tag{6}$$

where $Y$ plays the role of a "particle" coordinate and $P$, of the potential energy. Let the "particle" velocity $Y_t$ be negative (in which case $X_t > 0$). Multiplying (6) by $Y_t$, we obtain

$$E_t(t) \geq 0, \quad E(t) = Y_t^2/2 + P(Y),$$

which implies that the "particle" gains energy during motion. Apparently, a sufficient condition for the $Y$ value to turn zero (whereby $X$ goes to infinity) during a finite time is that the "article" would not encounter a potential barrier even for $E_t = 0$, which corresponds to equality in (6). Then, the collapse would take place under the following conditions:

(i) For $\delta < 0$ and $H > 0$, if $Y(t_0) < |\delta|^{1/4}/(3H)^{1/4}$ and $12E(t_0) \leq |\delta|^{3/2}/(3H)^{1/2}$;

(ii) For $\delta < 0$ and $H > 0$, if $12E(t_0) > |\delta|^{3/2}/(3H)^{1/2}$;

(iii) For $\delta < 0$ and $H \leq 0$;

(iv) For $\delta \geq 0$, if $E(t_0) > 0$,

where $t = t_0$ is the initial time instant. The first three conditions refer to the case of subcritical external fields $E > E_c$, whereby the flat dielectric liquid surface is stable to within a linear approximation. In this case, the instability excitation has a rigid character. Note also

that the stage of amplitude growth according to the power law described by equations (3) is followed by the instability stabilization at the expense of high-order nonlinearities.

The authors are grateful to E.A. Kuznetsov for stimulating discussions and to N.B. Volkov and A.M. Iskol'dskiĭ for their interest in this work.

## REFERENCES

1. M. I. Shliomis, Usp. Fiz. Nauk **112**, 427 (1974) [Sov. Phys. Usp. **17**, 153 (1974)].
2. A. Gailitis, J. Fluid Mech. **82**, 401 (1977).
3. E. A. Kuznetsov and M. D. Spektor, Zh. Éksp. Teor. Fiz. **71**, 262 (1976) [Sov. Phys. JETP **44**, 136 (1976)].
4. V. E. Zakharov, Prikl. Mekh. Tekh. Fiz. **2**, 86 (1968).
5. E. A. Kuznetsov and A. M. Lushnikov, Zh. Éksp. Teor. Fiz. **108**, 614 (1995) [JETP **81**, 332 (1995)].
6. S. K. Turitsyn, Phys. Rev. E **47**, R796 (1993).
7. P. M. Lushnikov, Pis'ma Zh. Éksp. Teor. Fiz. **62**, 447 (1995) [JETP Lett. **62**, 461 (1995)].

*Translated by P. Pozdeev*

*Technical Physics Letters, Vol. 26, No. 5, 2000, pp. 392–393. Translated from Pis'ma v Zhurnal Tekhnicheskoĭ Fiziki, Vol. 26, No. 9, 2000, pp. 70–74.*


# Magnetic Aharonov–Bohm Effect under Time-Dependent Vector Potential

**A. N. Ageev, S. Yu. Davydov, and A. G. Chirkov**

*Ioffe Physicotechnical Institute, Russian Academy of Sciences, St. Petersburg, 194021 Russia*

Received October 11, 1999

**Abstract**—A probability distribution for the scintillations caused by electrons hitting a screen after diffraction on a wire is calculated for the case when time-dependent vector potential is applied in the path of electron travel. Negative experimental results are explained and proper conditions for future experiments are proposed using the expression obtained. *© 2000 MAIK "Nauka/Interperiodica".*

Since the first publications on the magnetic and electrical Aharonov–Bohm (AB) effects [1–3], considerable theoretical and experimental effort was spent to elucidate their nature [4, 5]. Although the original treatment of these effects, based on the analysis of special electromagnetic potentials, encountered certain objections [6], all experimental results obtained by now can be explained using this theoretical model, and we adhere to it in the present work too.

Basic experimental studies aimed at proving the existence of the Aharonov–Bohm effect and at establishing its nature mainly dealt with the magnetic AB effect and were performed using electron optics; it is this case that we analyze below. In the course of those studies, main experimental effort was devoted to minimizing the scattered magnetic fields, which appear upon creating the magnetic flux inside the electronic loop in the path of electron travel. The highest ratio of the magnetic fields inside the loop and in the path of the electron propagation was obtained by Tonomura with coworkers in the middle of 1980s. With these experiments, the possibilities to investigate the nature of the AB effect in the stationary regime were apparently exhausted.

Since the beginning of the 1990s, the studies with the nonstationary fields, including the fields in the optical frequency range, have drawn the attention of researchers [7]. In the following, we restrict our study to the harmonic component of time-dependent potentials, and do not consider the static component, whose influence is well known within the framework of the model adopted.

Specifying the model, we follow the results obtained in [7]. Assume that noninteracting electrons are emitted sequentially from a point source and diffracted on a metallic wire occurring under small positive potential (several volts). Electron scintillations can be observed on a screen placed behind the wire and, after some time have elapsed, they form an interference pattern shaped as bands parallel to the wire. According to the wave theory, the interference pattern appears due to superposition of the two partial electron waves that propagate from the source to the screen on the opposite sides of the wire, as though they travel through the two wings of an interferometer. These partial waves pass the regions where alternating electromagnetic field potentials are present, the vector potentials in the two wings at every instant being equal in magnitude and directed from the source to the screen in the one wing and from the screen to the source, in the other. The interference pattern on the screen can be obtained by replacing the real electron source by two imaginary ones. Let us start from the Schrödinger equation

$$i\hbar\frac{\partial\Psi}{\partial t} = -\frac{\hbar^2}{2m}\Delta\Psi + \frac{ie\hbar}{m}\mathbf{A}\nabla\Psi + \frac{ie\hbar}{2m}\operatorname{div}\mathbf{A}\Psi + \frac{e^2}{2m}\mathbf{A}^2\Psi + e\varphi\Psi, \quad (1)$$

where $\mathbf{A}$ and $\varphi$ are the vector and scalar potentials, respectively, and $e$ is the electron charge ($e < 0$). The SI units are used throughout this paper. To simplify the calculation of the wavefunction, we choose the gauge $\varphi = 0$. We realize that in doing so we cannot consider the ideal case, whereby electric field is absent in the region where the electron waves propagate: it follows from the relation $\mathbf{E} = -\frac{\partial\mathbf{A}}{\partial t} - \nabla\varphi$ that, once the vector potential is time-dependent and $\varphi = 0$, the electric field cannot vanish.

Using the results obtained in [7] we find that, under these assumptions, the wavefunction can be expressed as

$$\Psi(\mathbf{r}, t) \cong \Psi_0\left\{\exp\left(\frac{ie v_{\mathrm{ph}}}{\hbar}\int_0^t(-A)dt\right) + \exp\left(\frac{ie v_{\mathrm{ph}}}{\hbar}\int_0^t A dt\right)\right\}, \quad (2)$$

1063-7850/00/2605-0392$20.00 

where $\Psi_0$ is the wavefunction in the vicinity of the electron source at $t = 0$, $v_{ph}$ is the phase velocity of the electron wave, and $\mathbf{A} = A_0 \cos \omega t$ is the vector potential projection on the direction of the classical electron motion.

With this equation, one can calculate the phases of the partial de Broglie waves from two imaginary electron sources and the intensity of the interference fringes on the screen, which is given by

$$I = \frac{1}{4}\left|\exp\left[\frac{ie v_{ph}}{\hbar}\int_0^t A dt + i\omega_e t\right] + \exp\left[\frac{ie v_{ph}}{\hbar}\int_{-\tau}^t (-A) dt + i\omega_e (t+\tau)\right]\right|^2, \quad (3)$$

where $\omega_e$ is the electron wave angular frequency and $\tau$ is the time delay between the arrival at a given point on the screen of the two electrons emitted simultaneously from the two imaginary sources: $\tau \cong xd/Lv_{ph}$, where $L$ is the distance from the source to the screen, $x$ is the coordinate of a point on the screen (the coordinate axis being oriented perpendicular to the interference fringes), and $d$ is the distance between the imaginary electron sources. Equation (3) represents only the effect of the vector potential, while the direct action of electric component of the electromagnetic field is not accounted for: its influence on the interference pattern is negligible. The time-averaged value of $I$ is given by

$$\bar{I} = \lim_{T\to\infty}\frac{1}{T}\int_0^T I dt = \frac{1}{2}\left\{1 + J_0\left[\frac{2e v_{ph} A_0}{\hbar\omega}\right]\cos\left(\omega_e - \frac{e v_{ph} A_0}{\hbar}\frac{\sin\omega\tau}{\omega\tau}\right)\tau\right\}, \quad (4)$$

where $J_0$ is the zeroth-order Bessel function. For $A_0 = 0$ we obtain

$$I(0) = \frac{1}{2}\{1 + \cos(\omega_e \theta d / v_{ph})\}, \quad (5)$$

where $\theta \cong x/L$ is the diffraction angle. Thus, in the absence of the vector potential we observe equal-amplitude bands on the screen. One can see from (4) that the spatial frequency of the bands increases when the potential is applied. This means that the interference peaks would exhibit narrowing, rather than widening predicted in [6]; this widening, however, is insignificant under the real experimental conditions.

Now, we will analyze expression (4) in the presence of the vector potential, using two sets of the relevant physical parameters, namely (1) that considered in [7] and (2) that corresponding to the experiment reported in [8].

(1) Electron acceleration voltage $U = 10$ kV, $v_{ph} = \frac{1}{2} v_{gr} = 3\times10^7$ m/s, $\omega_e = 1.6\times10^{19}$ rad/s, $d = 5\times10^{-6}$ m, $\tau \cong \theta d/v_{ph} = 1.7\times10^{-13}\theta$ s, $\omega = 10^{15}$ rad/s, and $A_0 = 1.7\times10^{-9}$ (V s)/m. Substituting these values into (5) and (4), we obtain

$$\overline{I(0)} = \frac{1}{2}\{1 + \cos(3\times10^6)\theta\}, \quad (5^*)$$

$$\bar{I} = \frac{1}{2}\{1 + J_0[0, 16]\cos[3\times10^6 + 14]\theta\}. \quad (4^*)$$

Comparing (5*) and (4*), one can see that the difference is too small and, in any case, do not correspond to that predicted in [7].

(2) $U = 100$ kV, $v_{ph} \cong 10^8$ m/s, $\omega_e = 1.6\times10^{20}$ rad/s, $d = 10^{-5}$ m, $\tau \cong 10^{-13}\theta$ s, $\omega = 3\times10^{15}$ rad/s, and $A_0 = \omega^{-1}\sqrt{P\mu_0 c/S}$, where $P$ is the power of the laser radiation focused in a spot of area $S$ in the electron loop plane and $\mu_0$ is the magnetic permeability of vacuum. The optical power achieved in [8] corresponds to $A_0 \cong 2\times10^{-10}$ (V s)/m; substituting this value into (4) we obtain: $\bar{I} = \frac{1}{2}\{1 + J_0[0, 02]\cos(1.6\times10^7 + 3)\theta\}$, i.e., in this case the changes are also too small.

In order to find a situation where the effect of the vector potential is significant, let us consider an extreme case, when this effect is so large that the interference pattern totally disappears. This means that $J_0 = 0$, which occurs when $2e v_{ph} A_0/\hbar\omega \cong 2.4$. This can be achieved, for example, with the following parameters: $U = 100$ kV, $\omega = 2\times10^{14}$ rad/s ($\lambda = 10$ μm), $S = 10^{-10}$ m$^2$, and $P = 24$ mW.

Thus, the obtained expression for the averaged intensity of the interference bands, given by (4), enables us, within the framework of the model adopted in this paper, to explain the experimental result reported in [8] and to predict the possibility of observation of the AB effect due to variable magnetic fields.

## REFERENCES


1. W. Franz, Verh. Deutsch. Phys. Ges. **20**, 65 (1939).
2. W. Ehrenberg and R. Sidey, Proc. Phys. Soc. London, Sect. B **62**, 8 (1949).
3. Y. Aharonov and D. Bohm, Phys. Rev. **115**, 485 (1959).
4. S. Olariu and I. Popescu, Rev. Mod. Phys. **57**, 339 (1985).
5. M. Peshkin and A. Tonomura, Lect. Notes Phys. **340**, 115 (1989).
6. B. S. DeWitt, Phys. Rev. **125**, 2189 (1962).
7. B. Lee, E. Yin, T. K. Gustafson, and R. Chiao, Phys. Rev. A **45**, 4319 (1992).
8. Yu. V. Chentsov, Yu. M. Voronin, I. P. Demenchonok, and A. N. Ageev, Opt. Zh. **8**, 55 (1996).


*Translated by M. Skorikov*

*Technical Physics Letters, Vol. 26, No. 5, 2000, pp. 394–396. Translated from Pis'ma v Zhurnal Tekhnicheskoĭ Fiziki, Vol. 26, No. 9, 2000, pp. 75–80.*


# Stable Electron Emission from Multipoint Liquid-Metal Cathode

**O. P. Korovin, E. O. Popov, S. S. Karatetskiĭ, and V. N. Shrednik**

*Ioffe Physicotechnical Institute, Russian Academy of Sciences, St. Petersburg, 194021 Russia*

Received December 30, 1999

**Abstract**—Low-frequency fluctuations of emission current from multipoint liquid-metal emitter power supplied in various regimes were studied. Images of the emitter surface before and after work were obtained. A change of the supply voltage amplitude for the transition from field emission to explosive emission regime were estimated. © *2000 MAIK "Nauka/Interperiodica".*

In the previous work [1], it was demonstrated that a multipoint liquid-metal emitter in the form of a perforated Lavsan (Dacron) film lying on the surface of liquid gallium may serve an effective source of electrons. Taking into account good prospects of using these emitters for the creation of large-area displays and other devices, it is necessary to study the working parameters of liquid-metal emitters such as noise, etc.

A multipoint liquid-metal emitter should be considered as an ensemble comprising a large number of isolated emitters. During the emission event, each individual emitter has the form of a liquid–metal point, the shape and size of the point are determined by the dynamic equilibrium between the electric field force ad the surface tension of the liquid metal. In contrast to a solid point cathode, a change in the applied voltage modifies both the value of current from the point and its radius, which additionally affects the emission current. Therefore, we may expect that the process of electron emission from a multipoint liquid–metal emitter would exhibit a higher instability was compared to the case of solid point emitter.

In order to check for this hypothesis, we have recorded the emission current with the aid of an LKD-4 recorder. Figure 1 shows the time variation of the emission current measured in various regimes of power supply to the emitter. Different regimes of power supply result, for an equal average emission current, in the different current loads and, hence, may lead to different heating of emitters. In the case of liquid-metal emitters, different power supply modes lead to additional differences in the conditions of liquid–metal point growth. Figure 1 shows the plot of current measured with a Faraday cup in the regimes of sinusoidal voltage (50 or 440 Hz) or dc voltage. The current collected at the Faraday amounted to ~10%. The average emitter current was always about 40 μA.

As seen from Fig. 1, the character of current fluctuations depends on the regime of power supply. Maximum fluctuations are observed for the dc voltage. Note that, in addition to rapid fluctuations, the system features comparatively slow deviations from the average level (lasting 5–10 s), which are probably related to the current redistribution between collector and Faraday cup, caused by variation of the emission capacity of various emitter areas (this effect is most pronounced for the dc voltage supply). Direct observations showed that both sinusoidal and dc power supply is accompanied by weak luminescence of the emitter, which is more stable in the case of alternating voltage.

The short-time current instabilities were studied by the method of analog-to-digital conversion at a discret-

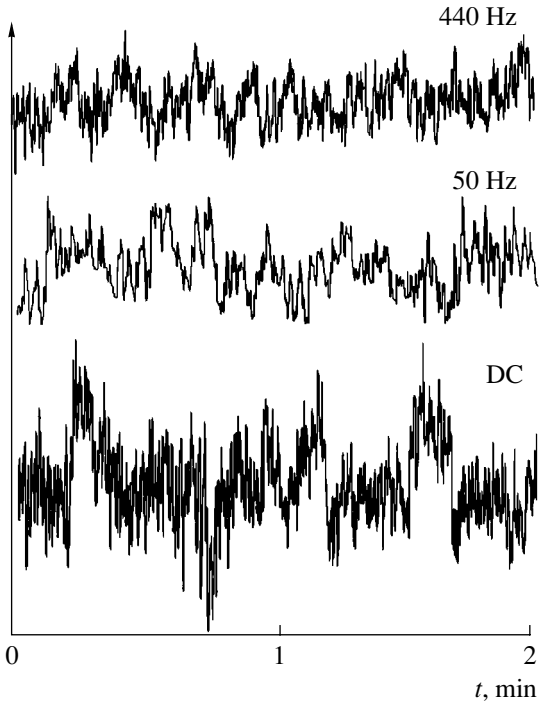


**Fig 1.** Time variation of the emission current from the multipoint liquid-metal emitter power supplied in various modes.

1063-7850/00/2605-0394$20.00 © 2000 MAIK "Nauka/Interperiodica"

ization frequency of 200 kHz and 40 MHz, with the emitter power supply of the same types as above. An analysis of data obtained at 40 MHz showed no fluctuations. Fourier analysis of the data recorded at 200 kHz revealed the presence of a continuous spectrum of the flicker noise, which began at a zero frequency and terminated by a characteristic decay by the law $1/f^{\gamma}$, where $f$ is the noise frequency and $\gamma = 0.85$.

In contrast to the case of dc voltage supply, the oscilloscopic patterns recorded with the dc supply reveal no sharp outbursts, so that the emission current can be interpreted as due to the field emission, without explosive features. However, it is not excluded that a smooth character of the observed current oscillograms can result from addition of large number of microexplosions from various points not resolved in time by the measuring instrumentation. This possibility requires additional investigation. Note that the pattern observed for the dc supply is somewhat analogous to the time variation of current observed for a multipoint liquid–metal emitter and carbon nanotubes in [2].

The assumption that operation of a multipoint liquid-metal emitter involves simultaneous emission from a large number of gallium points is confirmed by micrographs obtained with a scanning electron microscope (SEM) (see Figs. 2a and 2b). Figure 2a shows a region of the emitter surface before operation. The Lavsan membrane is lying on a liquid gallium layer, clearly demonstrating 0.4-μm-diam pores not filled by gallium. Figure 2b shows a micrograph of the emitter surface upon long-term operation. The electric field has pulled gallium out of the pores in a 10-μm-thick membrane and formed a spherical surface on the end of each point. We may suggest that, when the emitter is placed into electric field, the spherical formations will give rise to emitting points, with the shape and size determined, as noted above, by equilibrium between the forces of electric field and surface tension of liquid gallium. Note that, in the case of sinusoidal supply voltage, the emitting tips appear and disappear at a frequency of 50 and 440 cps, which implies that the liquid metal surface is "breathing." This may result in additional cleaning of the emitter surface from contaminations (quite possible under comparatively low vacuum of $6 \times 10^{-3}$–$1.3 \times 10^{-4}$ Pa). As seen from Fig. 2b, this emitter has a more uniform structure as compared to the system of carbon nanotubes. Note that liquid points, in contrast to the nanotubes, are capable of self-restoration upon accidental breakdowns and explosive emissions. The experience of emitter operation with sinusoidal supply showed that the conditions of nonexplosive emission are more readily selected in this mode, which is explained by that the explosive regime cannot establish during a halfperiod of the voltage oscillations.

Using the sinusoidal power supply, we may also provide conditions for the controlled passage from field emission to explosive emission. Figure 3 shows (out of scale) time variation of the emission current for a sinu-

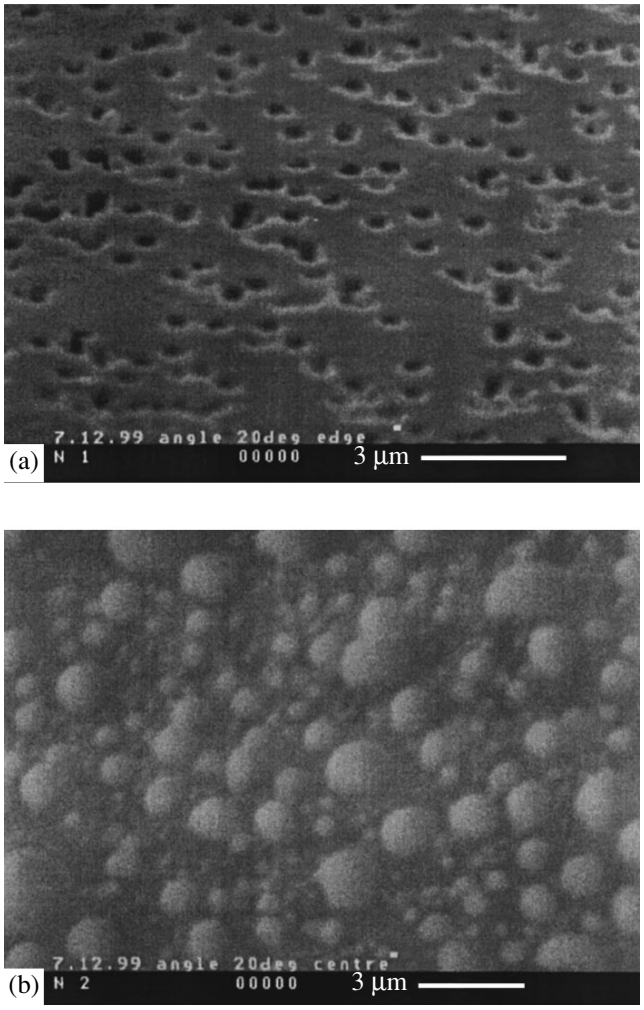


**Fig. 2.** SEM micrographs of a track membrane over gallium layer (a) before operation under voltage and (b) after prolonged operation in a multipoint liquid-metal emitter.

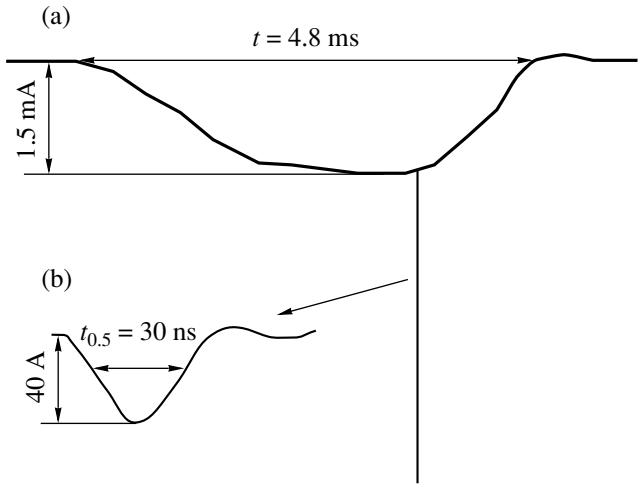


**Fig. 3.** Diagrams showing the current pulse shape (out of scale) in the regime of (a) combined and (b) explosive emission).

soidal power supply at a frequency of 50 Hz. Here, the explosive pulse of current appears on the field-emission pedestal when the sinusoidal voltage amplitude exceed certain level. The further increase in the amplitude leads to the appearance of the second pulse spaced by several tens of microseconds from the first one.

With continued increase in the voltage amplitude, the two pulses observed on the oscilloscope screen approached one another to a minimum distance of ~25 μm. After that, the third explosive emission pulse appeared and began to approach the first two, and so on. Both duration and amplitude of the explosive emission pulses may vary depending on the capacitance of the cathode system, reaching in our case 40 ns (at half height) and 40 A, respectively. Note that the interval of voltage variation featuring the passage from one regime to another is ~0.02%.

In the course of investigation of the process of combined emission, we have observed a phenomenon that should be paid attention from the standpoint of both thermal electron and ion emission. The effect consists in the transfer of substance from emitter to collector: a few explosions is enough for an ensemble of liquid droplets (20–400 Å in diameter) to form on the collector surface [3]. Provided that the supply voltage has the corresponding polarity, this ensemble may also serve a multipoint liquid-metal emitter, with the characteristics comparable with those of the system with perforated Lavsan film.

Thus, the results of our investigations showed that a gallium-based multipoint liquid-metal emitter, in addition to other well-known advantages, provides large pulsed emission currents with the noise characteristics and stability better than those of the existing solid-state emitters.

The work was supported by the Russian foundation for Basic Research, project no. 98-02-18414.

## REFERENCES

1. O. P. Korovin, S. S. Karatetskiĭ, E. O. Popov, and V. N. Shrednik, Pis'ma Zh. Tekh. Fiz. **25**, 39 (1999) [Tech. Phys. Lett. **25**, 310 (1999)].
2. Jean-Marc Bonard, Ultramicroscopy **73** (1–4), 7 (1998).
3. I. S. Gasanov, Prikl. Fiz. **3**, 108 (1999).

*Translated by P. Pozdeev*

*Technical Physics Letters, Vol. 26, No. 5, 2000, pp. 397–399. Translated from Pis'ma v Zhurnal Tekhnicheskoĭ Fiziki, Vol. 26, No. 9, 2000, pp. 81–86.*


# Structural Features and Energy of Small Water Clusters

**S. V. Drozdov and A. A. Vostrikov**

*Institute of Thermal Physics, Siberian Division, Russian Academy of Sciences, Novosibirsk, 630090 Russia*

Received December 8, 1999

**Abstract**—The structures and energies of small water clusters $(H_2O)_n$ with $n \le 10$ were calculated based on the results of computer simulation using molecular dynamics method and a polarization model with nonadditive potential. Structures with minimum energies are characterized by the cluster energy as function of the temperature and by the heat capacity, binding energy, and molecular evaporation energy for various $n$. The most stable structure is that of a ring-shaped $(H_2O)_5$ cluster with only one proton of each water molecule involved into the hydrogen bond formation. © *2000 MAIK "Nauka/Interperiodica".*

The methods of numerical experiment, which are widely used in the physics of clusters [1], offer a possibility of studying the kinetics of intracluster processes on a time scale of the order of a period of intramolecular oscillations, thus providing important supplementary information to the data obtained by conventional laboratory techniques such as the molecular-beam experiments [2]. Water clusters offer an object of special interest for these investigations, since water plays very important role in various phenomena occurring in nature. For example, it was recently reported [3, 4] that collisions of the water clusters and molecules with solid surfaces are accompanied by the phenomenon of charge generation and redistribution. Water clusters actively participate in the ion-molecular processes in the atmosphere and in various plasmachemical processes.

Among the models most frequently employed for the calculation of water molecules, we can distinguish two groups involving "rigid" [5] and "elastic" [6, 7] molecules. The "rigid" models do not allow the intracluster dissociation of $H_2O$ molecules upon the cluster excitation to be studied. Since the final purpose of our molecular dynamics (MD) calculations consists in the investigation of the kinetics of polar $H_2O$ dissociation in water clusters involved in cluster–cluster, cluster–surface, and cluster–ion collisions, we have employed a polarization model of Stillinger and Davis [7] with the force calculation method developed in [8].

According to the model adopted, the $H_2O$ molecules are composed of $H^+$ and $O^{2-}$ ions, the $O^{2-}$ ions possessing polarization. The resulting $H_2O$ molecules have a regular geometry ($r_{OH}$ = 0.9584 Å, $\theta_{HOH}$ = 104.45°), possess a dipole moment of 1.855 D, and are capable of forming clusters at the expense of hydrogen bonds formed between molecules. The total potential of interaction between atoms comprises a sum of special pairwise interatomic potentials and a nonadditive polarization potential. It is important to note that the polarization model employed poses restrictions neither on the atomic oscillations in $H_2O$ molecules nor on their ability to dissociate into ions, leading to a correct value of the polar dissociation energy of $H_2O$ into $H^+$ and $OH^-$ (16.9 eV). Unfortunately, complicated shape and nonadditivity of the interaction potentials markedly increase the computation time, thus limiting the size of calculated clusters. For this reason, the polarization model described above was used only in a few works (see, e.g., [9, 10]). In particular, the structure of $(H_2O)_8$ clusters was calculated in [9] and collisions between $H_5O_2^+$ and $H_3O_2^-$ ions was simulated in [10].

In this work, all calculations were performed by the classical MD method. The Newton equations of motion for a system of particles were solved by the fourth-order Runge–Kutta method at an integration step of 0.1 fs, without potential truncation and limitation of the evaporation of molecules from clusters.

Water clusters with various structures (geometries), corresponding to different local energy minima $U$, were obtained by the following procedure: randomly oriented $H_2O$ molecules were arranged in a parallelepiped and then the atomic velocities were sequentially decreased so as to reduce the cluster temperature to virtually zero (0 K).

Figure 1 shows the structures of clusters corresponding to local energy minima (the corresponding $U$ vales are listed in the table). The clusters with $n \ge 6$ are illustrated by the structures corresponding to lowest $U$ values. Note that the structures with $n$ = 2, 4, and 5 with minimum $U$ coincide with those obtained by other researchers [11, 12]. Wales and Hodges employed a "rigid" model according to Jorgensen [5], while Belford and Campbell [12] used a model with potentials from [13]. For $n$ = 3, the minimum $U$ value in [11, 12] corresponded to structure 4, while our calculations led to structure 1. However, our $U$ value for structure 1 only slightly differs from that reported for structure 4 in [11]. As for the clusters of other dimensions, our $U$ vales are generally lower as compared to those indi-

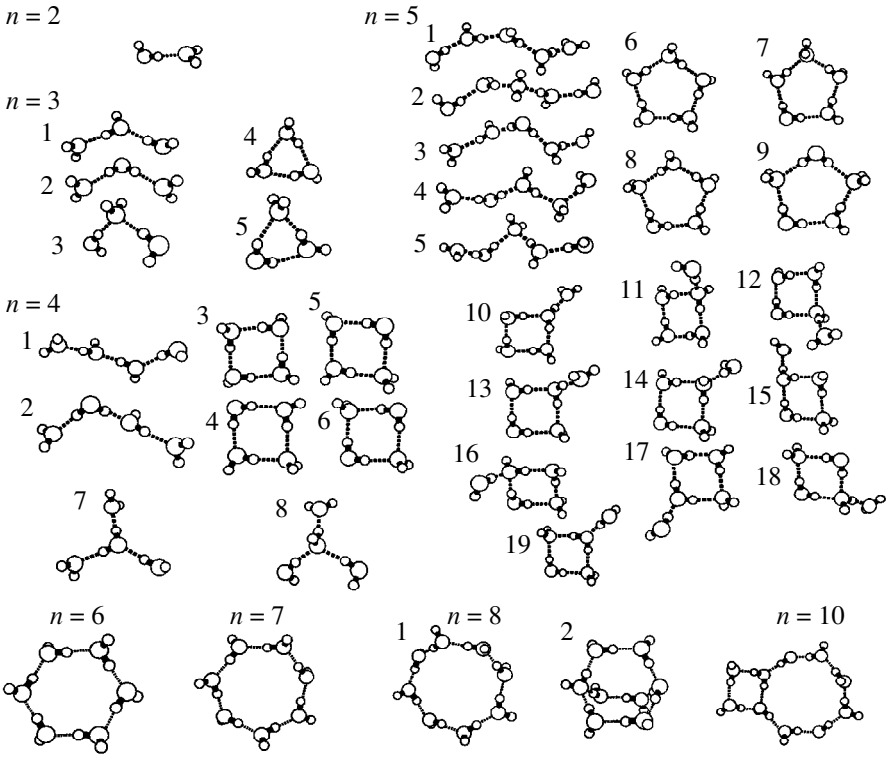


**Fig. 1.** Structures of water clusters corresponding to local potential energy minima.

cated for the global minima in [11]. Our value for $n = 6$ coincides with that in [12], but both differ from the value obtained in [11]. For $n > 6$, our structures do not coincide with those presented in [11]. In particular, our structure 1 for $n = 8$ has the energy lower than structure 2 (corresponding to the global minimum

Local potential energy minima of water clusters with the structures depicted in Fig. 1

| Structure size and number | $U \times 10$, eV | Structure size and number | $U \times 10$, eV | Structure size and number | $U \times 10$, eV |
|---|---|---|---|---|---|
| $n = 2$ | | 7 | –9.616 | 15 | –10.99 |
| | –3.022 | 8 | –9.344 | 16 | –11.7 |
| | –2.705 [11] | $n = 5$ | | 17 | –13.05 |
| $n = 3$ | | 1 | –15.35 | 18 | –11.97 |
| 1 | –6.907 | 2 | –11.92 | 19 | –12.02 |
| 2 | –4.907 | 3 | –11.97 | $n = 6$ | |
| 3 | –4.54 | 4 | –10.03 | | –26.53 |
| 4 | –4.573 | 5 | –10.76 | | –20.51 [11] |
| | –7.257 [11] | 6 | –20.26 | $n = 7$ | |
| 5 | –2.89 | | –15.77 [11] | | –31.09 |
| $n = 4$ | | 7 | –11.72 | | –25.25 [11] |
| 1 | –11.075 | 8 | –14.08 | $n = 8$ | |
| 2 | –8.496 | 9 | –10.42 | 1 | –35.47 |
| 3 | –13.29 | 10 | –16.14 | 2 | –34.15 |
| | –12.09 [11] | 11 | –15.44 | | –31.68 [11] |
| 4 | –8.405 | 12 | –13.11 | $n = 10$ | |
| 5 | –6.721 | 13 | –11.84 | | –43.34 |
| 6 | –7.604 | 14 | –11.002 | | –40.54 [11] |

of $U$ [9]). The discrepancies between our data and those reported in [11, 12] can be explained by differences of the models used to describe the $H_2O$ molecules.

We have calculated the values of energies $U(T)$ in the range from 0 K to the temperature of evaporation, proceeding from the structures with minimum $U$ values at $T = 0$ K. It was found that $U(T)$ plots are well approximated by straight lines. A similar temperature dependence of $U$ was obtained for $n = 5$ in [14] based on a model taken from [6]. The maximum temperatures corresponding to detachment of the $H_2O$ molecules from clusters were as follows: 385 K ($n = 2$), 417 K ($n = 3$), 420 K ($n = 4$), and 280 K (for $n = 10$). It should be noted that the clusters with $n = 4$ and 10 exhibited a change in their structures at certain values of the temperature, while the $U(T)$ function remained linear. The $(H_2O)_4$ cluster acquired a linear structure 1 at $T = 170$ K and turned back to a rig structure 3 when the temperature decreased. The structure of $(H_2O)_{10}$ depicted in Fig. 1 transformed at $T > 70$ K into a ring containing nine water molecules, with one $H_2O$ molecule "squeezed" outside the ring. Visual observation of the evaporation event showed that the first molecule to leave the cluster is that in which no one proton is involved into hydrogen bonds with other molecules.

Linearity of the $U(T)$ function implies that the heat capacity of clusters $C = n^{-1}(dU/dT)$ is independent of the temperature. Figure 2 (curve *1*) shows the plot of $C$ versus $n$. For $n = 10$, $C = 7.6 \times 10^{-4}$ eV/K, which is close to the heat capacity of water at 298 K ($7.8 \times 10^{-4}$ eV/K).

Also depicted in Fig. 2 are the specific binding energy of molecules in the cluster $\epsilon(n) = -U(n)/n$ (curve *2*) and the specific energy of molecule evaporation from the cluster $h(n) = d(nU(n))/dn$ (curve *3*), which were calculated for the structures with minimum $U$ values in the table. The plot of $h(n)$ exhibits a maximum at $n = 5$, which indicates that a five-member cluster with the ring structure 6 is characterized by increased stability with respect to detachment of a water molecule. The plot of $\epsilon(n)$ exhibits saturation for $n \geq 6$, attaining a level of $\epsilon \approx 0.43$ eV/mol. The latter value is close to the binding energy of $H_2O$ molecules in the solid state (~0.5 eV). This behavior of the binding energy qualitatively agrees with the results of ballistic measurements in the beams of molecular clusters [15].

Our calculations showed that water molecules, owing to the hydrogen bonds, are capable of forming a large variety of structures with markedly different binding energies and heat capacities. Most stable are the ring-shaped clusters, in which the five-member ring structure 6 is distinguished with only one proton involved in the hydrogen bond formation. A change in the structure of clusters is accompanied by a jumplike variation of the cluster temperature, which may result in a change of the parameters of water vapor under significantly nonideal conditions, for example, near the critical point.

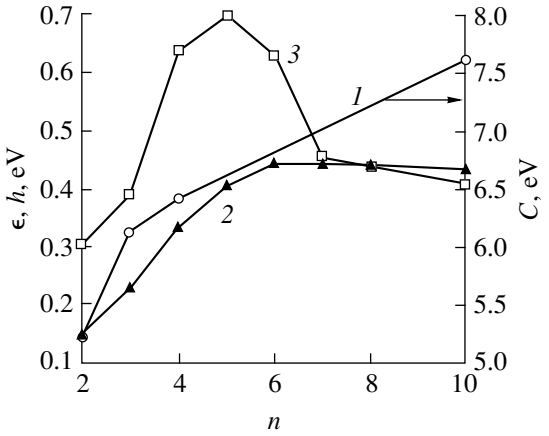


**Fig. 2.** Plots of (*1*) heat capacity $C$, (*2*) binding energy $\epsilon$, and (*3*) specific energy of $H_2O$ molecule evaporation from the cluster $h$ versus cluster size $n$.

The work was supported by the Russian Foundation for Basic Research, projects nos. 98-02-17804 and 98-02-17845.

## REFERENCES

1. A. A. Vostrikov *et al.*, Z. Phys. D **40**, 542 (1997).
2. A. A. Vostrikov, D. Yu. Dubov, and M. R. Predtechenskiy, Chem. Phys. Lett. **139**, 124 (1987).
3. A. M. Zadorozhny, A. A. Vostrikov, *et al.*, Geophys. Res. Lett. **24**, 841 (1997).
4. P. U. Andersson and J. B. C. Pettersson, J. Phys. Chem. B **102**, 7428 (1998).
5. W. L. Jorgensen, J. Chem. Phys. **77**, 4156 (1982).
6. F. H. Stillinger and A. Rahman, J. Chem. Phys. **68**, 666 (1978).
7. F. H. Stillinger and C. W. David, J. Chem. Phys. **69**, 1473 (1978).
8. F. H. Stillinger, J. Chem. Phys. **71**, 1647 (1979).
9. F. H. Stillinger and C. W. David, J. Chem. Phys. **73**, 3384 (1980).
10. T. A. Weber and F. H. Stillinger, J. Chem. Phys. **77**, 4150 (1982).
11. D. J. Wales and M. P. Hodges, Chem. Phys. Lett. **286**, 65 (1998).
12. D. Belford and E. S. Campbell, J. Chem. Phys. **86**, 7013 (1987).
13. E. S. Campbell and M. Mezei, J. Chem. Phys. **67**, 2338 (1977).
14. P. L. Moore Plummer and T. S. Chen, J. Chem. Phys. **86**, 7149 (1987).
15. A. A. Vostrikov, Zh. Tekh. Fiz. **54**, 327 (1984) [Sov. Phys. Tech. Phys. **29**, 191 (1984)].

*Translated by P. Pozdeev*

*Technical Physics Letters, Vol. 26, No. 5, 2000, pp. 400–402. Translated from Pis'ma v Zhurnal Tekhnicheskoĭ Fiziki, Vol. 26, No. 9, 2000, pp. 87–94.*


# The Optical Attenuation of Laser Radiation in Thin Fullerene $C_{70}$–Polyimide Films. Effect of Fullerenes on the Transmission of Azide Films

**N. V. Kamanina, E. L. Aleksandrova, and L. N. Kaporskiĭ**

*Vavilov Optical Institute, State Scientific Center of the Russian Federation, St. Petersburg, 193171 Russia*

Received December 21, 1999

**Abstract**—The phenomenon of optical attenuation of laser radiation in the visible spectral range was studied in a promising photosensitive medium based on fullerene $C_{70}$–polyimide films. The effect of fullerenes on the transmission of laser radiation in azide-based systems is demonstrated. *© 2000 MAIK "Nauka/Interperiodica".*

Macromolecular media based on polyimides (PIs) have been extensively investigated since the first publication [1] on their use as photoconducting materials for the electrophotographic reproduction (Xerox). However, practical application of PIs in optics was limited by poor solubility of these polymers in most organic solvents, unless a new class of aromatic soluble polyimides was created [2, 3] possessing high intrinsic photosensitivity in the blue-violet and near-IR spectral ranges. Polyimides of this class are widely used in the systems of reversible optical data recording [4], phase aberration correctors [5], and other devices of real-time coherent-optical systems [6, 7].

The unique optical and photoelectric properties of water-soluble aromatic PIs are determined by the possibility of excitation of the π-electron systems in these polymers. Directed modification of the macromolecular chain structure and donor–acceptor interactions provides a means of controlling the electron properties of PIs, which increases the prospects for their application.

At present, an important direction in investigation of the optical properties of macromolecular compounds, including polyimides, is related to their possible use as matrices for the introduction of fullerenes with a view to creating effective optical attenuation of laser radiation [8, 9]. Previously, we have established the existence of a bathochromic shift in the absorption spectra of fullerene-containing PIs and studied dependence of the level of optical attenuation on the content of a fullerene mixture (87 wt % $C_{60}$, 13 wt % $C_{70}$) in the composition [10, 11]. We have also determined the absorption cross-section of the charge-transfer complex formed by a triphenylamine (donor) fragment of PI and fullerene (acceptor) and found an absorption peak at $\lambda = 1405$ nm probably related to the intermolecular complex formation in the same fullerene-containing PI [12]. It should be noted that the presence of spectral features in the long-wavelength spectral range markedly expands the field of possible application of the fullerene-containing PIs as nonlinear optical attenuators in the near-IR spectral range. The effect of inverse absorption saturation and, hence, of the laser radiation attenuation in the fullerene–dye–PI system, was recently explained within the framework of the Forster model [13].

The purpose of this work was to study the optical attenuation of laser radiation in thin $C_{70}$–PI films. Below, we present comparative data on the transmission of fullerene-containing azide films and demonstrate the effect of electron affinity of the acceptor fragment on the photosensitivity and the quantum yield of charge carrier production in these films.

**Experimental.** The PI films with a thickness of 1.5–2 μm were prepared using 3- and 6.5-% solutions of a photosensitive polyimide 6B (PI-6B) in 1,1,2,2-tetrachloroethane. The composition was applied by a centrifuging technique onto glass substrates carrying preliminarily deposited conducting layers, which allowed the samples to be used for the photosensitivity and conductivity measurements. Since fullerenes are also well soluble in the solvent selected [14], the composite solutions provide for the obtaining of homogeneous films, in which transmission of a He–Ne laser beam with a 300-μm-diam spot varied within 5% over the whole sample film area with a diameter of 35 mm. The high homogeneity of samples was also confirmed by the results of investigation in a CamScan SU-90FE electron microscope with a resolution of 20 Å [15]. The content of fullerene $C_{70}$ in the films was varied within 0.2–0.5 wt %. In azide-based films, the content of fullerene $C_{60}$ was 0.5 wt %. A nonphotosensitive polyimide of the 81A grade (PI-81A), transparent in the visible range and possessing good film-forming and glass-adhesive properties, was used as the plasticizer component. The azide–plasticizer ratio in all compositions was 5 : 1

1063-7850/00/2605-0400$20.00 © 2000 MAIK "Nauka/Interperiodica"

The experiments were performed using second harmonic radiation of a YAG:Nd laser with a pulse duration of 15 ns. The spot size on the sample was 3–3.5 mm. The incident laser radiation energy was controlled with the aid of calibrated optical filters. The optical attenuation of laser radiation in the fullerene-containing medium was studied using a single-pass scheme analogous to that described in [13]. The photosensitivity was studied using an electrophotographic method described in [16]. The measurements were performed at a photon flux density of $10^{13}$ cm$^{-2}$ s$^{-1}$ in the wavelength range 400–900 nm.

**Results and discussion.** Figure 1 shows the plots of output radiation energy ($E_{out}$) versus the incident energy ($E_{in}$) for four samples. Curve *1* presents transmission of a PI film prepared using a 3% PI solution without fullerene additive. Curves *2* and *3* correspond to the same polymer containing 0.2 and 0.5 wt % of fullerene $C_{70}$, respectively. Finally, curve *4* refers to a sample obtained using a 6.5% PI solution containing 0.5 wt % of $C_{70}$. As seen from these data, all the fullerene-containing systems studied exhibit the optical attenuation manifested by the effect of inverse absorption saturation observed at a given beam power level and in the spectral range indicated.

In the general case, the phenomenon of optical attenuation in fullerene-containing systems is determined by generation of the excited states of fullerene molecules with the absorption cross-section exceeding that of the ground state [17–19]. In our experiment, the laser pulse duration (~15 ns) was longer than the characteristic time of fullerene transition from singlet to triplet state (1.2 ns [19]), which accounted for the effect realization by the $T_n \longrightarrow T_1$ scheme. Calculations [12] showed that the absorption cross-section of the excited intermolecular complex in the fullerene-containing PI (fullerene triphenylamine fragment of PI) is 300 times the value for the intramolecular complex with charge transfer between donor and acceptor fragments of the PI matrix molecule. This circumstance naturally determines particularities of the effect of optical attenuation in fullerene-containing PI structures.

In the system of PI sensitized by fullerene $C_{70}$, studied in this work, the onset of a nonlinear transmission region is observed at 350–400 mJ, in contrast to 150 mJ observed for PI sensitized with a $C_{60} + C_{70}$ mixture [10, 11] (for the same total fullerene content of 0.5 wt %). The attenuation efficiency is also greater in the system containing $C_{70}$ alone. It should be noted that the absorption spectrum of PI containing fullerene $C_{70}$ is shifted by 25–30 nm toward longer wavelengths as compared to the spectrum of a sample containing the $C_{60} + C_{70}$ mixture. This provides for more favorable conditions of an overlap between the absorption spectrum of the $C_{70}$–PI system and the luminescence spectrum of the PI matrix at a laser radiation wavelength (532 nm) and, hence, for a more effective excitation energy transfer in the system studied in this work.

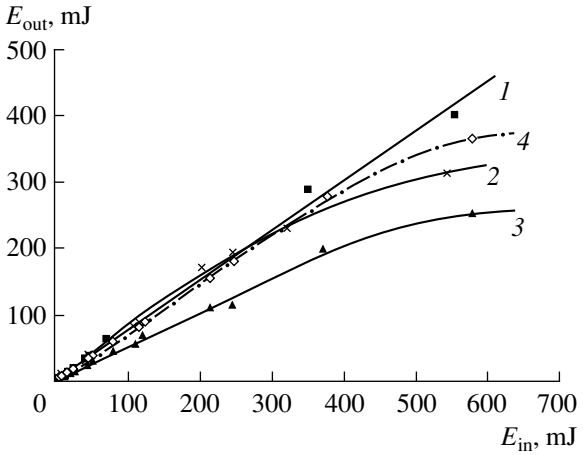


**Fig. 1.** The plots of output radiation energy ($E_{out}$) versus the incident energy ($E_{in}$) for various fullerene–PI systems (see the text for explanations).

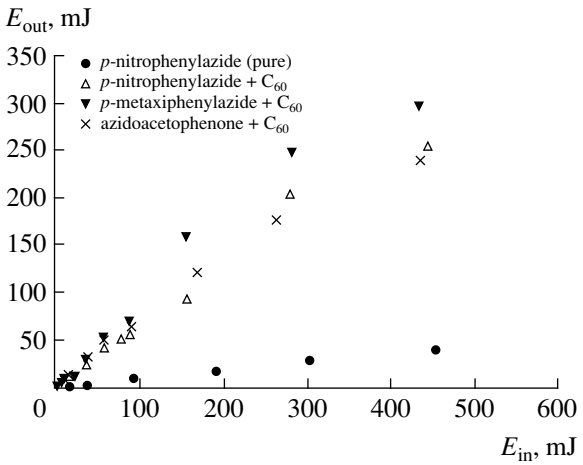


**Fig. 2.** The plots of output radiation energy ($E_{out}$) versus the incident energy ($E_{in}$) for fullerene–PI systems based on various azides.

Another important factor is the low ionization potential of the triphenylamine PI fragment and a change in conformation of this fragment upon the excitation from neutral tetrahedral to ionized planar form. This provides for the possibility of finding a parallel plane arrangement, accounting for a more effective overlap between the electron shells with $C_{70}$ molecule (having elongated shape of the ellipsoid of rotation) than with $C_{60}$ molecule (having virtually spherical shape). The level of optical attenuation of the laser radiation (determined from curve *3* in Fig. 1) was about 4 J/cm$^2$ at a laser radiation energy of $E_{in} \sim 500$ mJ, which indicates that the fullerene-containing PIs can may serve as effective nonlinear optical attenuators of laser radiation at sufficiently high incident laser beam energy density.

Characteristics of fullerene-PI films based on various azides

| Acceptor fragment | $-OCH_3$ | $-NO_2$ | $-\overset{\overset{O}{\|}}{C}-CH_3$ | Fullerene $C_{60}$ |
|---|---|---|---|---|
| Electron affinity, eV | −0.17 | 0.54 | 0.64 | 2.65 |
| Photosensitivity, $cm^2/J$ | $3 \times 10^{-3}$ | $1.2 \times 10^{-3}$ | $\sim 10^{-4}$ | |
| Quantum yield of charge carrier photoproduction | 0.07 | 0.02 | $< 10^{-4}$ | |

Note: The values of electron affinity were taken for the azide fragments from [20] and for the fullerene from [18].

Figure 2 shows the plots of output radiation energy ($E_{out}$) versus the input energy ($E_{in}$) for fullerene-containing azide films with various electron affinities of the intramolecular acceptor fragment of PI. The values of the electron affinity energy of acceptor fragments in the azide compounds studied are given in the table. Note that the azide-based films free of fullerenes transmit the laser radiation on the level of 5%. The introduction of fullerene $C_{60}$ increases the transmission of all samples up to 50–60%. This clarification effect is apparently related to the excitation of both the individual fullerene molecules and the complexes with charge transfer between the donor azide fragment and fullerene (possessing a high acceptor ability with the electron affinity greater than that of acceptor fragments in the azides studied).

As seen from Fig. 2 and the table, the optical transmission, photosensitivity, and quantum yield of charge carrier photoproduction in fullerene-containing azide films increase with decreasing electron affinity of the acceptor fragment of azide matrix molecules. This behavior apparently indicates that fullerenes, as most active electron acceptors, replace the intramolecular acceptor fragments of azides as a result of the intramolecular donor–acceptor interaction.

Thus, we have experimentally studied the phenomenon of optical attenuation of laser radiation in a fullerene $C_{70}$–polyimide composition in comparison with analogous $C_{60}$–PI system. Comparative data on the transmission characteristics of fullerene-containing azide films have been obtained demonstrating that the electron affinity of the acceptor fragment of the matrix azide affects the efficiency of attenuation, the photosensitivity, and the quantum yield of charge carrier photoproduction.

## REFERENCES


1. US Patent No. 3554744, 1971.
2. P. I. Dubenskov, T. S. Zhuravleva, A. V. Vannikov, *et al.*, Vysokomol. Soedin., Ser. A **30**, 1211 (1988).
3. B. M. Rumyantsev, V. I. Berendyaev, N. A. Vasilenko, *et al.*, Vysokomol. Soedin., Ser. A **39**, 720 (1997).
4. V. S. Myl'nikov, *Photoconductivity of Polymers* (Khimiya, Leningrad, 1990).
5. N. V. Kamanina, L. N. Some, and A. A. Tarasov, Opt. Spektrosk. **68**, 691 (1990).
6. N. V. Kamanina and N. A. Vasilenko, Electron. Lett. **31**, 394 (1995).
7. N. V. Kamanina and N. A. Vasilenko, Opt. Quantum Electron. **29**, 1 (1997).
8. A. Kost, L. Tutt, M. B. Klein, *et al.*, Opt. Lett. **18**, 334 (1993).
9. T. F. Boggess, G. R. Allan, S. J. Rychnovsky, *et al.*, Opt. Eng. **32**, 1063 (1993).
10. N. V. Kamanina, L. N. Kaporskiĭ, and B. V. Kotov, Opt. Zh. **65**, 85 (1998).
11. N. V. Kamanina, L. N. Kaporskiĭ, and B. V. Kotov, Opt. Commun. **152** (4–6), 280 (1998).
12. Yu. A. Cherkasov, N. V. Kamanina, E. L. Alexandrova, *et al.*, Proc. SPIE **3471**, 254 (1998).
13. N. V. Kamanina, Opt. Commun. **162**, 228 (1999).
14. V. N. Bezmel'nitsyn, A. V. Eletskiĭ, and M. V. Okun', Usp. Fiz. Nauk **168**, 1195 (1998) [Phys. Usp. **41**, 1091 (1998)].
15. N. V. Kamanina, N. M. Kozhevnikov, S. O. Kognovitsky, and N. A. Vasilenko, *Paper Presented at the Photonics West "Optoelectronics Materials and Devices" Conference, San Jose, California, January 22–28* (San Jose, 2000).
16. I. A. Akimov, Yu. A. Cherkasov, and M. I. Cherkashin, *Activated Photoeffect* (Nauka, Moscow, 1980).
17. L. W. Tutt and A. Kost, Nature **356**, 225 (1992).
18. A. V. Eletskiĭ and B. M. Smirnov, Usp. Fiz. Nauk **165**, 977 (1995) [Phys. Usp. **38**, 935 (1995)].
19. V. P. Belousov, I. M. Belousova, V. P. Budtov, *et al.*, Opt. Zh. **64**, 3 (1997).
20. L. V. Gurvich, G. V. Karachevtsev, V. N. Kondrat'ev, Yu. A. Lebedev, V. A. Medvedev, V. K. Potapov, and Yu. S. Khodeev, *Energies of Chemical Bond Rupture, Ionization Potentials, and Electron Affinity* (Nauka, Moscow, 1974).


*Translated by P. Pozdeev*

*Technical Physics Letters, Vol. 26, No. 5, 2000, pp. 403–405. Translated from Pis'ma v Zhurnal Tekhnicheskoĭ Fiziki, Vol. 26, No. 10, 2000, pp. 1–8.*


# An STM Investigation of the Surface Structure of Graphite Irradiated by Pulses of Fission Fragments

**M. A. Kozodaev, O. N. Makeev, V. F. Khokhryakov, L. A. Osadchuk, B. G. Levakov, A. G. Zaluzhnyĭ, V. P. Babaev, and A. L. Suvorov**

*Institute of Theoretical and Experimental Physics, State Scientific Center of the Russian Federation, Moscow, Russia*
*Institute of Technical Physics, State Nuclear Research Center of the Russian Federation, Snezhinsk, Russia*
*Moscow Institute of Physical Engineering (Technical University), Moscow, Russia*

Received December 30, 1999

**Abstract**—A method for processing structural materials by pulsed bombardment with fission fragments in a fuel solution reactor has been developed. The samples were irradiated with a particle fluence varied from $10^{11}$ to $5 \times 10^{12}$ cm$^{-2}$. The surface structure of a highly oriented pyrolytic graphite upon these treatments was studied by scanning tunneling microscopy (STM). The spectrum of surface defects and the surface roughness of irradiated samples were determined. © *2000 MAIK "Nauka/Interperiodica".*

**1. Introduction.** Investigating the effects of neutron irradiation on the structural materials, related to the development of modern nuclear setups (fast neutron reactors, thermonuclear reactors) requires using new, effective and economic methods for modeling the action of high-fluence neutron fluxes ($10^{22}$–$10^{24}$ cm$^{-2}$). Indeed, direct exposure of the samples in operating reactors until accumulating a necessary fluence is a time-consuming and expensive procedure. At present, these fluences are usually modeled by irradiating the samples with charged particles in various types of accelerators.

In this work, we have developed a relatively simple and cheap method based on the irradiation of structural materials with fission products. While this method has certain disadvantages (predominant irradiation of the surface layers of samples, and some others), it offers an obvious advantage of rapidly gaining a necessary level of displacements per atom (dpa). In addition, study of the effect of irradiation with fission products on the surface state and properties of structural materials is of considerable independent interest.

Below we report on the first results of our investigations of the effect of irradiation with fission products on the surface structure of carbon-based materials. The samples were studied by the method of scanning tunneling microscopy (STM) described in detail in [1–3].

**2.1. Irradiation of samples.** The samples of highly-oriented pyrographite (HOPG) were irradiated in a fuel solution reactor (Institute of Technical Physics, Snezhinsk) [4] equipped with a specially designed source of fission products. Figure 1 shows a schematic diagram of this source. A base element of the system is the neutron to fission products converter (NFPC), where a flux of thermal neutrons bombarding an active target gives rise to fission events ($n$, $f$), with a typical yield of two fission fragments per event having the energies 99.8 and 68.4 MeV, the weights 96.08 and 139.92 amu, and the most probable charges $Z_p$ = 40 and 56 for the light and heavy fragments, respectively. NFPC must ensure a high thermal, mechanical, and radiation stability of operation, especially in the pulsed operation mode. Various NFPC designs were described in [5]. The active target was made of uranium enriched with $^{235}$U to 90%.

During operation of the setup, we have measured fluences of the fission products, the yield of sputtered uranium, and the sample and target temperatures. The

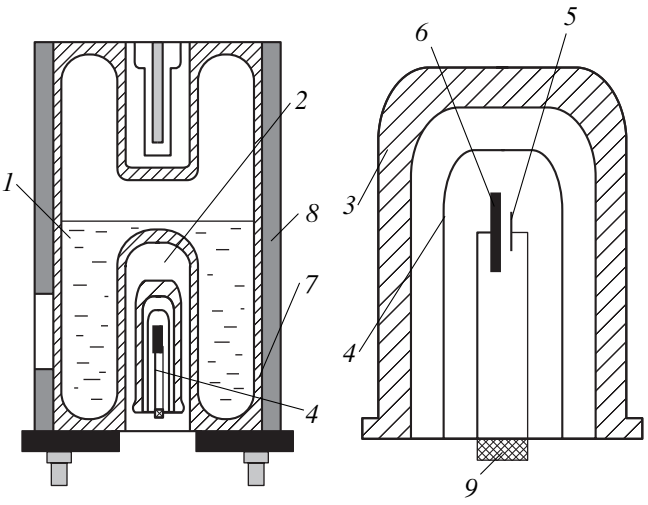


**Fig. 1.** Schematic diagram of the fission fragment source (FFS-1): (*1*) active reactor zone; (*2*) experimental channel; (*3*) fast to slow neutron converter; (*4*) experimental ampule; (*5*) sample; (*6*) neutron to fission product converter (NFPC); (*7*) reactor vessel; (*8*) biological shield; (*9*) electric output connector of monitoring transducers.

1063-7850/00/2605-0403$20.00 © 2000 MAIK "Nauka/Interperiodica"

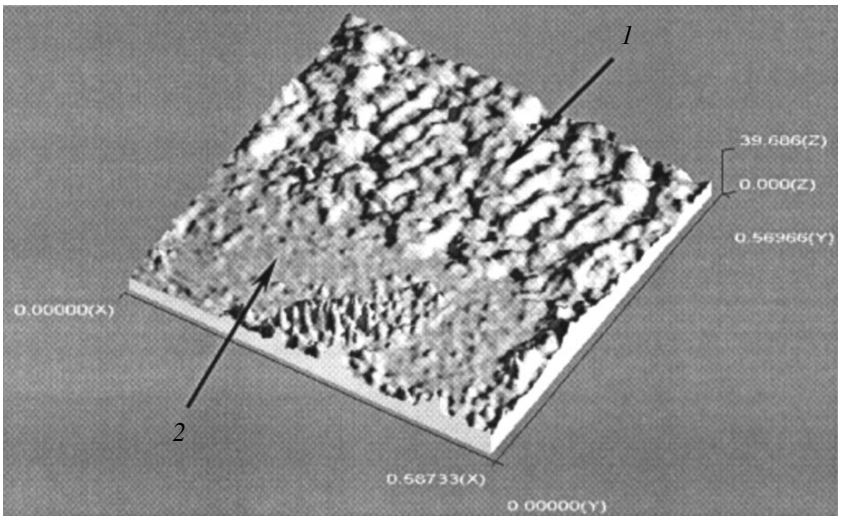


**Fig. 2.** A typical STM image of the HOPG surface upon irradiation with fission fragments; arrows indicate (*1*) a region of significant degradation and (*2*) a region into which no fission fragments did fall (illustration of the irradiation nonuniformity). Scanned area, $0.59 \times 0.57$ μm; roughness height scatter, 40 nm.

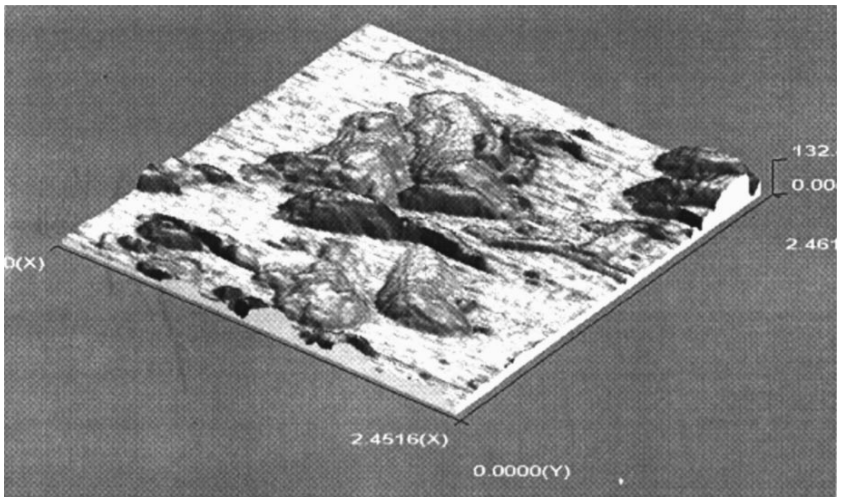


**Fig. 3.** An STM image of the HOPG surface upon irradiation with fission fragments; the formation of separate "hills" is related to the overlap of damaged areas produced by several incident fission fragments. Scanned area, $2.5 \times 2.5$ μm; roughness height scatter, 132 nm.

particle fluences and uranium sputtering yields were measured by Mössbauer spectroscopy with the aid of aluminum foil. The temperatures were measured using a chromel–copel thermocouple.

In a pulsed irradiation mode, with an energy deposition of 57 MJ in the active reactor zone and a pulse duration of 2.4 ms, the fluence of fission fragments on the sample surface reached $\sim 10^{12}$ cm$^{-2}$ at a particle flux intensity of $\sim 4 \times 10^{14}$ cm$^{-2}$ s$^{-1}$. The NFPC surface temperature during irradiation was ≥250°C.

**2.2. STM investigation of the sample surface structure.** The control (unirradiated) and exposed HOPG samples were investigated in air using an original STM setup. The surface of each sample was studied in 25 sites. Note that the sample preparation and handling was markedly complicated by their radioactivity. The average activity was about 850 μR/h at a 1 cm distance from the samples. This circumstance also explained special scanning regimes selected so as to minimize the effect of radiation on the STM scanner point.

**3. Results and discussion.** Analysis of the STM images of the surface of graphite led us to a conclusion that single interactions of the fission fragments with the target surface cannot be observed in the samples irradiated to a fluence of $5 \times 10^{11}$ cm$^{-2}$ and above because of overlap of the damaged areas. This is confirmed by an estimate, according to which these fluences correspond to a surface area of not greater than $\sim 15 \times 15$ nm$^2$ per

Fractal dimensions of the HOPG surface bombarded with various high-energy ions

| Projectile | $D_1$ | $D_2$ |
|---|---|---|
| Unirradiated control | 1.0003 ± 0.0001 | 2.0003 ± 0.0001 |
| 3-MeV protons at normal incidence | 1.0013 ± 0.0001 | 2.0012 ± 0.0001 |
| 90-keV protons incident at 45° | 1.0038 ± 0.0010 | 1.0023 ± 0.0009 |
| 90-keV protons at normal incidence | 1.0265 ± 0.0149 | 2.0176 ± 0.0009 |
| 25-keV cesium ions | 1.0071 ± 0.0019 | 2.0059 ± 0.0017 |
| Laser-excited $SiO_2$ plasma | 1.0079 ± 0.0010 | 2.0072 ± 0.0009 |
| Fission products | 1.0054 ± 0.0012 | 2.0058 ± 0.0014 |

projectile. A fluence of $5 \times 10^{11}$ cm$^{-2}$ results in a comparatively uniform damage of the surface, with some areas containing isolated hills (Figs. 2 and 3).

As mentioned above, several tens of surface images were obtained for each sample. In order to evaluate the surface roughness (i.e., the degree of surface development), each image was characterized by the fractal dimension [6]. Previously we have studied by STM changes in the surface relief of HOPG samples induced by ion bombardment (proton beams of various energies incident at variable angles, high-energy heavy ions, laser-excited plasma) [7, 8]. A possible mechanism explaining the formation of "thermal" tracks in the bulk and a periodic relief on the HOPG surface bombarded with high-energy particles was proposed in [9]. Comparative data on the effect of radiations of various types on the surface relief are summarized in the table in terms of the fractal dimensions calculated for the profile ($D_1$) and along the surface ($D_2$). According to this table, the fractal dimensions may vary widely, even for the same sample. The large scatter can be explained by the fact that the sample surface was scanned in various sites, representing different structural cells (crystallites) with various orientations, and, probably, by nonuniform irradiation. Data presented in the table are illustrated by Fig. 4.

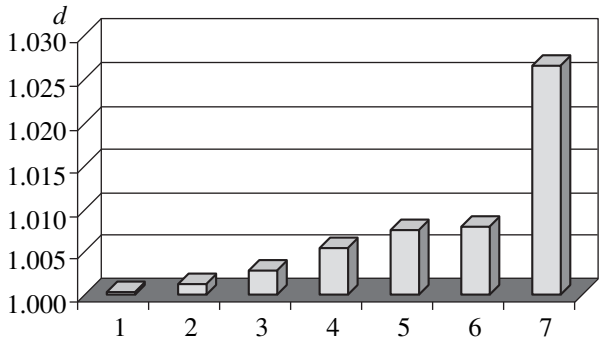


**Fig. 4.** A histogram illustrating development (fractal dimension *d*) of the surface of HOPG samples irradiated by various ions: (1) unirradiated control; (2) 3-MeV protons at normal incidence; (3) 90-keV protons at 45°; (4) fission products; (5) 25-keV cesium ions; (6) laser-excited $SiO_2$ plasma; (7) 90-keV protons at normal incidence.

It should be emphasized that the above data present a rough relative pattern and are insufficient to select the parameters of, e.g., proton irradiation, that are necessary to provide for a developed surface of a particular material. This work offers a methodological approach that has to be further developed. The first task is to reduce the irradiation fluence so as to study by STM the results of single projectile–target surface interactions. Another step, which is already in progress, is to use the method of field-ion microscopy to study the interaction of individual fission fragments with carbon-based materials, refractory metals, and their alloys.

## REFERENCES

1. S. N. Magonov and M.-H. Whangbo, *Surface Analysis with STM and AFM. Experimental and Theoretical Aspects of Image Analysis* (Wiley-VCH, 1995).
2. A. L. Suvorov, *Field-Ion Microscopy of Radiation Defects in Metals* (Énergoizdat, Moscow, 1982).
3. A. L. Suvorov, Yu. N. Cheblukov, N. E. Lazarev, *et al.*, *Study of the Surface and Bulk Defects in Carbon and Silicon by Field-Ion and Scanning Tunneling Microscopies*, Preprint No. 24, ITÉF (Institute of Theoretical and Experimental Physics, Moscow, 1998).
4. V. S. D'yankov, V. P. Korolev, A. I. Kormilittsin, *et al.*, Fiz. Met. Metalloved. **81**, 245 (1996).
5. V. T. Kazaryan, B. A. Litvinenko, L. P. Roginets, and I. A. Savushkin, *Physical Principles of Using the Kinetic Energy of Fission Fragments in Radiation Chemistry* (Nauka i Tekhnika, Minsk, 1972).
6. A. Talibuddin and J. P. Runt, J. Appl. Phys. **76**, 5070 (1994).
7. M. A. Kozodaev, B. A. Loginov, A. L. Suvorov, and A. M. Kozodaev, in *Proceedings of the 1st Moscow International Physics School at the Institute of Theoretical and Experimental Physics* (Inst. Teor. Éksp. Fiz., Moscow, 1998), p. 241.
8. A. L. Suvorov, A. Yu. Didek, Yu. N. Cheblukov, *et al.*, in *Proceedings of the 43rd International Field Emission Symposium* (Moscow, July 14–19, 1999), P-90.
9. D. V. Kulikov, A. L. Suvorov, R. A. Suris, *et al.*, Pis'ma Zh. Tekh. Fiz. **23**, 27 (1997) [Tech. Phys. Lett. **23**, 507 (1997)].

*Translated by P. Pozdeev*

*Technical Physics Letters, Vol. 26, No. 5, 2000, pp. 406–407. Translated from Pis'ma v Zhurnal Tekhnicheskoĭ Fiziki, Vol. 26, No. 10, 2000, pp. 9–12.*


# Output Power Limits for Pulsed Relativistic Microwave Oscillators of Different Types

**A. N. Didenko and M. S. Dmitriev**

*Moscow State Engineering Physics Institute (Technical University), Moscow, 115409 Russia*

Received January 13, 2000

**Abstract**—High-power microwave generation with high-current electron accelerators is studied theoretically. Output power limits are evaluated for most commonly used microwave devices, such as traveling-wave tubes, klystrons, magnetrons, and vircators. © *2000 MAIK "Nauka/Interperiodica".*

This paper addresses the problem of increasing the output power of nanosecond-pulse microwave oscillators. As is known, they are now capable of generating several gigawatts or even tens of gigawatts [1]. We present a comparative study of the output power limits for relativistic microwave oscillators of different types with regard to the parameters of a high-current electron accelerator employed.

As demonstrated in [2], the maximum output power of a microwave oscillator can be expressed as

$$W_{\text{rad}} = 2\pi\alpha(\gamma-1)\frac{S}{\lambda^2}W_A, \qquad (1)$$

where

$$W_A = 8.5 \text{ GW}, \quad \alpha = \frac{\int_S [\mathbf{EH}^*]dS'}{E_0^2 S}.$$

The dimensionless coefficient $\alpha$ depends on the oscillator type, the oscillation modes excited, and the shape and position of the output coupling hole. In the case of a cylindrical resonator where an $E_{011}$ wave is excited, we have

$$W_{\text{rad}} \approx (\gamma-1)W_A, \qquad (2)$$

which is valid for most suitable values of resonator parameters and the fundamental mode.

The above formulas were derived under the assumption that the motion of particles in varying fields of frequency $\omega$ can be described with the potential $U_{\text{rf}} = \frac{eE_0^2}{4m\omega^2}$, where $E_0$ is the amplitude of the induced electric field [3]. However, the conjecture is not universally true.

Let us determine the output power limits for most commonly used pulsed relativistic microwave oscillators without resorting to approximations used to derive the above expressions in [2].

Recall that the power generated in a microwave structure with impedance $Z$ can be evaluated from

$$W = \frac{U_{\text{out}}^2}{Z} = \frac{250(\gamma-1)^2}{Z} \text{ GW}, \qquad (3)$$

where $U_{\text{out}} = \frac{mc^2(\gamma-1)}{e}$ is the external field potential determined by the kinetic energy of the electron beam. Since $U_{\text{out}}$ depends solely on the electron accelerator parameters, formula (3) indicates that raising output power necessitates reducing $Z$. Let us find expressions for $Z$ as applied to a traveling-wave tube, magnetron, klystron, or vircator.

The time-averaged microwave power induced in a cylindrical waveguide is

$$W = \frac{\pi k k_z}{Z_0 \kappa^2}\frac{a^2}{2}[J_1^2(\kappa a) - J_0(\kappa a)J_2(\kappa a)]E_0^2, \qquad (4)$$

where $a$ is the radius of the beam opening in the slow-wave structure [4]. Assume that $E_0 = \frac{U_{\text{out}}}{L}$, where $L$ is the resonator length. For the traveling wave tube and the klystron, (3) and (4) imply

$$Z = \frac{Z_0}{2\pi^2}\left(\frac{L}{a}\right)^2\frac{\lambda^2}{S}\beta_p F(\kappa a), \qquad (5)$$

where $F(\kappa a) = \frac{\kappa^2 a^2}{[J_1^2(\kappa a) - J_0(\kappa a)J_2(\kappa a)]}$, $\beta_p$ is the phase velocity of the wave, and $Z_0 = 377\ \Omega$. The value of $F(\kappa a)$ varies within the range 8–20. The lower bound corresponds to $\beta_p = 1$ (traveling-wave tube); the higher bound, to a smooth waveguide or resonator (klystron).

1063-7850/00/2605-0406$20.00 © 2000 MAIK "Nauka/Interperiodica"

Consider a traveling-wave tube. Its diaphragmatic slow-wave guide has $\beta_p = \beta_e$, which is close to 1 even at a modest $\gamma$. With $\frac{L}{a} = 10$, $\beta_p = 1$, and $F(\kappa a) = 8$, we therefore have

$$Z = 1.5 \times 10^4 \frac{\lambda^2}{S}\Omega. \quad (6)$$

Note that $W = 10(\gamma - 1)^2$ GW is attained at $Z = 25\ \Omega$, which is possible if $\frac{S}{\lambda^2} = 600$.

Thus, the traveling-wave tube should have a short waveguide and should operate by higher-order modes so as to produce a high output power. The conclusion agrees with experimental data.

The result for a klystron is more impressive. Using strong currents allows us to take $\frac{L}{a} \sim 0.25$. Assuming that $\beta_p \cong 1.5$ and $F(\kappa a) = 20$, we obtain

$$Z = 36\frac{\lambda^2}{S}\Omega, \quad (7)$$

indicating that the same value $Z = 25\ \Omega$ is attained at $\frac{S}{\lambda^2}$ as small as 1.4. Thus, relativistic klystrons can offer a fairly high output power when operating by the fundamental mode.

Now, look at a magnetron. Experiments indicate that its impedance is approximately equal to 25 $\Omega$ as well. Thus, relativistic magnetrons with typical anode dimensions can produce a high output power.

Finally, consider a vircator. As demonstrated in [5], its impedance can be determined from an expression relating the current density $j$ to the gap voltage $U$. For the diode of a high-current accelerator, we have

$$j = \frac{8}{9}\frac{mc^3}{e}\frac{1}{\pi d^2}\frac{(\gamma - 1)^2}{\sqrt{\gamma^2 - 1}}F_1^2, \quad 1 \le F_1 \le \frac{3}{2}. \quad (8)$$

Since $I = jS$, we obtain

$$Z = 60\pi\frac{9}{8}\frac{d^2}{S}\frac{1}{\beta}\frac{1}{F_1^2}. \quad (9)$$

Assuming that $\beta \longrightarrow 1$, we arrive at

$$Z = \frac{9}{16}Z_0\frac{d^2}{S}\frac{1}{F_1^2} \approx 250\frac{d^2}{S}\Omega. \quad (10)$$

Thus, the same power $W = 10(\gamma - 1)^2$ GW is produced at $\frac{S}{d^2} = 10$.

In fact, the vircator can give considerably higher powers, since it may attain $S \gg d^2$.

To summarize, this study covers different types of relativistic microwave oscillator. The results enable one to optimize oscillator parameters for maximum output power.

## REFERENCES

1. *High-Power Microwave Sources*, Ed. by V. Granatstein and I. Alexeff (Artech House, Massachusetts, 1987).
2. A. N. Didenko, Dokl. Ross. Akad. Nauk **356**, 470 (1997).
3. A. V. Gaponov and M. A. Miller, Zh. Éksp. Teor. Fiz. **34**, 242 (1958) [Sov. Phys. JETP **7**, 168 (1958)].
4. O. A. Val'dner, A. D. Vlasov, and A. V. Shal'nov, *Linear Accelerators* (Atomizdat, Moscow, 1969).
5. A. N. Didenko and B. V. Zverev, *SHF Energetics* (Nauka, St. Petersburg, 1995).

*Translated by A. A. Sharshakov*

*Technical Physics Letters, Vol. 26, No. 5, 2000, pp. 408–409. Translated from Pis'ma v Zhurnal Tekhnicheskoĭ Fiziki, Vol. 26, No. 10, 2000, pp. 13–16.*


# A 30-nm-Gate Field-Effect Transistor

**S. V. Obolenskiĭ and M. A. Kitaev**

*Nizhegorodskiĭ State University, Nizhny Novgorod, 630600 Russia*

Received October 29, 1999

**Abstract**—The fabrication technology is developed for and characteristics are investigated of a GaAs Schottky-barrier field-effect transistor (SBFET) with an effective gate length of 30 nm. The SBFET power gain cutoff frequency is 150 GHz. The noise factor at 12–37 GHz is comparable with that of two-dimensional electron gas transistors. The theoretical electron transit time under the gate is below 0.1 ps. © *2000 MAIK "Nauka/Interperiodica".*

It is known [1] that gate length is among the design parameters determining the frequency characteristics of Schottky-barrier field-effect transistors (SBFET). Modern lithographic installations do not provide a reliable resolution of better than 0.1 μm. Kohn [2] suggested using optical lithography to fabricate a SBFET channel in the form of a V-shaped groove, which, for a gate metallization length of 2 μm, brings the device characteristics closer to those of a SBFET with submicron gate.

In this work, the V-groove technique was implemented for the first time with the electron lithography. We used traditional $n^+$–$n$–$n^-$-GaAs structures obtained by the vapor-phase epitaxy, having a typical transient region length of about 0.15 μm between the channel and the buffer layer. Anisotropic etching in the $NH_4OH$–$H_2O_2$–$H_2O$ 1 : 0.5 : 25 etchant makes it possible to fabricate a V-shaped groove in the active layer of the GaAs structure. This, in combination with the self-alignment method [3] used for evaporation of the gate metallization, permitted us to obtain an effective gate length below 30 nm (Fig. 1). The accuracy of orientation of the fabricated device topology relative to crystallographic directions of the initial semiconductor wafer was ±3°–5°. The samples were prepared using an ELP-13 electron-beam resist, an 0.35-μm-thick layer of which was applied and then dried for 30 min at 170°C. The exposure was performed on a ZBA-21 electron-beam system with an electron beam diameter of 0.1 μm. A mixture of methyl ethyl ketone and isopropyl alcohol was used for development.

The transistor low-frequency characteristics were measured on an L2-56 characteristic tracer, and the high-frequency characteristics were measured using the R2-67, R2-65, and R2-69 panoramic meters (at 12, 37, and 60 GHz, respectively). The SBFET dynamic characteristics were measured with the help of precision probe heads used for nondestructive monitoring of the gain and noise factors directly on the crystals. From the available set of transistors with different gate lengths, we selected devices with optimum parameters for each frequency band: 200 μm (with gate-source input capacitance $C$ = 0.15 pF) for 12 GHz, 100 μm (with $C$ = 0.08 pF) for 37 GHz, and 50 μm (with $C$ = 0.05 pF) for 60 GHz.

The device current–voltage characteristic has a traditional form. The transistor saturation current is about 7 mA (for a gate length of 50 μm). The transconductance exceeds 400 mS/mm. Experimental frequency characteristics of maximum gain, minimum noise factor, and the corresponding optimum gain are presented in Fig. 2. The theoretically estimated power gain cutoff frequency is about 150 GHz.

Theoretical calculations performed in the relaxation time approximation [4, 5] show that the carrier transit time under the gate is about 0.1 ps (ballistic transit) and the transistor on-to-off switching time is below 1 ps. These data allow us to expect a (2–3)-fold increase in

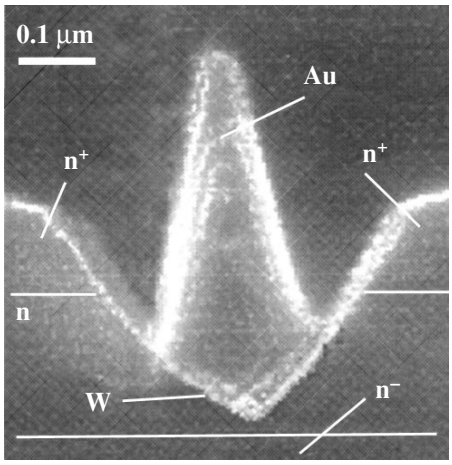


**Fig. 1.** SEM micrograph of the cross-section of a recessed-gate field-effect transistor. The doping levels of GaAs layers are $10^{15}$ cm$^{-3}$ (for the $n^-$ buffer layer), $5 \times 10^{17}$ cm$^{-3}$ (for the $n$ channel), and $10^{19}$ cm$^{-3}$ (for the $n^+$ contact layer). The material used for the gate metallization is Au with a sublayer of W.

1063-7850/00/2605-0408$20.00 © 2000 MAIK "Nauka/Interperiodica"

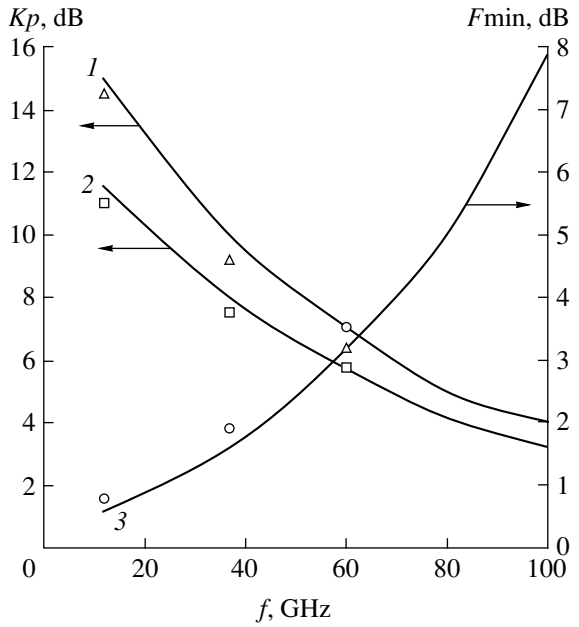


**Fig. 2.** FET high-frequency characteristics: (*1*) maximum power gain, (*2*) optimum power gain, and (*3*) minimum noise factor. Solid lines show the results of theoretical calculations.

the power gain cutoff frequency after lowering the input capacitance by decreasing the gate width to 7–15 μm.

The greatest influence on the charge carrier motion under the gate has the velocity overshoot. The maximum carrier velocity in the channel is $8 \times 10^7$ cm/s, which agrees with the data presented in [4]. Due to the presence of a V-shaped groove, the velocity undershoot is lower than that in a conventional transistor with the same gate length, which is an additional factor improving the device performance. The latter effect can be explained by a different distribution of electric field in the gate–drain gap, which, in turn, affects the distribution of the electron gas temperature in the channel, reduces dimensions of the static Gunn domain, and shifts it to the drain. The electrons pass from *L* to Γ valley through the $n^+$ GaAs contact layer (near the drain).

The lowest noise level was obtained for a channel thickness (in its narrow part) comparable to the size of a depletion region (normally-off transistor). In this case, the optimum gate bias voltage is +0.15 V. This can probably be explained by a lower efficiency of the carrier scattering during their motion in the layer immediately adjacent the *n* channel. Because of the charge carrier diffusion, the conductance of this layer is comparable with that of the channel, which additionally lowers the noise resistance. As a result, the transistor noise factor at 12 GHz is below 0.8 dB for a gain factor of 11.5 dB, which compares to the noise factor of two-dimensional electron gas transistors.

Thus, the presented results demonstrate that one can use standard epitaxial GaAs structures to fabricate a SBFET with characteristics approaching those of two-dimensional electron gas transistors (such as HEMT and PMHEMT) by creating gates with an effective gate length of several tens of nanometers.

## REFERENCES

1. D. M. Gill, B. C. Cane, S. P. Svensson, *et al.*, IEEE Trans. Electron Devices **ED-17**, 328 (1996).
2. E. Kohn, Electron. Lett. **11**, 160 (1975).
3. C. L. Cheng, L. A. Coldren, B. I. Miller, *et al.*, IEEE Trans. Electron Devices **ED-31**, 840 (1984).
4. B. Carnez, A. Cappy, A. Kaszinski, *et al.*, J. Appl. Phys. **51**, 784 (1980).
5. S. V. Obolenskiĭ and G. P. Pavlov, Fiz. Tekh. Poluprovodn. (St. Petersburg) **29**, 413 (1995) [Semiconductors **29**, 211 (1995)].

*Translated by A. Kondrat'ev*

*Technical Physics Letters, Vol. 26, No. 5, 2000, pp. 410–411. Translated from Pis'ma v Zhurnal Tekhnicheskoĭ Fiziki, Vol. 26, No. 10, 2000, pp. 17–21.*


# The Effect of Illumination on the Electric and Photoelectric Properties of μ*c*-Si : H Films Weakly Doped with Boron

**A. G. Kazanskiĭ[1], S. N. Kozlov[1], H. Mell[2], and P. A. Forsh[2]**

[1] *Moscow State University, Moscow, 119899 Russia*

[2] *Philipps-Universitat Marburg, D-35032 Marburg, Germany*

Received November 15, 1999

**Abstract**—The electric conductivity and photoconductivity of μ*c*-Si : H films weakly doped with boron increase upon exposure of the samples to light in the band of intrinsic absorption. It is shown that the effect is related to changes in the ambient medium, probably, to the photoinduced charging of oxygen molecules adsorbed on the μ*c*-Si : H films. © *2000 MAIK "Nauka/Interperiodica".*

In recent years, microcrystalline hydrogenated silicon (μ*c*-Si : H) has drawn the attention of researchers because of good prospects for the use of this material in optoelectronics. This is related to a considerable extent to the fact that electric properties of the undoped μ*c*-Si : H films, in contrast to those of the amorphous hydrogenated silicon, exhibit no degradation during prolonged exposure to light [1]. As is known, the undoped μ*c*-Si : H films possess a comparatively high conductivity of the *n*-type ($10^{-4}$–$10^{-3}$ $\Omega^{-1}$ cm$^{-1}$) [2], related to uncontrolled oxygen impurity introduced during the film preparation [3], and low photosensitivity [2].

It was reported that the introduction of a small amount of boron into μ*c*-Si : H decreases the conductivity by several orders of magnitude [1, 2, 4] and, which is especially important, markedly increases the photosensitivity [1, 2, 4]. However, no data were reported on the stability of boron-doped μ*c*-Si : H films with respect to prolonged illumination. The purpose of this work was to study the effect of light on the electric and photoelectric properties of μ*c*-Si : H weakly doped with boron.

The experiments were performed with boron-doped μ*c*-Si : H films prepared at Marburg University by chemical vapor deposition (CVD) from a glow-discharge decomposed mixture of monosilane ($SiH_4$), diborane ($B_2H_6$), and hydrogen. The initial gas mixture contained 98.5% $H_2$, while the diborane to monosilane molar ratio was $B_2H_6/SiH_4 = 4 \times 10^{-6}$. Silicon films with a thickness of 0.6–0.7 μm were deposited onto quartz substrates heated to a temperature of 220°C. For the electrical measurements, the samples were provided with vacuum-deposited magnesium contacts. The photoconductivity was measured on the films excited by light quanta with an energy of 1.8 eV at a light beam intensity of $5 \times 10^{14}$ cm$^{-2}$ s$^{-1}$. The effect of prolonged illumination at room temperature on the dark conductivity ($\sigma_d$) and photoconductivity ($\sigma_{ph}$) of the film samples was studied using an incandescent lamp with a thermal filter (light intensity, 60 mW/cm$^2$). Prior to exposure, the films were annealed for 30 min at 180°C in a vacuum of $10^{-3}$ Pa. The electric measurements were performed in vacuum or in dry air.

According to the data of scanning and transmission electron microscopy, the film morphology comprised a system of "columns" with a diameter of 30–100 nm. The columns, oriented perpendicularly to the film surface, were composed of 3–30 nm microcrystallites [5]. Analysis of the Raman spectra showed that scattering from the crystalline component accounts for 85% of the total peak area [5]. The results of thermo emf measurements indicated that the films possess conductivity of the *p* type.

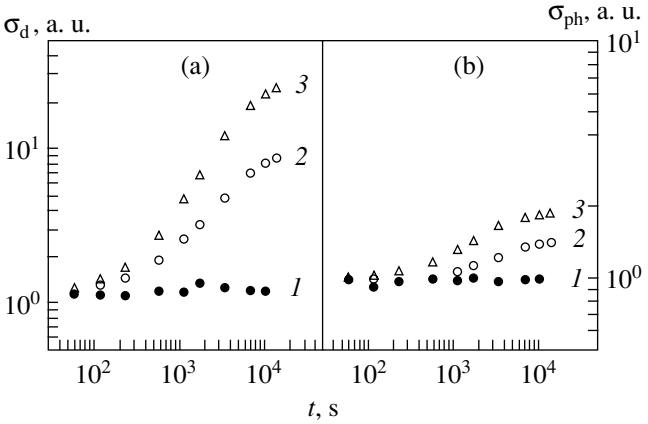


**Fig. 1.** The plots of relative variation in (a) conductivity and (b) photoconductivity of μ*c*-Si : H films versus the time of their preliminary illumination (*1*) in a vacuum of $10^{-3}$ Pa and in dry air at a pressure of (*2*) 10 or (*3*) $10^5$ Pa.

1063-7850/00/2605-0410$20.00 © 2000 MAIK "Nauka/Interperiodica"

Our investigations showed that the electric conductivity and photoconductivity of μ*c*-Si : H films weakly doped with boron are independent of the ambient medium (vacuum versus dry air). At the same time, conditions of the prolonged illumination of the samples significantly affected the pattern of variation in the electric and photoelectric properties. As seen from Fig. 1, illumination of the films in a vacuum of $10^{-3}$ Pa changed neither $\sigma_d$ nor $\sigma_{ph}$ values. At the same time, illumination of the μ*c*-Si : H films in dry air increased both the conductivity and photoconductivity of the samples. A reduction in residual pressure in the working chamber decreased the observed effect.

Figure 2 shows the plots of conductivity versus reciprocal temperature for a vacuum-annealed μ*c*-Si : H film sample measured before (curve *1*) and after (curve *2*) a 4-h illumination at room temperature in dry air at a pressure of 10 Pa. In both cases, the conductivity measurements were performed in a vacuum of $10^{-3}$ Pa in the heating mode. As seen, the temperature dependence of $\sigma_d$ for the annealed sample exhibits the thermoactivation character with an activation energy of $E_a = 0.43$ eV. Prolonged illumination in dry air leads to increasing conductivity and decreasing $E_a$. As the sample temperature increased (Fig. 2, curve *2*), a change in the conductivity induced by preliminary illumination in dry air was gradually "annealed" and the initial conductivity was restored at $T > 450$–460 K.

In our opinion, the observed effects can be related to the trapping of photogenerated electrons on the orbitals of oxygen molecules adsorbed at the surface of columns and the outer surface of the μ*c*-Si : H films. Effects of this type were previously reported for real [6] and thermally oxidized [7] silicon surfaces. The adsorption-induced electron states manifested in these effects are separated from the bulk of the semiconductor by a potential barrier related to a thin surface oxide layer. This barrier can be surmounted only by most energetic ("hot") electrons photogenerated in the bulk. In crystals with an imperfect surface oxide structure, the optical threshold of negative photoinduced charging of the adsorption electron states falls within the visible spectral range ($h\nu > 2.6$ eV [6]). Trapping of the electron increases the binding of an adsorbed molecule to the surface, so that the desorption is also possible at elevated temperatures ($T \geq 450$–460 K) (Fig. 2).

Negative photoinduced charging of the μ*c*-Si : H film surface leads to a growth in the hole concentration in the film and increases their mobility at the expense of decreasing potential barrier on the column boundaries. This results in an increasing electric conductivity of the films. A growth in the photoconductivity is probably related to a decrease in the rate of minority carrier recombination, which is caused by changes in the surface potential of μ*c*-Si : H microcrystallites.

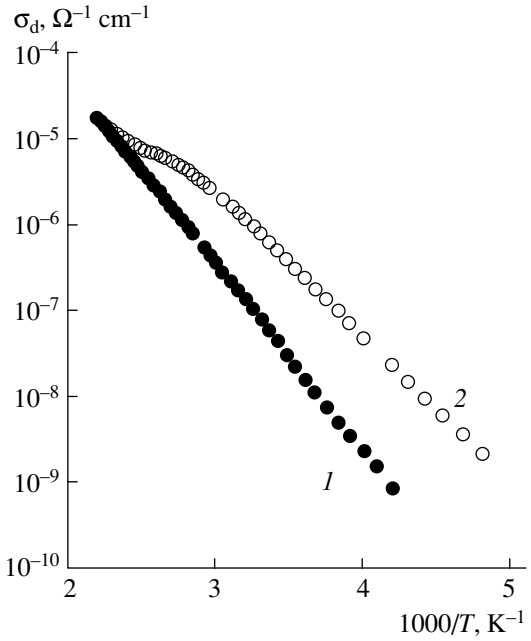


**Fig. 2.** The plot of dark conductivity versus reciprocal temperature for a vacuum-annealed μ*c*-Si : H film measured (*1*) before and (*2*) after 4-h illumination at room temperature in dry air at a pressure of 10 Pa. The conductivity measurements were performed in a vacuum of $10^{-3}$ Pa.

The above data suggest that changes in the electric conductivity and photoconductivity must also take place in the undoped μ*c*-Si : H films upon prolonged illumination, but these changes may be less distinguishable against the higher conductivity and lower photoconductivity of this material.

This work was supported by the INTAS Foundation, project no. 97-1910.

## REFERENCES

1. M. J. Williams, C. Wang, and G. Lucovsky, Mat. Res. Soc. Symp. Proc. **219**, 389 (1991).
2. R. Fluckiger, J. Meier, M. Goetz, *et al.*, J. Appl. Phys. **77**, 712 (1995).
3. P. Torres, J. Meier, R. Fluckiger, *et al.*, Appl. Phys. Lett. **69**, 1373 (1996).
4. M. Bruggemann, A. Heirzenberger, P. Reining, *et al.*, J. Non-Cryst. Solids **227**–**230**, 982 (1998).
5. D. Ruff, H. Mell, L. Toth, *et al.*, J. Non-Cryst. Solids **227**–**230**, 1011 (1998).
6. S. N. Kozlov and S.N. Kuznetsov, Fiz. Tekh. Poluprovodn. (Leningrad) **12**, 1680 (1978) [Sov. Phys. Semicond. **12**, 995 (1978)].
7. S. N. Kozlov and S. N. Kuznetsov, Izv. Vyssh. Uchebn. Zaved., Fiz. **1**, 92 (1981).

*Translated by P. Pozdeev*

*Technical Physics Letters, Vol. 26, No. 5, 2000, pp. 412–414. Translated from Pis'ma v Zhurnal Tekhnicheskoĭ Fiziki, Vol. 26, No. 10, 2000, pp. 22–27.*


# Optical Absorption of the $Gd_3Ga_5O_{12}$ Epitaxial Films Grown from $Bi_2O_3$–$B_2O_3$–CaO Solution Melt System

**V. V. Randoshkin, N. V. Vasil'eva, V. G. Plotnichenko, A. M. Saletskiĭ, K. V. Stashun, and N. N. Sysoev**

*United Laboratory of Magnetooptoelectronics, Institute of General Physics (Russian Academy of Sciences) and Mordvinian State University, Saransk, Mordvinia, Russian Federation*

*Scientific Center of Fiber Optics, Institute of General Physics (Russian Academy of Sciences) and Moscow State University, Moscow, Russia*

Received December 8, 1999

**Abstract**—Single-crystalline garnet films with a stoichiometric composition of $Gd_3Ga_5O_{12}$ were grown for the first time by liquid phase epitaxy from a supercooled melt of the $Bi_2O_3$–$B_2O_3$–CaO solid solution system. The films exhibit no absorption bands in the visible spectral range. © *2000 MAIK "Nauka/Interperiodica".*

Optically active epitaxial single-crystalline garnet (SCG) films of various compositions are usually grown from supercooled melts of PbO– $B_2O_3$ based solid solutions [1–5]. A disadvantage of this system is that the solvent components $Pb^{2+}$ and $Pb^{4+}$ enter into the garnet composition, which results in additional optical absorption in the visible spectral range [5] and hinders creation of the film lasers operating in this range. Moreover, the optical absorption spectra of SCG films grown under identical conditions from the same Pb-containing solution melt exhibited considerable scatter [5]. This is manifested, in particular, by different colors of sequentially grown epitaxial films [2].

The purpose of this work was to grow $Gd_3Ga_5O_{12}$ SCG films on (111)-oriented $Gd_3Ga_5O_{12}$ substrates by liquid phase epitaxy (LPE) from a supercooled melt of the $Bi_2O_3$–$B_2O_3$–CaO solid solution system and to study the optical absorption spectra of these films. It was expected that the films would exhibit no additional optical absorption caused by the $Pb^{2+}$ and $Pb^{4+}$ ions. CaO was introduced into the melt in order to compensate for the charge of the possible admixture of $Pt^{4+}$ ions.

The SCG films were grown from a charge with the following molar ratios of components:

$$R_1 = Ga_2O_3/Gd_2O_3 \approx 2.9\text{–}4.8,$$

$$R_2 = Bi_2O_3/B_2O_3 \approx 16.1\text{–}16.3,$$

$$R_2 = CaO/B_2O_3 \approx 1.00,$$

$$R_3 = (Gd_2O_3 + Ga_2O_3)/(Gd_2O_3 + Ga_2O_3 + Bi_2O_3 + CaO + B_2O_3) \approx 0.087\text{–}0.097.$$

The melt was homogenized in a platinum crucible for not less than 240 min, after which the temperature was decreased for 60 min to reach the growth temperature $T_{gr}$; the solution melt was kept at this temperature for ~20 min. Then a substrate was immersed into the melt to grow an SCG film sample. The melt supercooling $\Delta T$ was gradually increased from one series of experiments to another. A minimum $\Delta T$ value in various series varied from 1.5 to 23 K. The film growth time was about 30 min and the total film thickness ($2h$) grown on both sides of the substrate was determined by weighing the substrate before immersion and the grown epitaxial structure upon withdrawal [2]. The optical transmission spectra were measured on a Perkin-Elmer Lambda 900 spectrophotometer.

The final parameters of some SCG films grown at various temperatures ($T_{gr}$) and growth rates ($f_{gr}$) are listed in the table. In our experiments, the samples sequentially grown under otherwise identical conditions exhibited no variation in their color, in contrast to what was observed for the films grown from the Pb-containing melt [2]. The samples grown from the $Bi_2O_3$–$B_2O_3$–CaO melt appeared as colorless and transparent.

Parameters of epitaxial semicrystalline garnet films grown from $Bi_2O_3$–$B_2O_3$–CaO (samples 1–3) and PbO–$B_2O_3$ (samples 4 and 5) solution melts

| Sample | $T_{gr}$, °C | $f_{gr}$, μm/min | $2h$, μm | $\lambda_{0.1}$, nm |
|---|---|---|---|---|
| 1 | 896 | 0.22 | 12.92 | 314 |
| 2 | 886 | 0.39 | 24.82 | 321 |
| 3 | 886 | 0.30 | 18.46 | 317 |
| 4 | 932 | 0.74 | 29.8 | 365 |
| 5 | 932 | 0.24 | 9.4 | 289 |

1063-7850/00/2605-0412$20.00 

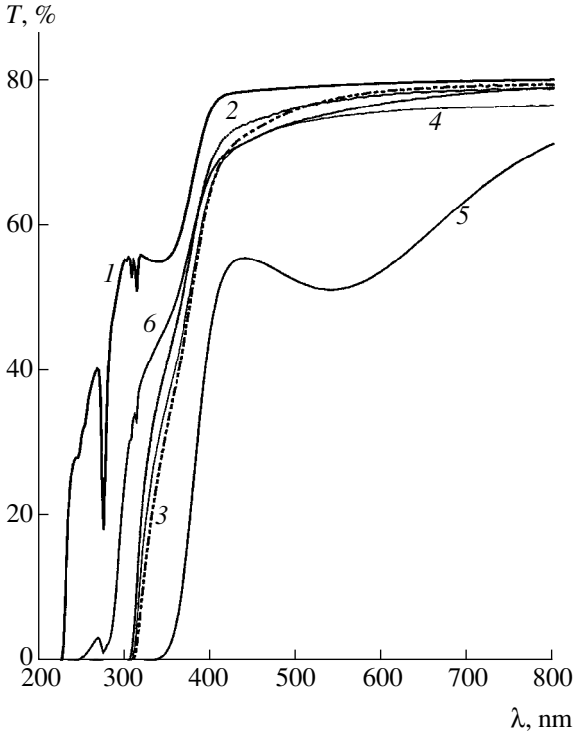


**Fig. 1.** Optical transmission spectra of (*1*) $Gd_3Ga_5O_{12}$ substrate and (*2–6*) epitaxial SCG films grown from (*2–4*) $Bi_2O_3$–$B_2O_3$–CaO melts (samples 1–3, respectively) and (*5*, *6*) PbO–$B_2O_3$ melts (samples 4 and 5).

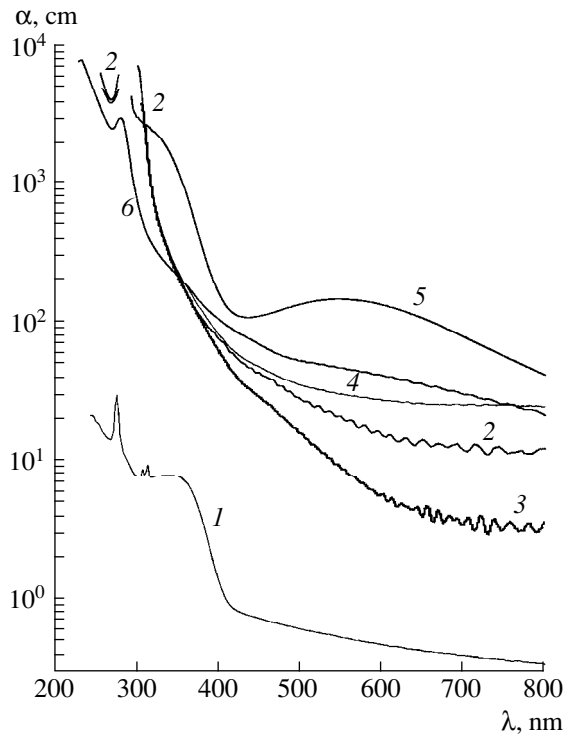


**Fig. 2.** Reduced optical absorption spectra of (*1*) $Gd_3Ga_5O_{12}$ substrate and (*2–6*) epitaxial SCG films grown from $Bi_2O_3$–$B_2O_3$–CaO PbO–$B_2O_3$ solution melts. Numbers at the curves refer to the same sample as in Fig. 1.

Figure 1 shows the optical transmission spectra of a $Gd_3Ga_5O_{12}$ substrate (curve *1*) and the epitaxial SCG samples 1–3 grown from a $Bi_2O_3$–$B_2O_3$–CaO solution melt (curves *2–4*) in comparison with the spectra of two films (samples 4 and 5, having smaller and greater thicknesses than the former films, respectively) grown from a PbO– $B_2O_3$ based solution melt (curves *5* and *6*).

As seen from Fig. 1, all the epitaxial films studied exhibit additional absorption as compared to that of the substrate. The transmission band edge of the SCG films was characterized by $\lambda_{0.1}$ (see table), representing a wavelength at which the transmission *T* drops to 10% of the maximum value. Note that the $\lambda_{0.1}$ values of SCG films grown from the $Bi_2O_3$–$B_2O_3$–CaO solution melt vary in the series of sequential samples [5] to a lesser extent than in the films grown from the PbO– $Ba_2O_3$ solution melt.

Figure 1 demonstrates that the transmission spectra of SCG films grown from the $Bi_2O_3$–$B_2O_3$–CaO solution melt (curves *2–4*) exhibit no significant absorption in the region of $\lambda \approx 550$ nm characteristic of sufficiently thick Pb-containing films (curve *6*). This circumstance is promising from the standpoint of creating film lasers emitting in the visible spectral range.

Figure 2 presents the spectra of absorbance $\alpha(\lambda)$ (normalized to the film thickness) of SCG films grown from the $Bi_2O_3$–$B_2O_3$–CaO solution melt. These curves were obtained by mathematical processing of the transmission spectra in Fig. 1, whereby the transmittance *T* of a substrate with the film was divided by that of the pure substrate (measured before growth) and a logarithm of this ratio was divided by the total thickness of layers grown on both sides of the substrate. As seen, curves *2–4* exhibit an absorption band in the region of $\lambda \approx 290$ nm. This absorption can be attributed to the most longwave transition in bismuth ions $^1S_0 \longrightarrow {}^3P_1$ in nonferromagnetic garnets [6]. However, this assignment has to be verified by further investigations of the optical absorption in SCG films grown.

A weak absorption in the region of $\lambda \approx 280$ nm is also present in the spectra of SCG films grown from the PbO–$B_2O_3$ based solution melt (Fig. 2, curve *6*). This band can be assigned to an intra-ion transition in $Pb^{2+}$, such as $(G_s^2)^1 - S_0 \longrightarrow {}^3P_1$.

Thus, the results of our experiments have demonstrated that epitaxial SCG films with a stoichiometric composition of $Gd_3Ga_5O_{12}$ grown by LPE from a $Bi_2O_3$–$B_2O_3$–CaO solution melt system possess additional optical absorption in the UV range (near 290 nm) in comparison to the $Gd_3Ga_5O_{12}$ substrates. At the same time, these films exhibit no absorption bands in the visible spectral range at $\lambda \approx 550$ nm (characteristic of the garnets grown from the PbO–$B_2O_3$ based solution

melt). This property is promising from the standpoint of creating film lasers emitting in the visible spectral range.

This work was partly supported by the Russian Foundation for Basic Research (project no. 99-02-18427).

## REFERENCES

1. P. A. Arsen'ev, Kh. S. Bagdasarov, and V. V. Fenin, *Growth of Single-Crystalline Films for Quantum Electronics* (Mosk. Énerg. Inst., Moscow, 1981).
2. V. V. Randoshkin, A. M. Belovolov, M. I. Belovolov, *et al.*, Kvantovaya Élektron. **25**, 233 (1988).
3. B. Ferrand, B. Chambaz, and M. Couchaud, Opt. Mater. **11**, 101 (1999).
4. V. V. Randoshkin, N. V. Vasil'eva, A. M. Saletskiĭ, *et al.*, *Physical Thought in Russia* (in press).
5. V. V. Randoshkin, N. V. Vasil'eva, A. M. Saletskiĭ, *et al.*, Pis'ma Zh. Tekh. Fiz. (2000) (in press).
6. V. V. Randoshkin and A. Ya. Chervonenkis, in *Applied Magnetooptics* (Énergoatomizdat, Moscow, 1990), p. 50.

*Translated by P. Pozdeev*

*Technical Physics Letters, Vol. 26, No. 5, 2000, pp. 415–417. Translated from Pis'ma v Zhurnal Tekhnicheskoĭ Fiziki, Vol. 26, No. 10, 2000, pp. 28–34.*


# Remote Interferometer with Polarizing Beam Splitting

**O. I. Kotov, L. B. Liokumovich, S. I. Markov, A. V. Medvedev, and V. M. Nikolaev**

*St. Petersburg State Technical University, St. Petersburg, 195251 Russia*

Received December 30, 1999

**Abstract**—A scheme of an optoelectronic system built around a remote Mach–Zehnder interferometer was developed and experimentally studied. The output signal of the interferometer is detected under pseudoheterodyne conditions using the polarizing beam splitting and a sawtooth phase modulation. It is demonstrated that the system is insensitive to external noise in the forward and backward optical channels. © *2000 MAIK "Nauka/Interperiodica".*

Optical interferometers are frequently employed in physical measurements and of or monitoring moving objects [1]. Present-day needs are best met by distributed systems that combine high accuracy, wide dynamic range, and large bandwidth with the possibility of remote operation and reliable optical signal transmission from local units to the remote sensor. This paper presents a system built around a remote two-beam optical interferometer with polarizing beam splitting and ancillary sawtooth phase modulation. Although analogs of the system have been reported [2–8], they suffer from fluctuations of the optical path length in the channel going to the remote portion of the instrument, since their interferometers had extended arms for remote measurements.

In the scheme we suggest (Fig. 1), a remote portion of the instrument includes the entire sensor, whereas the local portion contains a light source (gas laser) and electronic equipment. It is demonstrated that the system is insensitive to external noise in the forward optical channel. The sensor is a two-beam Mach–Zehnder interferometer with the input polarizing beam splitting. Its output signal goes through the backward channel to a photodetector connected to processing units. The laser output is subjected to ancillary phase modulation in an electrooptical crystal (see block *2* in Fig. 1). The interferometer is sensitive to difference in the arm lengths. It may embody the principle of reference and signal arms or the differential principle, whereby an external factor changes the arm lengths oppositely. If the forward channel is isotropic, it does not change the phase difference between interfering beams and hence does not affect measurements.

A detailed analysis of the instrument together with a theoretical and experimental study of the phase-difference modulation employed and the interferometer misalignment distortions have been presented in [6]. Here, we consider (1) pseudoheterodyne detection using ancillary sawtooth modulation of the phase dif-

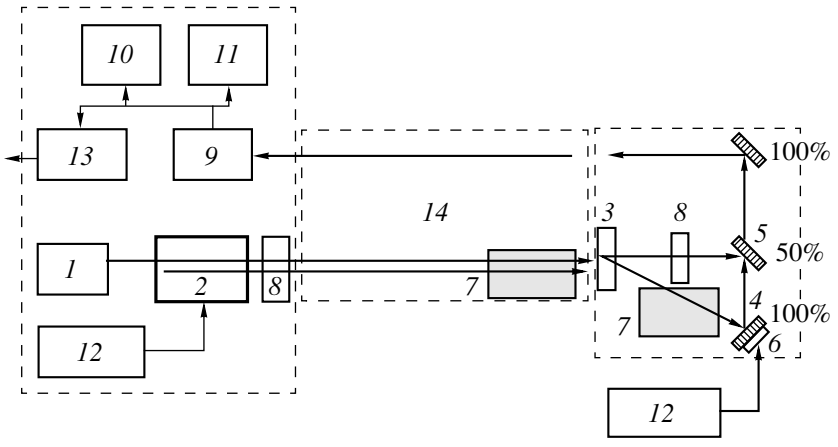


**Fig. 1.** Block diagram of the instrument: (*1*) LGN-207 gas laser; (*2*) ML-102 electrooptical modulator (polarizers removed); (*3*) polarizing beam splitter; (*4*) mirror; (*5*) semireflecting mirror; (*6*) piezo-ceramics cylinder; (*7*) cell with water; (*8*) λ/2 phase plate; (*9*) photodetector; (*10*) oscilloscope; (*11*) spectrum analyzer; (*12*) oscillator; (*13*) phase meter; (*14*) optical channel.

1063-7850/00/2605-0415$20.00 © 2000 MAIK "Nauka/Interperiodica"

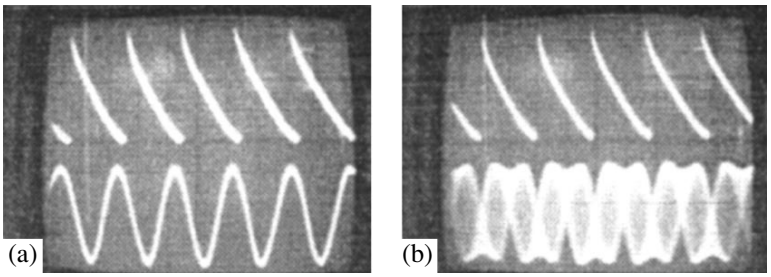


**Fig. 2.** Oscilloscope traces obtained in the (a) absence or (b) presence of phase modulation in the interferometer, the modulation index being π. In each panel, the upper portion shows the modulating voltage across the local electrooptical crystal, whereas the lower portion, the output of the photodetector.

ference and (2) suppression of noise in the forward channel.

In our experiment, we used a He–Ne laser (LGN-207) providing linearly polarized radiation with a wavelength of 0.63 μm and a power of 2 mW. The input and the output polarizer of the modulator were removed. Let α denote the azimuth of the radiation with respect to the birefringence axis (*OX*) of the electrooptical crystal. If $\alpha \neq 0°$ and $\alpha \neq 90°$, the phase difference Γ between the orthogonal components $E_x$ and $E_y$ at the output of the crystal varies according to a sawtooth control voltage. After the modulator, the beam passes through a λ/2 phase plate and the forward channel, coming to the polarizing beam splitter. Generally speaking, the environment can make the channel anisotropic so that the phase difference between the orthogonal components would change by a certain quantity γ. Also, the axes of the crystal and the Rochon prism may be misaligned by a certain angle β. The prism splits the beam into the $E_x$ and $E_y$ components, which propagate along respective arms of the interferometer. One of the arms includes a λ/2 plate for matching beam azimuths at semireflecting mirror *5*. The output of the interferometer is a linearly polarized beam with modulated intensity. The modulation is picked up by the photodetector. An external action on the interferometer modifies the phase difference φ between the beams at mirror *5*.

According to [6], a lossless interferometer gives the normalized output intensity

$$I_{\text{out}} = 1 - \cos(2\alpha)\sin(4\beta)\sin(\gamma) - \sin(2\alpha)\cos(2\beta) \times [\cos^2\beta\sin(\varphi + \Gamma + \gamma) + \sin^2\beta\sin(\varphi + \Gamma + \gamma)]. \quad (1)$$

Optimal operation is achieved at

$$\alpha = 45°, \quad \beta = 0. \quad (2)$$

Note that the condition β = 0 is satisfied by means of the λ/2 plate *8*. In view of (2), formula (1) is simplified as follows:

$$I_{\text{out}} = 1 - \sin(\varphi + \Gamma + \gamma). \quad (3)$$

This expression is a typical interferometer waveform with the ancillary modulation Γ(*u*(*t*)). The processing units extract φ(*t*), which gives information about the external action on the sensor. If the forward channel becomes anisotropic (in the operating band), producing a phase shift γ(*t*), then a spurious signal arises at the output, since γ(*t*) cannot be differentiated from the desired signal φ(*t*).

With a sawtooth voltage *u*(*t*) of frequency Ω, the modulation index $\Gamma_{\max}$ being 2π, expression (3) can be reduced to [4].

$$I_{\text{out}} = 1 - \sin(\Omega t + \varphi_0), \quad \varphi_0 = \varphi(t) + \gamma(t). \quad (4)$$

This is equivalent to the heterodyne detection of the interferometer signal, whereby a variation in φ results in the same phase shift of the subcarrier with frequency Ω at the photodetector output.

Once the interferometer had been aligned [see condition (2)], a 1-kHz sawtooth voltage (see the upper portion of Fig. 2a) was applied to the modulator. The amplitude of the modulating signal was chosen so that the phase difference between $E_x$ and $E_y$ be 2π. The photodetector produced a sine signal (see the lower portion of Fig. 2a) identical to heterodyne signal (4). Detection was tested by applying a "signal" phase modulation to one of the interferometer beams with the help of mirror *4* attached to a piezo-ceramic cylinder.

If a 100-Hz harmonic voltage is applied to the cylinder, the subcarrier (of frequency 1 kHz) becomes modulated in phase at 100 Hz, the amplitude being constant (Fig. 2b).

The alignment of the electronics under pseudoheterodyning conditions consisted in setting the amplitude of the sawtooth modulating voltage so that the phase difference be 2π.

The desired signal was extracted from the detected signal with a phase meter (Fig. 2b).

In the experiment, we also evaluated the sensitivity of the instrument to external noise in the forward channel. To this end, a 10-cm-thick glass cell with water of variable temperature was inserted into the optical path. If the cell is placed in the arm of the interferometer, heating the water causes a considerable phase shift of the subcarrier (see curve *a* in Fig. 3), due to a variation in the refractive index and hence, in the optical path length. If the cell is in the forward channel, subcarrier

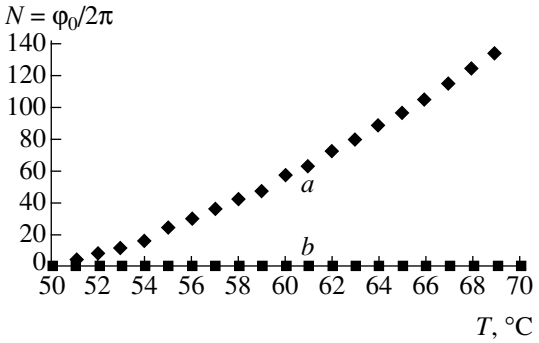


**Fig. 3.** Subcarrier phase shift vs. water temperature in, the cell placed (*a*) in the interferometer arm or (*b*) in the forward channel.

phase varies insignificantly ($\ll 2\pi$) and irregularly (see curve *b* in Fig. 3). The latter feature seems to stem from thermal fluctuations in $\varphi$. We attribute the temperature insensitivity of the subcarrier phase and, hence, of the instrument readings to the isotropy of the propagation medium (water). The system is expected to assure $\gamma(t) \ll \varphi(t)$ in most common cases of real interferences.

In conclusion, note that the instrument may be constructed in optical-fiber technology.

## REFERENCES

1. N. N. Evtikheev, É. A. Zasovin, and D. I. Mirovitskiĭ, Itogi Nauki Tekh., Ser. Svyaz' **8**, 4 (1991).
2. V. L. Fedorin and V. L. Shur, Tr. Metrol. Inst. SSSR **240** (300), 54 (1979).
3. A. V. Kotkov, N. E. Lebedeva, and V. L. Shur, Tr. Metrol. Inst. SSSR **240** (300), 70 (1979).
4. V. M. Khavinson, in *Proceedings of the IX Conference IPEF/UMNE-4, 1997*, pp. 119–122.
5. V. L. Fedorin and V. L. Shur, Izmer. Tekh., No. 9, 34 (1993).
6. O. I. Kotov, L. B. Liokumovich, S. I. Markov, *et al.*, in *Proceedings of the V International Scientific and Technical Conference on Radiolocation, Navigation, and Communications, Voronezh, April 20–23, 1999*, Vol. 3, pp. 1377–1388.
7. A. D. Kersey, Proc. SPIE **1797**, 161 (1993).
8. S. P. Ganevskiĭ, O. T. Kotov, L. B. Liokumovich, *et al.*, Pis'ma Zh. Tekh. Fiz. **21**, 62 (1995) [Tech. Phys. Lett. **21**, 380 (1995)].

*Translated by A. A. Sharshakov*

*Technical Physics Letters, Vol. 26, No. 5, 2000, pp. 418–419. Translated from Pis'ma v Zhurnal Tekhnicheskoĭ Fiziki, Vol. 26, No. 10, 2000, pp. 35–39.*


# The Effect of Space Charge on Electron–Wave Instabilities near Cut-off Frequencies of the Slow-Wave Structure

**N. O. Bessudnova and A. G. Rozhnev**

*Saratov State University, ul. Dvadtsatiletiya VLKSM 112a, Saratov, 410071 Russia*

Received September 1, 1999

**Abstract**—For a linear-beam microwave tube, the effect of space charge on signal generation and amplification in the electron flux–electromagnetic field system near a cut-off frequency of a slow-wave structure is studied numerically. In a parameter plane, regions of operation regimes are delineated. It is demonstrated that the space charge facilitates the oscillation near the higher cut-off frequency, but hampers that near the lower cut-off frequency. © *2000 MAIK "Nauka/Interperiodica".*

The interaction of linear electron beams with an electromagnetic field near a cut-off frequency of the slow-wave system is employed in relativistic orotrons and high-power traveling-wave tubes. Comprehensive theoretical treatment of the devices entails investigating their electron–wave instabilities, since these mechanisms dictate the conditions of desired or spurious oscillation [1]. This type of research was pioneered in [2]. However, that work was restricted to the case of an infinitesimal space charge, which is far from reality. The point is that an increased space charge may cause a transition from absolute to convective instability or vice versa, thus hampering or facilitating oscillation. On the other hand, taking the space charge into account leads to a multiparametric problem. This topic is important for the entire theory of wave phenomena, currently investigated by researchers in many fields, such as chemical kinetics [3], where the instability of a multiparametric kinetic system was studied with an allowance for diffusion.

Let us consider the interaction between a linear electron beam and a synchronous component of the longitudinal electric field near a cut-off frequency of the slow-wave structure [2]. Allowing for space charge, the equations describing this system can be written in the following form:

$$\left(\frac{\partial}{\partial\xi} - iB\right)^2\tilde{I} = i(\tilde{F} + iq\tilde{I}), \quad \frac{\partial\tilde{F}}{\partial\tau} + i\mu\frac{\partial^2\tilde{F}}{\partial\xi^2} = -\tilde{I}, \quad (1)$$

where $\tilde{F}(\xi, \tau)$ and $\tilde{I}(\xi, \tau)$ are slowly varying amplitudes of the RF field and current, respectively; $B$ indicates the degree to which the synchronism between the beam and the critical wave is violated; and $q$ refers to the space charge [2]. Specifically, $q = [\omega_p/(\omega_0\varepsilon)]^2$, where $\omega_p$ is the plasma oscillation frequency of the beam, $\omega_0$ is the critical frequency, and $\varepsilon$ is an interaction parameter. In (1), $\mu = 1$ for the lower cut-off frequency and $\mu = -1$ for the higher cut-off frequency. Equations (1) are derived and discussed in [2].

The dispersion relationship for equations (1) is

$$\Omega(\beta) = \mu\beta^2 + \frac{1}{(\beta + B)^2 - q}. \quad (2)$$

The frequency $\Omega(\beta)$ is an analytic function everywhere except for the first-order poles $\beta_{1,2} = -B \pm \sqrt{q}$. They relate to the dispersion of an electron stream that does not interact with the wave in the slow-wave structure. A formal solution of the initial problem is offered by the Fourier integral, the singularities being circumvented according to the condition $\tilde{I}(\xi, \tau) = 0$ as $\xi \longrightarrow -\infty$. This means that the field attenuates in the direction opposite to that of the beam propagation.

Let us consider the time evolution of a perturbation whose spatial distribution is given at an initial instant. In other words, we are going to examine the system for absolute instability. The method developed in [2] tells us that absolute instability is present if the complex plane of $\beta$ contains saddle points $\beta_s$ for which $\mathrm{Im}\,\Omega(\beta_s) < 0$ and $\mathrm{Im}\,\beta_s > 0$. Recall that a saddle point is characterized by the equation

$$d\Omega/d\beta = 0. \quad (3)$$

The first inequality states that a small initial perturbation with wavenumber $\beta_s$ must grow, whereas the second inequality follows from the circumvention rule. Computation testifies to the absolute instability if $B$ is above a certain critical level $B_c$ for the low-frequency boundary ($\mu = 1$) or below the critical level for the high-frequency boundary ($\mu = -1$). Plots of the critical level $B_c(q)$ are depicted in Fig. 1, which shows that, for $\mu = -1$, increasing space charge results in absolute instability if $B > 1.755$; for $\mu = 1$, the increase suppresses absolute instability if $B > 0$. Thus, the space

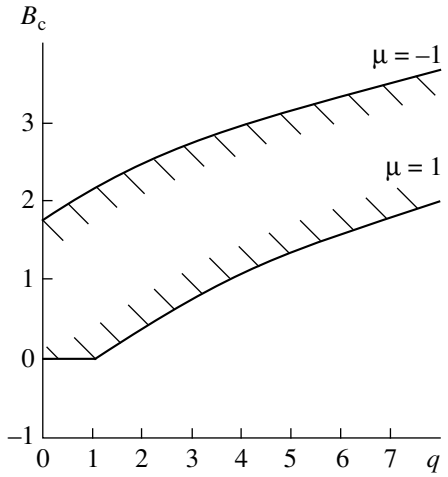


**Fig. 1.** The plot of critical values $B_c$ vs. $q$ for the lower ($\mu = 1$) or the higher ($\mu = -1$) cut-off frequency. The region of absolute instability is marked by hatching.

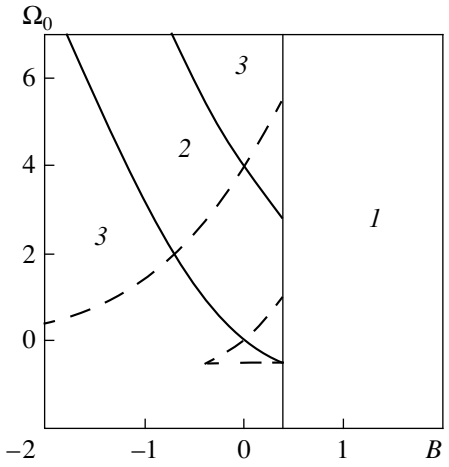


**Fig. 2.** The map of operation regimes ($B$, $\Omega_0$) for the lower cut-off frequency ($\mu = 1$) and $q = 2$: (*1*) absolute instability, (*2*) convective instability, and (*3*) transmission.

charge is favorable for oscillation near the higher limit, but it is unfavorable near the lower limit.

Alternatively, one may consider a perturbation that arises in a certain region and follows a preset time schedule. Then one deals with the problem of wave amplification by the medium (or convective instability) for the waves propagating from a source of given frequency $\Omega_0$ [1]. Look at the regions into which the parameter space ($B$, $\Omega_0$, $q$) is divided according to the regimes of operation (amplification or transmission). If the system is free from absolute instability, the boundaries can be determined from the following equations: $\Omega_0 = \Omega(\beta)$ and $d\Omega/d\beta = 0$ [2, 3]. For dispersion relationship (2), this yields

$$\begin{aligned} \Omega_0 &= \mu\beta^2 + \frac{1}{(\beta + B)^2 - q} = 0, \\ \mu\beta &- \frac{B + \beta}{[(B + \beta)^2 - q]^2} = 0. \end{aligned} \tag{4}$$

Note that lines (4) separate the regions where the imaginary part of each root of $\Omega_0 = \Omega(\beta)$ retains its sign. For each of the regions, the behavior of the system can be determined on the basis of the criterion distinguishing convective instability and opacity [1] at a single characteristic point.

The maps of ($B$, $\Omega_0$) corresponding to the solutions of various types were calculated for the lower and higher cut-off frequencies with $q$ ranging from 0 to 10. The case of the lower frequency and $q = 2$ is presented in Fig. 2. The chart comprises the regions of (*1*) absolute instability, (*2*) convective instability, and (*3*) transmission. The curves separating regions with different types of solution (namely, the amplification and transmission regions) and the dashed curves refer to resonance, when $\Omega_0 = \Omega_s$ with $\Omega_s = \Omega(\beta_s)$ being a frequency at which the roots of (2) merge with each other. It can be shown that the region $\Omega_0 < 0$ is a transmission region, by analogy with the propagation of a beam in a nonzero-susceptance medium. Specifically, the current wavenumbers are $\beta \approx -B \pm \sqrt{q - 1/(B^2 + |\Omega|)}$, provided that $|\Omega| \gg 1$. Under the above assumptions, the wavenumbers are real so that the system is transparent. Thus, perturbations are propagated by space-charge waves in the electron stream.

We are grateful to D.I. Trubetskov for his support.

This study was funded by the Russian Foundation for Basic Research, grant no. 97-02-16546.

## REFERENCES

1. E. M. Lifshitz and L. P. Pitaevskiĭ, *Physical Kinetics* (Nauka, Moscow, 1979; Pergamon Press, Oxford, 1981).
2. A. P. Kuznetsov and S. P. Kuznetsov, Izv. Vyssh. Uchebn. Zaved. Radiofiz. **23**, 1104 (1980).
3. S. P. Kuznetsov, E. Mosekilde, G. Dewel, *et al.*, J. Chem. Phys. **106**, 7609 (1997).

*Translated by A. A. Sharshakov*

*Technical Physics Letters, Vol. 26, No. 5, 2000, pp. 420–422. Translated from Pis'ma v Zhurnal Tekhnicheskoĭ Fiziki, Vol. 26, No. 10, 2000, pp. 40–45.*


# The Effect of Ultrasound on the Parameters of Metal–Dielectric–Semiconductor Structures

**P. B. Parchinskiĭ, S. I. Vlasov, R. A. Muminov, Kh. Kh. Ismailov, and U. T. Turgunov**

*Tashkent State University, Tashkent, Uzbekistan*

*Starodubtsev Physicotechnical Institute, Academy of Sciences of Uzbekistan, Tashkent, Uzbekistan*

Received December 7, 1999

**Abstract**—Data on the effect of ultrasound on the metal–oxide–semiconductor structures preliminary irradiated by γ-quanta are presented. It is demonstrated that the ultrasonic action results in a decrease of the radiation-induced charge in the dielectric layer of the structures under study. The observed effects are explained using a mechanism of the ultrasound-stimulated diffusion of radiation defects in the field of elastic stresses in the layer of silicon dioxide. © *2000 MAIK "Nauka/Interperiodica".*

It is known that the action of the radiation on the semiconductor devices results in the formation of various bulk defects and degradation of their electrophysical parameters [1]. Recent discovery of the positive influence of the ultrasonic processing on the defect structure of semiconductor materials [2, 3] explains the interest in the studies of the effect of ultrasound on the semiconductor devices and structures that experienced the action of ionizing radiation. In this work, we report on the effect of ultrasonic processing on the metal–oxide–semiconductor (MOS) structures preliminary irradiated by γ-quanta.

MOS structures were produced by means of the thermal oxidation of silicon with the specific resistance $\rho_0 = 0.2$–$0.5\ \Omega$ cm and the crystallographic orientation (100). Oxidation was performed in the atmosphere of dry oxygen at $T = 900$°C during one hour with subsequent slow cooling (10°C/min). A control electrode with the area $S = 4 \times 10^{-2}$ cm$^2$ and the ohmic contact were formed by the vacuum deposition of aluminum. The samples were irradiated by γ-quanta from a $Co^{60}$ source to a dose of $10^6$ rad and then treated for 30 min with ultrasound at a frequency of 1 MHz and a power of 1 W/cm$^2$.

It is commonly accepted that the process of charge accumulation in the dielectric and increase in the density of surface states (SS) at the Si–$SiO_2$ interface are factors producing the main influence on the parameters of MOS structures irradiated to closes below $10^7$ rad [4]. We used the method of high-frequency capacitance–voltage (*C–V*) characteristics [5] to determine the charge in the dielectric and the SS charge at the Si–$SiO_2$ interface. Figure 1 shows the experimental *C–V* curves of the MOS structures studied. It is seen that the ultrasonic treatment shifts the *C–V* curves of the irradiated structures along the voltage axis toward the parameters of the initial structures and changes the slope of the curves. According to [5, 6] this indicates a decrease both in the charge built in the dielectric layer and the SS charge. Figure 2 demonstrates a change of the integral SS charge ($Q_s$) along the band gap ($E_c - E$) of silicon. It is seen that the ultrasonic processing of the irradiated structures results in the decrease of $Q_s$ down to $1.5$–$2 \times 10^{-8}$ C/cm$^2$ at $E_c - E = 0.7$ eV. At the same time, the

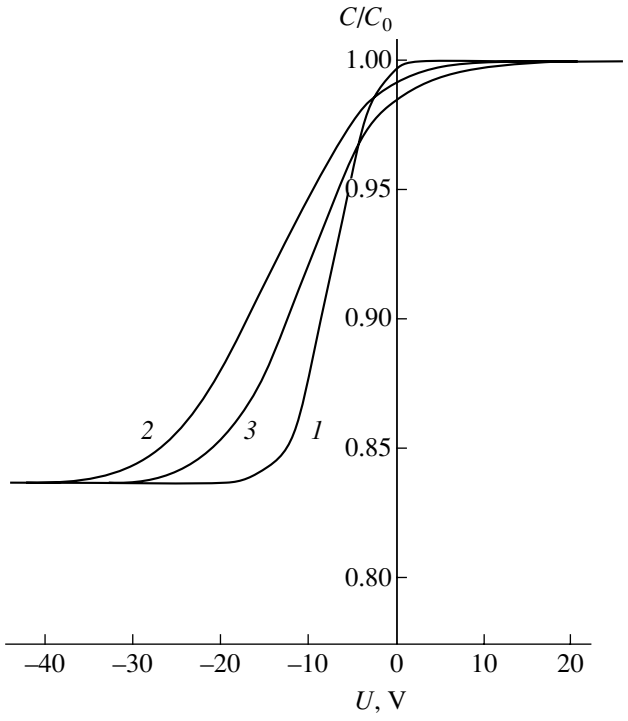


**Fig. 1.** Experimental capacitance–voltage (*C–V*) curves of the MOS structures: (*1*) initial structure, (*2*) the result of γ-irradiation; (*3*) the result of the ultrasonic action on the irradiated structure.

1063-7850/00/2605-0420$20.00 © 2000 MAIK "Nauka/Interperiodica"

ultrasonic treatment decreases the value of the effective charge inside the dielectric $Q_{ef}$ (determined from the shift of the *C–V* curves in the same energy interval [5, 7]) by $3.5–4 \times 10^{-8}$ C/cm$^2$.

It is known that high-intensity electric fields appear inside a dielectric in the course of the *C–V* measurements. In the structures under study, the electric field intensity in the dielectric layer was $E_d = 10^5$ V/cm. Such fields can stimulate the process of self-annealing of the radiation defects and relaxation of the radiation-induced charge in the dielectric layer [8]. However, control measurements of the irradiated structures not treated by ultrasound demonstrated the absence of the distinct changes of $Q_{ef}$ and $Q_s$. Hence, it can be concluded that the observed changes are caused by the ultrasonic treatment, rather than by the self-annealing of the radiation defects in the course of *C–V* measurements. At the same time, it was demonstrated that the ultrasonic processing of the initial (unirradiated) MOS structures does not lead to changes in the *C–V* curves and does not influence the process of accumulation of the radiation-induced charge in the dielectric layer. Therefore, the energy of the ultrasonic oscillations transferred to the MOS structures is lower than the threshold energy of the defect formation in $SiO_2$ and in the transition layer near the Si–$SiO_2$ interface.

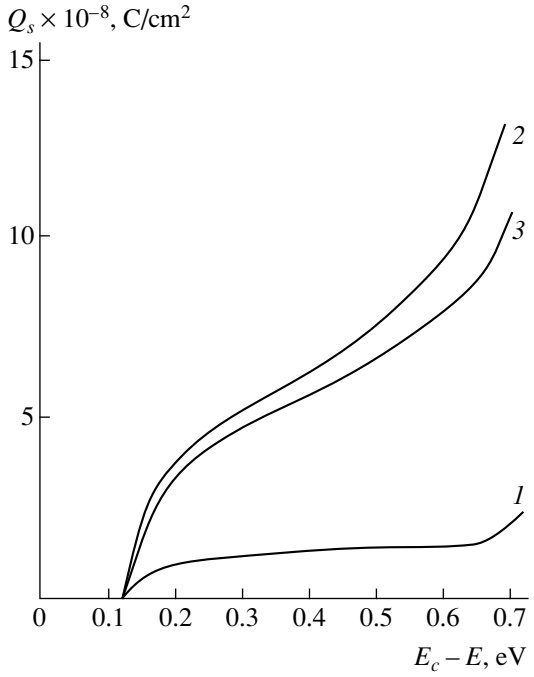


**Fig. 2.** The distribution of the integral charge of the surface states over the band gap of silicon in the MOS structures: (*1*) initial structure; (*2*) the result of γ-irradiation; (*3*) the result of the ultrasonic action on the irradiated structure.

These results can be explained as follows. It is known that the ionization effects play the main role in the formation of defects at the Si–$SiO_2$ interface and in the bulk of silicon dioxide under the action of γ-radiation [9]. In this case, two processes take place: the formation of the new charged defects and charging of the existing trap centers. Radiation defects in $SiO_2$ can be stable or unstable. In the former case, the positions of defects inside the glass structure are determined by the absolute minimum of the free energy. In the latter case, these positions correspond to a local minimum of the free energy [9]. It is known that there are internal compressive stresses in the transition layer near the Si–$SiO_2$ interface, which become weaker in the bulk of the dielectric layer [4, 8]. The ultrasonic action can stimulate diffusion of the unstable defects inside the glass structure with their further localization in the positions with an absolute minima of the free energy [10]. The gradient of the internal stresses causes a diffusion of the defects from the interface into the depth of the dielectric. The quantity $Q_{ef}$ that causes shifts of the *C–V* curves along the voltage axis is given by the formula

$$Q_{ef} = d^{-1}\int_0^d (\rho(x)x)dx, \qquad (1)$$

where $d$ is the thickness of the dielectric layer, $\rho(x)$ is the space charge distribution function inside the dielectric layer, ($x = 0$ at the metal–$SiO_2$ interface) [7]. Removal of the charged defects from the interface results in a shift of the maximum of $\rho(x)$ deeper inside the dielectric and a decrease of $Q_{ef}$. In addition, the removal of a part of defects from the interface makes impossible their recharging by electrons from bulk silicon, which results in the observed decrease of $Q_s$. Note also that the drift of defects can be accompanied by the process of their annihilation at the internal sinks and rearrangement of their energy levels [8], which can be followed by the liberation of the localized charge (this factor also leads to the decrease of $Q_{ef}$).

Therefore, the decrease of the radiation-induced charge observed in the dielectric layer of the MOS structures after ultasonic processing can be determined by the process of the ultrasound-stimulated diffusion of unstable radiation defects in field of elastic stresses in $SiO_2$ structure. The processes that take place in this case provide a partial recovery of the electrophysical parameters of the γ-irradiated MOS structures.

## REFERENCES

1. F. P. Korshunov, Yu. V. Bogatyrev, and V. A. Vavilov, *Effect of Radiation on Integrated Circuits* (Nauka i Tekhnika, Minsk, 1986).
2. E. Yu. Braĭlovskiĭ, A. P. Zdebskiĭ, V. L. Korchnaya, *et al.*, Pis'ma Zh. Tekh. Fiz. **13**, 1310 (1987) [Sov. Tech. Phys. Lett. **13**, 547 (1987)].

3. A. P. Zdebskiĭ, V. L. Korchnaya, T. V. Tarchinskaya, *et al.*, Pis'ma Zh. Tekh. Fiz. **12**, 76 (1986) [Sov. Tech. Phys. Lett. **12**, 31 (1986)].
4. V. S. Vavilov, M. Gorin, N. S. Danilin, *et al.*, *Radiation Methods in Solid-State Electronics* (Radio i Svyaz', Moscow, 1990).
5. S. Sze, *Physics of Semiconductor Devices* (Wiley, New York, 1981; Mir, Moscow, 1984).
6. L. M. Terman, Solid-State Elektron., No. 5, 803 (1962).
7. Yu. V. Chistov and V. F. Synorov, *The Physics of MOS Structures* (Voronezh. Gos. Univ., Voronezh, 1989).
8. V. S. Pershenkov, V. D. Popov, and A. V. Shal'nov, *Surface Radiation-Induced Effects in Integrated Circuits* (Énergoatomizdat, Moscow, 1998).
9. T. M. Agakhanyan, E. R. Astvatsatur'yan, and P. K. Skorobogatov, *Radiation-Induced Effects in Integrated Circuits* (Énergoatomizdat, Moscow, 1989).
10. P. I. Baranskiĭ, A. E. Belyaev, S. M. Koshirenko, *et al.*, Fiz. Tverd. Tela (Leningrad) **32**, 2159 (1990) [Sov. Phys. Solid State **32**, 1257 (1990)].

*Translated by A. Chikishev*

*Technical Physics Letters, Vol. 26, No. 5, 2000, pp. 423–425. Translated from Pis'ma v Zhurnal Tekhnicheskoĭ Fiziki, Vol. 26, No. 10, 2000, pp. 46–52.*


# Multilayer Structures with Quantum Dots in the InAs/GaAs System Emitting at a Wavelength of 1.3 μm

**G. É. Tsyrlin, N. K. Polyakov, V. A. Egorov, V. N. Petrov, B. V. Volovik, D. S. Sizov, A. F. Tsatsul'nikov, and V. M. Ustinov**

*Institute of Analytical Instrument Engineering, Russian Academy of Sciences, St. Petersburg, 198103 Russia*
*Ioffe Physicotechnical Institute, Russian Academy of Sciences, St. Petersburg, 194021 Russia*

Received January 18, 2000

**Abstract**—The optical properties of multilayer structures with quantum dots in the heteroepitaxial InAs/GaAs system have been studied. The structures were obtained by the method of submonolayer migration-stimulated epitaxy. It is shown that the optimized growth conditions provide room-temperature luminescence at a wavelength of 1.3 μm. *© 2000 MAIK "Nauka/Interperiodica".*

The creation of laser diodes emitting at a wavelength of 1.3 μm is very important for optical fiber communications. In recent years, much attention has been given to systems that can be regarded as an alternative to indium-phosphide-based lasers, which use the substrates and materials that cannot provide for the necessary temperature stability of lasing characteristics [1]. To obtain the emission at a 1.3 μm wavelength, several approaches were proposed and implemented. One of these is based on the use of InGaAsN quantum wells (QWs) with a low nitrogen content in the active region [2]; another one is based on the incorporation of InAs quantum dots (QDs) into a silicon matrix [3]. Still another approach consists in growing quantum dots in a heteroepitaxial (In,Ga)As/GaAs system by the Stransky–Krastanov mechanism providing considerable shift of the emission wavelength in comparison to that in the (InGa)As/GaAs quantum wells (QWs). In the latter case, the emission at a wavelength of about 1.3 μm can be achieved by several methods: (a) the formation of InGaAs/GaAs quantum dots by deposition of a rather large number (about eleven) of InGaAs monolayers of a 50%-(In,Ga)As solid solution by the method of molecular beam epitaxy (MBE) with alternating deposition of indium and gallium atoms and antimony molecules for increasing the lateral dimensions of nanoislands [4]; (b) the incorporation of InAs quantum dots obtained by the conventional MBE method into an external (Al,In,Ga)As quantum well [5, 6], which stimulates the decomposition of the solid solution and increases indium concentration in the vicinity of the quantum dot. Difficulties encountered in the attempts at achieving the 1.3 μm range in the structures with InGaAs/GaAs quantum dots are associated mainly with a rather large average thickness of the InAs layer in the active region, which results in a high probability of the formation of misfit dislocations. Therefore, the search for new approaches in designing devices based on the use of quantum dots emitting at a wavelength of 1.3 μm by minimizing the indium concentration in the active region seems to be quite timely.

It is well known that the use of submonolayer migration-stimulated epitaxy and/or its combination with other growth methods increases the lateral dimensions of nanometer islands in the InAs/GaAs system [7, 8]. For multilayer InAs/GaAs structures with several planes of InAs quantum dots separated by GaAs spacers, the average island dimensions are also rather large [9]. Below, we consider the optical properties of multilayer structures, where the quantum dots in the active regions were formed either by the method of submonolayer migration-stimulated epitaxy (SMSE) or by a combination of this method with the conventional MBE process. Optimization of the growth conditions made it possible to obtain structures with the room-temperature photoluminescence (PL) maximum at a wavelength of 1.3 μm and the average thickness of the InAs layer in each quantum-dot plane equal to 2.5 monolayers (MLs).

The structures studied were grown by the MBE method or, in the case of an active layer, by the modified MBE method—SMSE, whereby indium and antimony were alternatively deposited onto the substrate surface (each indium deposition cycle providing the formation of an 0.5-ML-thick layer then exposed for 10 s to the As flux). The structures were grown in an ÉP1203 apparatus on semi-insulating GaAs(100) singular or vicinal substrates. The active region located between two 6 nm-thick GaAs layers consisted of ten InAs layers of quantum dots separated by 6–8-nm-thick GaAs spacers. The effective thickness of the InAs layer in various structures with quantum dots ranged from 2.5 to 3.0 monolayers. To avoid the transport of nonequilibrium carriers into the subsurface region and the substrate during the optical studies, the active region was bounded on both sides by the short-period

1063-7850/00/2605-0423$20.00 © 2000 MAIK "Nauka/Interperiodica"

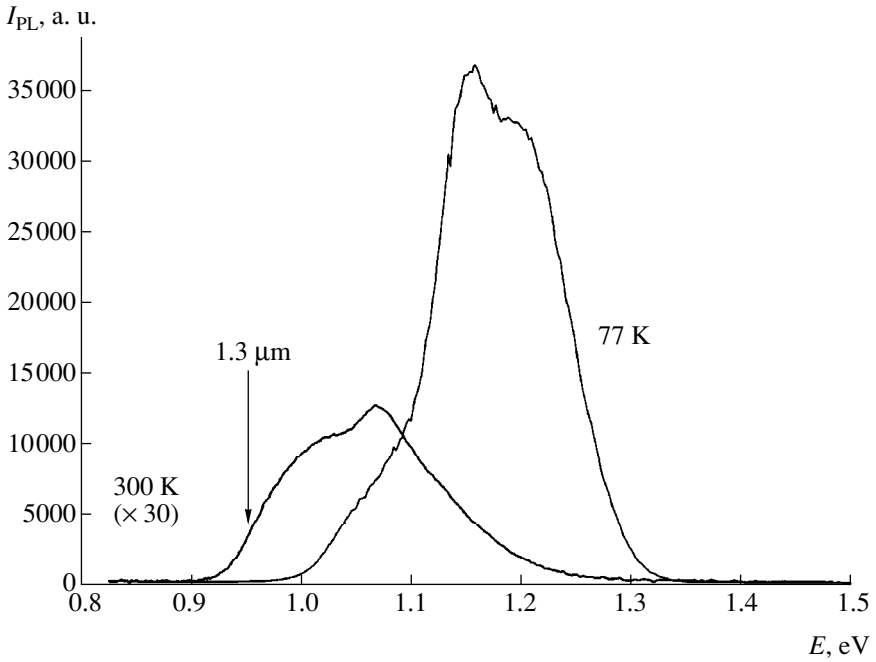


**Fig. 1.** Photoluminescence spectra measured at 77 and 300 K for a structure consisting of ten 2.5-ML-thick InAs layers of quantum dots grown by the SMSE method. The thickness of a GaAs spacer is 8 nm.

$Al_{0.25}Ga_{0.75}As$/GaAs superlattices (five 25A/25A pairs). The growth temperatures were 480°C for the active region and 550°C for the remaining part of the structure. The formation of quantum dots was checked by the reflection high-energy electron diffraction (RHEED) patterns. The growth rates (preliminarily measured for a calibrated sample using the method of intensity oscillation in the zeroth reflection of the RHEED pattern) were 0.10, 0.24, and 0.70 ML/s for InAs, AlAs, and GaAs, respectively. The total pressure of antimony vapors in the growth chamber measured by a VMB 1/8-type transducer was the same in all the experiments ($1.5 \times 10^{-6}$ Pa). Photoluminescence was excited by an $Ar^+$ laser ($\lambda = 514.5$ nm, the excitation energy density ~100 W/cm$^2$). Luminescence was detected by a cooled Ge-photodiode.

Figure 1 shows the photoluminescence spectra measured at 77 and 300 K for a sample with the active region consisting of ten InAs quantum-dot layers of the nominal thickness 2.5 ML grown by the SMSE method (five cycles) separated by 8-nm-thick GaAs spacers. The spectra are characterized by broadened lines (characteristic of the ensembles of quantum dots) with the maxima at ~1.2 and ~1.05 eV at 77 and 300 K, respectively. It is seen that only the long-wavelength edge of the fluorescence line covers the range of 1.3 μm at room temperature. The spectra obtained led to a conclusion that, in this case, the nanoisland dimensions were rather small, which could be explained either by a partial reevaporation of indium atoms during the first deposition cycle performed by the SMSE method (which resulted in a considerable decrease of the nominal thickness of the InAs layer) or by the pronounced migration of adatoms during rather long (10 s) pauses between the cycles of indium deposition.

To elucidate the situation, we grew a series of multilayer structures with modified growth parameters. An increase of the InAs content in each of the quantum-dot layers up to three monolayers resulted in the shift of the fluorescence maximum toward the long-wavelength range. However, this shift was accompanied by a drastic decrease of the photoluminescence yield in comparison with that observed for the previous structure. Thus, in this case, the island dimensions exceeded the critical volume of the formation of misfit dislocations, which resulted in a rather poor crystallographic quality of the structure.

A quite different situation was observed for a multilayer structure, in which a 0.5-ML-thick InAs layer was deposited by the MBE method, whereas all the other deposition cycles were performed by the SMSE method (altogether 2.5 InAs monolayers in each quantum-dot layer). Figure 2 shows the photoluminescence spectra for the singular and vicinal (7° misorientation along the [010] and $[0\bar{1}1]$ directions) samples measured at 77 and 300 K. The spectra of photoluminescence at 77 K are characterized by peaks in the region of 1.0–1.2 eV and exhibit a characteristic shift toward the short-wavelength range for the vicinal samples [10].

The coexistence of several peaks in the above spectra may be caused by several factors, including the existence of several groups of quantum dots of different dimensions, the possible formation of ensembles of quantum dots in the upper layers because of the lateral

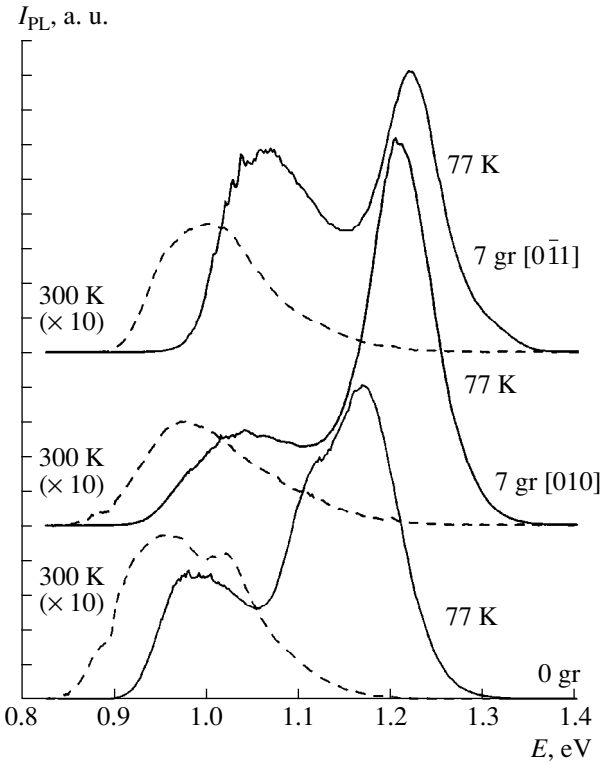


**Fig. 2.** Photoluminescence spectra measured at 77 and 300 K for the structures consisting of 2.5 ML-thick quantum-dot InAs layers grown by the combined MBE + SMSE method [0.5 ML (MBE) + 2.0 ML (SMSE)] on the singular and vicinal (7° misorientation along the [010] and [0$\bar{1}$1] directions) substrates. The thickness of a GaAs spacer is 8 nm.

merging of neighboring quantum dots [11], or by the contribution of photoluminescence of the excited states of quantum dots, which is confirmed by a change in the spectrum shape at lower excitation levels. The room-temperature photoluminescence peak for a singular sample is located at 1.3 μm; the maxima for the vicinal samples are located at 1.20–1.25 μm, which is also consistent with the photoluminescence data obtained at 77 K. A relatively small decrease of the emission intensity (by a factor of 10 to 20) upon the transition from 77 to 300 K indicates a rather high quality of the structures grown on both singular and vicinal substrates.

The computer simulation data [12] show that evolution of the island dimensions can proceed according to the following scenarios: (a) a decrease in the density with simultaneous increase in the island dimensions in the upper layers, (b) nucleation of new islands in the upper layers, (c) preservation of the island density in various layers depending on the mutual location of the islands in the initial layer and in the spacer bulk. The variation in the optical properties of the structures grown confirms the critical influence of the growth parameters and the amount of deposited InAs on the evolution of the system of quantum dots in the multilayer structures.

Thus, we have shown that the use of the multilayer structure of quantum dots in the heteroepitaxial InAs/GaAs system as an active region provides for the emission at a wavelength of 1.3 μm at room temperature. The quantum-dot layers were obtained by a combination of the MBE and SMSE methods (the nominal thickness of each layer was 2.5 ML). The study performed has proved a considerable effect of the growth parameters and the surface kinetic processes on the optical properties of the structures grown. The geometric and optical properties of such multilayer structures will be compared in a special publication.

## ACKNOWLEDGMENTS

The authors are grateful to Yu.B. Samsonenko, D.N. Demidov, and N.P. Korneeva for their help in growth experiments and to N.N. Ledentsov and A.E. Zhukov for fruitful discussions.

The study was supported by the State Scientific Program “Physics of Solid-State Nanostructures” (projects nos. 98-2029 and 99-2014) and the Russian Foundation for Basic Research (project no. 98-02-18317).

## REFERENCES

1. S. Seki, H. Oohasi, H. Sugiura, *et al.*, J. Appl. Phys. **79**, 2192 (1996).
2. M. Kondow, K. Uomi, A. Niwa, *et al.*, Jpn. J. Appl. Phys. **35**, 1273 (1996).
3. G. E. Cirlin, V. G. Dubrovskiĭ, V. N. Petrov, *et al.*, Semicond. Sci. Technol. **13**, 1262 (1998).
4. D. L. Huffaker, G. Park, Z. Zou, *et al.*, Appl. Phys. Lett. **73**, 2564 (1998).
5. B. V. Volovik, A. F. Tsatsul’nikov, D. A. Bedarev, *et al.*, Fiz. Tekh. Poluprovodn. (St. Petersburg) **33**, 990 (1999) [Semiconductors **33**, 901 (1999)].
6. A. R. Kovsh, A. E. Zhukov, N. A. Maleev, *et al.*, Fiz. Tekh. Poluprovodn. (St. Petersburg) **33**, 1020 (1999) [Semiconductors **33**, 929 (1999)].
7. G. É. Tsyrlin, A. O. Golubok, S. Ya. Tipisev, *et al.*, Fiz. Tekh. Poluprovodn. (St. Petersburg) **29**, 1697 (1995).
8. G. E. Cirlin, V. N. Petrov, and A. O. Golubok, Surf. Sci. **377–379**, 895 (1997).
9. G. M. Gur’yanov, V. N. Demidov, N. P. Korneeva, *et al.*, Zh. Tekh. Fiz. **67**, 111 (1997) [Tech. Phys. **42**, 956 (1997)].
10. V. G. Talalaev, B. V. Novikov, S. Yu. Verbin, *et al.*, Fiz. Tekh. Poluprovodn. (St. Petersburg) **34**, 467 (2000) [Semiconductors **34**, 453 (2000)].
11. A. F. Tsatsul’nikov, A. Yu. Egorov, A. E. Zhukov, *et al.*, Fiz. Tekh. Poluprovodn. (St. Petersburg) **31**, 851 (1997) [Semiconductors **31**, 722 (1997)].
12. V. A. Egorov and G. É. Tsyrlin, Pis’ma Zh. Tekh. Fiz. **26**, 86 (2000) [Tech. Phys. Lett. **26**, 220 (2000)].

*Translated by L. Man*

*Technical Physics Letters, Vol. 26, No. 5, 2000, pp. 426–428. Translated from Pis'ma v Zhurnal Tekhnicheskoĭ Fiziki, Vol. 26, No. 10, 2000, pp. 53–59.*


# Thermographic Investigation of the Discrete Fusion and Crystallization Supercooling of Lead

**V. I. Petrenko, F. V. Nedopekin, and P. V. Petrenko**

*Donetsk State University, Donetsk, Ukraine*

Received December 7, 1999

**Abstract**—The kinetics of lead melting and solidification were studied by the method of ballistic thermal analysis (BTA). It was established for the first time that the melting process involves three stages of fusion at $T_{L1}$, $T_{L2}$, and $T_{L3}$, with the temperature differences $T_{L2} - T_{L1} = 0.3 \pm 0.05$ K and $T_{L3} - T_{L2} = 0.6 \pm 0.1$ K. The corresponding specific enthalpies of fusion are $H_1 = H_2 = (0.4 \pm 0.05)H$ and $H_3 = (0.15 \pm 0.05)H$, where $H = H_1 + H_2 + H_3$. Crystallization always proceeds at a temperature equal to that of the first stage of fusion ($T_s - T_{L1}$). Accordingly, the crystallization supercooling of the melt exhibits discrete variation: $\Delta T_1^- = 0$, $\Delta T_2^- = 0.06 \pm 0.02$ K, and $\Delta T_3^- = 3 \pm 0.5$ K after the first, second, and third stage, respectively. Overheating of the melt to $\Delta T^+ = 22 \pm 2$ K is accompanied by the maximum supercooling $\Delta T_4^- = 4 \pm 0.2$ K. © *2000 MAIK "Nauka/Interperiodica".*

In practice, almost all substances exhibit various anomalies in their physical and mechanical properties in the vicinity of their melting temperatures, which are inherent in the nature of these substances, rather than brought about by impurities and technological factors [1]. There is a special direction of investigations called the physics of smeared phase transitions [2]. It is now commonly accepted that the melting process also proceeds within a certain interval of temperatures rather than at a single "melting point".

It was reported that various substances exhibit a discrete character of fusion [3–7]. For example, the melting of gallium single crystals involves four stages of fusion with the temperature differences 0.024, 0.0054, and 0.036 K [8]. However, no estimates were reported for the specific enthalpies of fusion of the separate stages of such melting processes, even when their multistage nature was established with certainty. Nor were any experimental data presented or theoretical hypotheses formulated concerning the temperature of crystallization in the systems with multistage fusion.

Another point of discussion is a possible effect of the temperature of melt overheating ($\Delta T^+$) and the discrete character of fusion on the values of crystallization supercooling $\Delta T^-$ [9].

All this indicates that real melting and solidification processes are much more complicated than their existing theoretical models. Therefore, new experimental methods should be developed and new experimental data obtained in order to formulate a new general theoretical model of melting and solidification. Before proceeding to investigations of the behavior of complex and multicomponent systems, we have to formulate clear concepts concerning processes occurring in simple compounds and single-component substances, the more so that many of such substances are used in a pure form or serve a base for various materials.

An example of widely spread substances of this kind is offered by lead (Pb). There are very few data on the kinetics of melting and solidification of this metal, but is was reported that various physical and mechanical characteristics of lead exhibited anomalous changes in the region of temperatures corresponding to transitions to the liquid ($T_L$) and solid ($T_S$) state. This is probably explained by the fact that the "anomalous" temperature region is rather narrow and the values of crystallization supercooling are small.

Below we report on the results of investigation of the melting and solidification kinetics of Pb by the method of ballistic thermal analysis (BTA) described in [3–6]. The experiments were performed using Pb samples of various purity grades, from technical to analytical. The samples of lead weighing 1–2 g were melted in alundum crucibles with a diameter of 7 mm and a height of 10 mm. The BTA diagrams were measured in air, and recorded at a chart velocity of 240 and 2400 mm/h. The temperature was determined with the aid of chromel–alumel and chromel–constantan thermocouples connected to a KSP-4 electronic potentiometer–recorder with a voltage scale of 20 or 1 mV (for the preliminary and precise measurements, respectively). A compensation potentiometer PPTV-1 connected in parallel to the thermocouples allowed the sample fusion temperatures to be measured in the middle of the recorder scale.

The sample heating and cooling was performed in a linear temperature variation mode with equal velocities of 0.0015–0.008 K/s. Each sample was measured under

1063-7850/00/2605-0426$20.00 © 2000 MAIK "Nauka/Interperiodica"

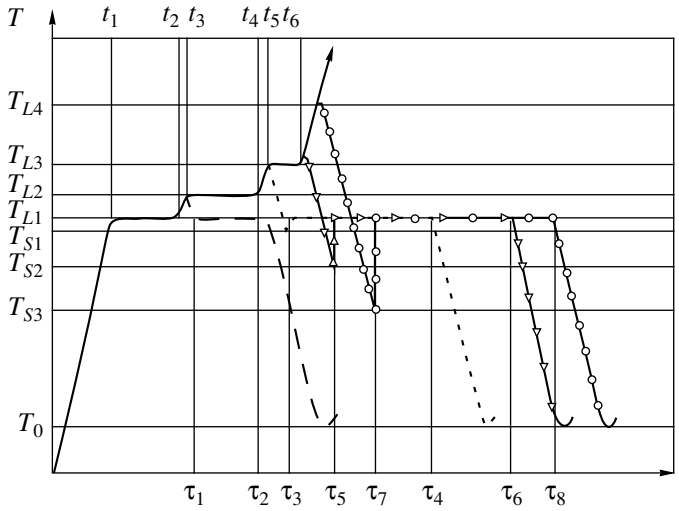


**Figure.**

identical conditions in several tens of thermal cycles, after which the results were processed and generalized BTA diagrams were constructed (see figure). In the first series of experiments, the BTA curves were recorded on a Pb sample overheated and supercooled within 50–100 K above and below the melting temperature, respectively, using a 20-mV potentiometer–recorder. In the second series, the thermograms were measured in a narrow range of $T_L = 324 \pm 12$ K and recorded with a 1-mV instrument. A generalized BTA diagram depicted in the figure shows the characteristic temperatures obtained by statistical averaging.

It was established for the first time that the melting process involves three stages of fusion at $T_{L1}$, $T_{L2}$, and $T_{L3}$, with the temperature differences between stages $T_{L2} - T_{L1} = 0.3 \pm 0.05$ K and $T_{L3} - T_{L2} = 0.6 \pm 0.1$ K.

After the first stage of fusion, whereby the metal is heated to $T_{L1} \le T \le T_{L2}$, the sample exhibits equilibrium crystallization without supercooling ($\Delta T_1^- = 0$. Upon the second stage of fusion at $T_{L2} \le T \le T_{L3}$, the process of solidification proceeds at a very low supercooling of $\Delta T_2^- = 0.06 \pm 0.02$ K. Upon fusion in the third stage at $T_{L3} \le T \le T_{L4}$, the crystallization supercooling increases in a jumplike manner to $\Delta T_3^- = 3 \pm 0.5$ K.

Upon heating the sample to elevated temperatures, with an overheating to about $\Delta T^+ = T_{L4} - T_{L3} = 20 \pm 2$ K, the melt apparently features some additional structural changes, as evidenced by the crystallization supercooling increasing in a jumplike manner again to reach $\Delta T_4^- = 4 \pm 0.2$ K. The BTA diagrams exhibited no endothermal effects in this temperature region, although a weakly pronounced nonlinearity was observed. A further increase in $\Delta T^+$ was not accompanied by changes in $\Delta T^-$. The onset of solidification in a supercooled melt always exhibited an explosion-like character. The discrete (rather than continuous) variation of $\Delta T^-$ with $\Delta T^+$ observed in Pb was also reported for other substances [3–7]. It was found that a supercooled Pb solution at $T \ge T_s - \Delta T_4^-$ may occur in the liquid state for an arbitrary long time, so that this state cannot be considered as metastable.

The above results indicate that processes involved in the melting– solidification cycle in Pb has a hysteresis character, similarly to changes in many other physical characteristics of substances in the region of phase transitions [1, 2].

X-ray diffraction measurements performed in the melts of many substances in the temperature intervals significantly above their melting temperatures revealed structural changes not observed by thermoanalytical methods [12, 13]. Nevertheless, these structural changes in the melts are known to significantly influence the kinetics of solidification and the values of crystallization supercooling $\Delta T^-$ [12].

By measuring the duration of melting and solidification processes (the length of horizontal plateaus), it is possible to determine (provided equal rates of heating and cooling) relative changes in the enthalpies of fusion at each stage and the corresponding enthalpies of solidification upon each fusion stage. As seen in the figure, the time of fusion in the first stage ($t_2 - t_1$) was equal to the corresponding time of solidification ($\tau_2 - \tau_1$). Durations of the first and second fusion stages were approximately the same ($t_2 - t_1 = t_4 - t_3$), but the time of solidification upon the second fusion stage was equal to the total time of fusion in the first two stages: $\tau_4 - \tau_3 = (t_2 - t_1) + (t_4 - t_3)$. The time of fusion in the third stage ($t_6 - t_5$) did not exceed half that in the first or second stage: $t_4 - t_3 \cong 2(t_6 - t_5)$. The time of solidification upon the third fusion stage was equal to the total time of fusion in the all three stages: $\tau_6 - \tau_5 = (t_2 - t_1) + (t_4 -$

$t_3$) + ($t_6 - t_5$). As the degree of melt overheating was increased further, the duration of solidification remained unchanged ($\tau_6 - \tau_5 = \tau_8 - \tau_7$). Relative values of the corresponding specific enthalpies of fusion were $H_1 = H_2 = (0.4 \pm 0.05)H$ and $H_3 = (0.15 \pm 0.05)H$, where $H = H_1 + H_2 + H_3$.

It was reliably established for the first time that solidification of the melt upon any crystallization supercooling always proceeds at a temperature equal to the temperature in the first stage: $T_S \equiv T_{L1}$.

In the BTA diagrams, the process of fusion is usually smeared over a certain temperature interval. This is explained by the fact that, in the course of continuous heating, the sample inevitably features considerable temperature gradients. Therefore, there are different temperatures at various points, while the thermocouple provides a value averaged over certain volume. In the course of BTA measurements, a maximum temperature of heating in each subsequent cycle is determined to within a few tenths of a degree and the temperature gradients at the extremal points are equal to zero. This circumstance allowed the discrete character of fusion to be established with confidence and the crystallization temperature to be determined with high precision. Based on the results of BTA measurements in Pb and some other substances [3–7], we may ascertain that the scatter of experimental $\Delta T^{-}$ values is related to a random arrangement of the primary crystallization centers on the sample surface (upon every fusion stage) relative to the thermocouple junction even at $\Delta T^{-} = \text{const}$.

The discrete character of fusion and jumplike variation of the crystallization supercooling cannot be explained from the standpoint of conventional molecular models of liquid involving spherically-symmetric interactions and classical motions (which do not at all feature "solidification" as such [14]). It was repeatedly suggested that a "pulsation" character of the crystallization mechanism is a principal property inherent in the liquid–solid phase transition [1, 15].

In the solid state, the bond energies in a crystal lattice are different along various axes and their rupture must take place at different temperatures. There were numerous attempts to explain the observed phenomena from the standpoint of quantum physics, considering "solidification as a jumplike transition into a quantum state" [14, 15], but no consistent theoretical concepts have been developed.

The possibility of a "pulsation" mechanism of crystallization "occurring at a hurricane rate" was originally suggested as long ago as in 1915 by academician B.S. Fedorov [16].

In closing, it should be noted that numerous experimental data reported in literature on the kinetics of melting and solidification indicate that the existing molecular-diffusion theories of nucleation and crystallization do not adequately reflect real physical processes. Therefore, new approaches have to be developed to rationalize these data.

## REFERENCES

1. A. R. Ubbelohde, *Melting and Crystal Structure* (Clarendon Press, Oxford, 1965; Mir, Moscow, 1969).
2. B. N. Rolov and V. É. Yurkevich, *Physics of Smeared Phase Transitions* (Rostov. Gos. Univ., Rostov, 1983).
3. V. D. Aleksandrov, A. Yu. Kudzin, and V. I. Petrenko, Pis'ma Zh. Tekh. Fiz. **13**, 1120 (1987) [Sov. Tech. Phys. Lett. **13**, 467 (1987)].
4. V. D. Aleksandrov and V. I. Petrenko, Rasplavy **2**, 29 (1988).
5. V. D. Aleksandrov and V. I. Petrenko, Rasplavy, No. 3, 83 (1992).
6. V. D. Alesandrov and V. I. Petrenko, Rasplavy, No. 4, 85 (1993).
7. V. D. Aleksandrov and V. I. Petrenko, Pis'ma Zh. Tekh. Fiz. **9**, 1354 (1983) [Sov. Tech. Phys. Lett. **9**, 582 (1983)].
8. *Properties of Elements: A Reference Book*, Ed. by M. E. Drifts (Metallurgiya, Moscow, 1985).
9. V. D. Aleksandrov and A. A. Barannikov, Pis'ma Zh. Tekh. Fiz. **24**, 73 (1998) [Tech. Phys. Lett. **24**, 573 (1998)].
10. A. A. Romanov, N. A. Vatolin, and V. V. Ryabov, Rasplavy, No. 1, 3 (1997).
11. B. P. Drapkin and V. K. Kononenko, Izv. Akad. Nauk SSSR, No. 5, 87 (1985).
12. V. I. Psarev and L. A. Ivanov, Izv. Vyssh. Uchebn. Zaved., Fiz. **8**, 31 (1982).
13. O. I. Ostrovskiĭ and V. A. Grigoryan, Izv. Vyssh. Uchebn. Zaved., Chern. Metall. **5**, 1 (1985).
14. V. V. Pavlov, Rasplavy, No. 4, 88 (1995).
15. B. Chalmers, *Principles of Solidification* (Wiley, New York, 1964; Mir, Moscow, 1968).
16. E. S. Fedorov, Priroda **XII**, 1461 (1915).

*Translated by P. Pozdeev*

*Technical Physics Letters, Vol. 26, No. 5, 2000, pp. 429–431. Translated from Pis'ma v Zhurnal Tekhnicheskoĭ Fiziki, Vol. 26, No. 10, 2000, pp. 60–65.*


# Defect Formation in a Two-Layer Al/Ni Crystal Bombarded with Ions Having Energies Close to the Sputtering Threshold

**G. V. Kornich[1], G. Betz[2], and A. I. Bazhin[3]**

[1] *Zaporozhskiĭ State Technical University, Zaporozh'e, Ukraine*

[2] *Institut für Allgemeine Physik, Technische Universität Wien, A-140 Wien, Austria*

[3] *Donetsk State University, Donetsk, Ukraine*

Received December 17, 1999

**Abstract**—Atomic collision cascades developed in an Al/Ni system, comprising a monolayer of Al atoms on the Ni(100) single crystal face bombarded at normal incidence by 25- or 50-eV Ar and Xe atoms, were simulated by means of molecular dynamics. It is shown that the number of Al atoms relocated within the first layer of the Al/Ni crystal markedly exceeds the number of analogous relocations in a nickel single crystal, which is explained by differences in the number of vacancies in the first layer of two systems, and in the lattice constants of Al and Ni. © *2000 MAIK "Nauka/Interperiodica"*.

In this work, we have compared the results of molecular dynamics simulation of the process of defect formation in (i) a two-layer crystal comprising a monolayer of Al atoms on the Ni(100) single crystal surface and (ii) a Ni single crystal with the same surface orientation bombarded at 300 K by 25- and 50-eV Ar and Xe atoms at a normal incidence.

The modeling was performed for the nickel and Al/Ni crystals containing 4032 and 3944 atoms, respectively, both systems comprising 14 atomic layers. In the Al/Ni crystal, two rows of Al atoms obeying periodic boundary conditions were excluded along the perimeter of the uppermost atomic layer in order to avoid nonphysical reconstruction of the Al monolayer [2]. In the two-layer structure studied, Al atoms in the surface layer repeated the lattice order of the Ni(100) substrate (in the absence of interactions with incident ions). Interactions between atoms in the crystals were described in terms of a many-body potential [3] matched at high energies with the ZBL potential [4], the latter used to describe the ion–atom collisions as well. The ambient temperature was modeled by a boundary layer on the side and rear surfaces of the crystal, which had a constant (room) temperature and absorbed the energy delivered with incident ions [5]. The interstitial atoms and vacancies generated by the ion bombardment were determined using an algorithm proposed in [6]. The initial coordinates of ions striking the target surface within a given elementary region [7] were calculated based on the law of random numbers. All simulations involved 200 collision cascades. Each cascade was traced in the initial crystal during 4 ps.

Tables 1 and 2 present data on the numbers (averaged over all the experimental runs) of the surface ($N_{v,s}$) and volume ($N_{v,v}$) vacancies, interstitial atoms ($N_{in}$), radiation-induced adatoms ($N_{ad}$), and atoms leaving their Wigner–Seitz (WS) cells ($N_{WS}$) for the Al/Ni and Ni crystals after a 4-ps collision cascade evolution. In Table 1, values in the numerator and denominator refer to the Al monolayer and the Ni substrate of the Al/Ni crystal, respectively. As seen from these data, the number of atoms ($N_{WS}$) relocated in the substrate of the Al/Ni system differs only slightly from that in the Ni crystal. At the same time, the number of relocations of Al atoms in the surface layer of the former system is, provided the same bombardment conditions, 2–6 times that in the uppermost layer of the Ni crystal, depending on the projectile type and energy. Determined using the $N_{ad}$ and $N_{WS}$ values presented in Table 1 and taking into account the results of our model calculations (not reported in this paper) for the number of Al atoms relocated into bulk of the Al/Ni crystal, the number of Al

**Table 1.** Average numbers of point defects per cascade formed in a two-layer Al/Ni crystal

| Al/Ni | | $N_{WS}$ | $N_{v,s}$ | $N_{v,v}$ | $N_{in}$ | $N_{ad}$ |
|---|---|---|---|---|---|---|
| Ar | 25 eV | 2.15/0.34 | 1.02 | 0.0 | 0.0 | 0.95/0.0 |
| | 50 eV | 8.59/3.14 | 2.57 | 0.02 | 0.025/0.06 | 2.19/0.01 |
| Xe | 25 eV | 2.47/0.6 | 1.06 | 0.01 | 0.0 | 0.95/0.0 |
| | 50 eV | 10.6/3.37 | 3.04 | 0.06 | 0.005/0.015 | 2.89/0.025 |

1063-7850/00/2605-0429$20.00 © 2000 MAIK "Nauka/Interperiodica"

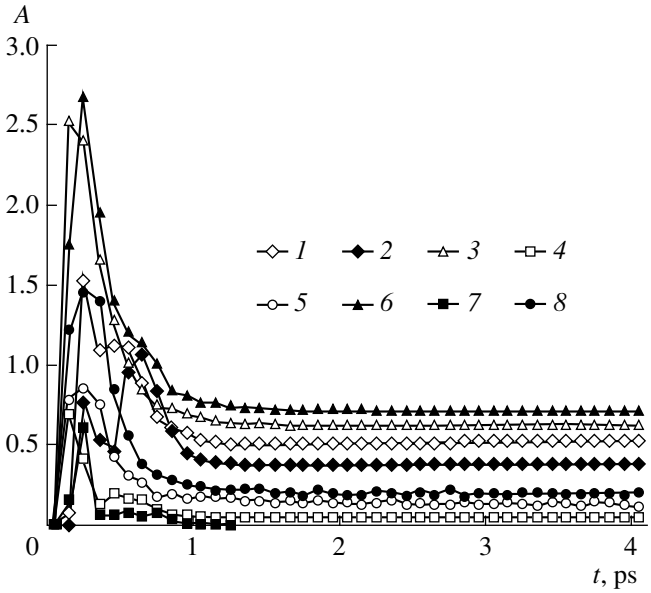


**Fig. 1.** Variation of the number *A* of various defects with time during the cascade development (averaged) in a Ni single crystal bombarded with 50-eV Ar (*1*, *3*, *4*, *5*) and Xe (*2*, *6*, *7*, *8*) atoms: (*1*, *2*) radiation-induced adatoms; (*3*, *6*) surface vacancies; (*4*, *7*) bulk vacancies; (*5*, *8*) interstitial atoms.

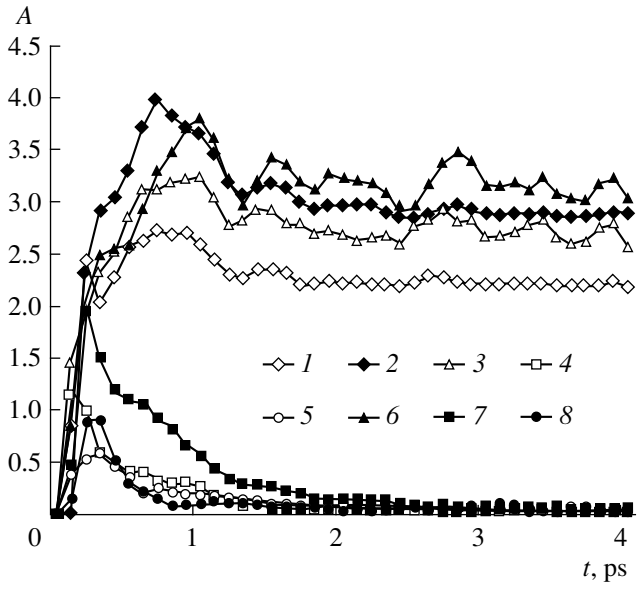


**Fig. 2.** Variation of the number *A* of various defects with time during the cascade development (averaged) in a two-layer Al/Ni crystal bombarded with 50-eV Ar (*1*, *3*, *4*, *5*) and Xe (*2*, *6*, *7*, *8*) atoms: (*1*, *2*) radiation-induced adatoms; (*3*, *6*) surface vacancies in the Al monolayer; (*4*, *7*) bulk vacancies in the Ni substrate; (*5*, *8*) interstitial Ni atoms.

atoms displaced out of their WS cells along the surface (i.e., not passing into the substrate or adlayer) was 0.91 or 5.25 (1.02 or 6.2) relocations per ion for the bombardment with Ar (Xe) ions with the primary energy 25 and 50 eV, respectively. The data of Table 2 indicate that the number of analogous lateral relocations in the uppermost layer of Ni atoms is several times lower, since the total number of relocations $N_{WS}$ is comparatively small.

As seen, the type of bombarding ions rather insignificantly affected the number of lateral relocations of Al atoms in the surface layer of the Al/Ni crystal, because the work required for these displacements is determined primarily by the number of surface vacancies weakly dependent (see Table 1) on the ion type. Study of the surface of the model Al/Ni crystal upon decay of the collision cascade revealed the following pattern: the region where a projectile struck the first atomic layer exhibited local atomic rearrangement involving a considerable number of atoms. This reconstruction, caused by a significant difference of the lattice constants of aluminum (4.05 Å) and nickel (3.52 Å), becomes possible due to a free room of 1–3 surface vacancies per cascade formed by the incident ion. Note that the edge rows of Al atoms on the periphery of the first atomic layers remained unchanged. No such effect was took place in the Ni crystal, as confirmed by the small $N_{WS}$ and $N_{v,s}$ values in Table 2.

**Table 2.** Average numbers of point defects per cascade formed in a Ni single crystal

| Ni | | $N_{WS}$ | $N_{v,s}$ | $N_{v,v}$ | $N_{in}$ | $N_{ad}$ |
|---|---|---|---|---|---|---|
| Ar | 25 eV | 0.39 | 0.13 | 0.0 | 0.0 | 0.13 |
| | 50 eV | 2.88 | 0.63 | 0.05 | 0.12 | 0.52 |
| Xe | 25 eV | 0.81 | 0.25 | 0.01 | 0.0 | 0.26 |
| | 50 eV | 3.32 | 0.71 | 0.0 | 0.21 | 0.48 |

The results of our model calculations of the atomic mean square displacements (MSDs) in the WS cells were also indicative of large lateral shifts of Al atoms in the first layer. For the Al/Ni crystal bombarded by Ar and Xe ions with an energy of 25 eV, the MSD values of Al atoms in the first layer were 5.3 and 5.4 Å$^2$, respectively, whereas the lateral shifts of Ni atoms in the (100) plane of the Ni crystal (adatoms not taken into account) bombarded at the same energy were 0.93 and 1.8 Å$^2$, respectively. The lateral displacements, as well as the corresponding $N_{WS}$ values, for the Ni crystal and the substrate layers of the Al/Ni system differ rather insignificantly. For the Ar and Xe ions with an energy of 50 eV, the MSD values of Al atoms in the first layer were 28.7 and 34.2 Å$^2$, whereas the lateral shifts of Ni atoms for the collision cascades in the Ni crystal (adatoms not taken into account) were 7.9 and 9.0 Å$^2$, respectively.

Figures 1 and 2 present data (averaged over all the experimental runs) describing variation of the number of various defects with the time of cascade development in Ni and Al/Ni crystals bombarded with 50-eV Ar and Xe ions. As is seen from these curves, the num-

ber of point defects of various types in the Ni crystal and in the substrate of the Al/Ni system decreases to less than half after the cascade evolution for 0.5–0.7 ps. At the same time, the numbers of surface vacancies and Al adatoms in the Al/Ni crystal (Fig. 2) reach maximum values within the first picosecond of the cascade evolution and decrease rather insignificantly during subsequent relaxation. Note that the surface vacancies in Al/Ni exhibit, irrespective of the ion type, a wavy instability after the first picosecond. This feature is evidence of a low-energy character of the process of Al atom passage near the initial lattice sites. Qualitatively similar patterns of the formation of Al adatoms and surface vacancies in Al/Ni were obtained for an ion energy of 25 eV.

A difference in the character of time variation of the number of surface defects during the cascade development in Al/Ni, on the one hand, and the behavior of bulk defects in the nickel substrate of this system, as well as the defects in the Ni single crystal, on the other hand, is also related to local changes in the atomic structure of Al monolayer in the Al/Ni crystal. This process is not accompanied by a development of the interatomic forces capable of returning the system to the pre-existing surface structure. Nor does it lead to the effective recombination of the surface vacancies and adatoms in the Al/Ni crystal.

The results of modeling also indicate that the number of interstitial atoms formed as a result of bombardment with 50-eV Ar ions is lower by a factor of 4–10 in the Al/Ni crystal than in the Ni single crystal. Apparently, the presence of a monolayer of Al atoms on the nickel substrate hinders the energy transfer into the bulk of the crystal, thus reducing the probability of the displacement collision sequence production–the main mechanism leading to the formation of sable interstitial atoms, and results predominantly in the compensated atomic relocations. In cases when bulk vacancies and interstitial Ni atoms were retained upon a 4-ps cascade evolution in the Ni or Al/Ni crystal, these defects were separated with respect to depth, occurring in the 2nd–3rd and 5th–10th layers, respectively. Interstitial Al atoms in the Al/Ni crystal after a 4-ps cascade evolution were observed only in the first two atomic layers.

## REFERENCES

1. J. M. Haile, *Molecular Dynamics Simulation–Elementary Methods* (Wiley-Interscience, New York, 1992).
2. G. V. Kornich, G. Betz, and A. I. Bazhin, Nucl. Instrum. Methods Phys. Res. B **153**, 383 (1999).
3. F. Gao, D. J. Bacon, and G. J. Ackland, Philos. Mag. A **67**, 275 (1993).
4. J. P. Biersack and J. F. Ziegler, Nucl. Instrum. Methods Phys. Res. B **141**, 93 (1982).
5. H. J. Berendsen, J. P. M. Postma, W. F. V. Gunsteren, *et al.*, J. Chem. Phys. **81**, 3684 (1984).
6. H. Gades and H. M. Urbassek, Phys. Rev. B **51**, 14559 (1995).
7. G. Betz, M. J. Pellin, J. W. Burnett, and D. M. Gruen, Nucl. Instrum. Methods Phys. Res. B **58**, 429 (1991).

*Translated by P. Pozdeev*

*Technical Physics Letters, Vol. 26, No. 5, 2000, pp. 432–435. Translated from Pis'ma v Zhurnal Tekhnicheskoĭ Fiziki, Vol. 26, No. 10, 2000, pp. 66–72.*


# Changes in the Topology and Symmetry of a Vorticity Field upon Turbulent Vortex Breakdown

**T. O. Murakhtina and V. L. Okulov**

*Institute of Thermal Physics, Siberian Division, Russian Academy of Sciences, Novosibirsk, Russia*

Received December 8, 1999

**Abstract**—A model describing a turbulent vortex breakdown in terms of the transition from right-handed helical slender vortex to left-handed annular vortex is proposed. The results offer a new approach to the phenomenon of vortex breakdown considered from the standpoint of spontaneous changes in the topology and symmetry of the vorticity field. © *2000 MAIK "Nauka/Interperiodica".*

The phenomenon of vortex breakdown was extensively studied in the case of swirling flows in tubes. The flows with the moderate Reynolds number (below 35000) exhibit well-known bubble, helix, and double-helix types of the breakdown [1]. Experiments with flows in the range of greater Reynolds numbers (100000—300000) [2, 3] revealed a new type of the turbulent vortex breakdown, whereby the flow behind the breakdown region comprises several helices rotating at a very high speed. For Re > 200000, the helices tend to contract and the breakdown pattern resembles an axisymmetric contour with hollow core. Analysis of a diagram of distribution of the azimuthal vorticity component, and of the velocity profiles measured in various cross-sections of the working region of the tube [3], indicate that the breakdown was preceded by the appearance of a circular columnar slender vortex transformed into an annular vortex (a ring vortex with hollow core). This implies that not only the vortex topology varies, which is characteristic of all the breakdown types previously known, but the vorticity field topology changes as well.

The purpose of this work was to study the possibility of describing this new form of vortex breakdown as the transition from right-handed helical slender vortex to left-handed annular vortex (Fig. 1b) by analogy with a description developed previously [4, 5] for the breakdown of other types, not involving changes in the vorticity field topology (Fig. 1a).

For a more accurate description of the average flow characteristics in the region behind the turbulent vortex breakdown, we will use a model of the annular helical vortex with a constant axial vorticity component distribution in the ring $r_0 - \varepsilon < r < r + \varepsilon$ [6] and generalize this model to the case of smooth distribution:

$$\omega_z = 2\Gamma\left[\frac{\varepsilon}{(\varepsilon^2 + (r - r_0)^2)}\right]^2,$$

$$f(r, \varepsilon, r_0) = \frac{r(r - r_0)}{(r - r_0)^2 + \varepsilon^2} \tag{1}$$

$$+ \frac{r_0}{\varepsilon}\arctan\left(\frac{r - r_0}{\varepsilon}\right) + \frac{r_0}{\varepsilon}\arctan\left(\frac{r_0}{\varepsilon}\right).$$

Integrating equation (1) restores the tangential and axial velocity profiles:

$$w_\varphi = \frac{\Gamma}{r}\left[\frac{r(r - r_0)}{(r - r_0)^2 + \varepsilon^2} + \frac{r_0}{\varepsilon}\arctan\left(\frac{r - r_0}{\varepsilon}\right)\right.$$

$$\left. + \frac{r_0}{\varepsilon}\arctan\left(\frac{r_0}{\varepsilon}\right)\right], \tag{2}$$

$$w_z = w_0 - \frac{r}{l}w_\varphi.$$

Figure 2 shows an approximation of the velocity

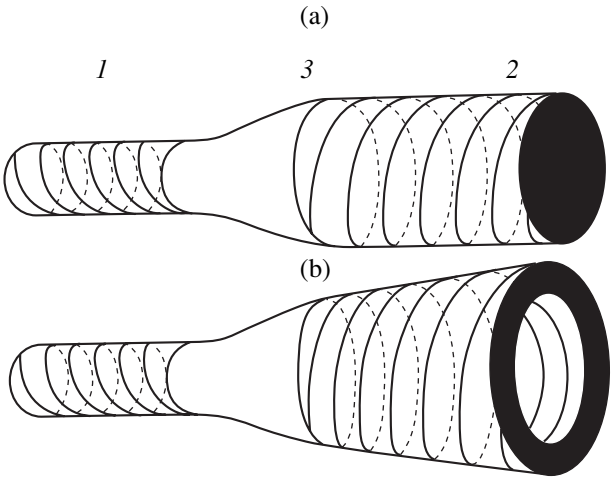


**Fig. 1.** Schematic diagrams illustrating the helical symmetry and topology of the vorticity field for breakdown of the (a) slender and (b) annular cone types: (*1*) left-hand vortex; (*2*) right-hand vortex; (*3*) breakdown region.

1063-7850/00/2605-0432$20.00 © 2000 MAIK "Nauka/Interperiodica"

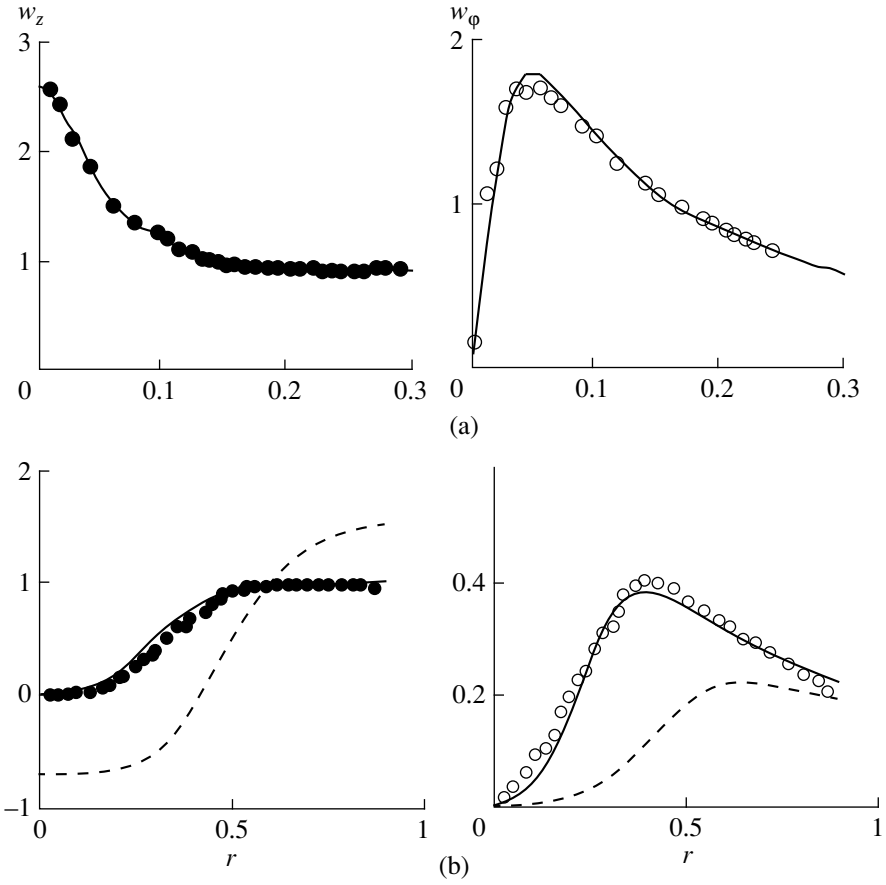


**Fig. 2.** Profiles of the axial and azimuthal velocity components (a) before and (b) after the breakdown at Re = 230000. Open and black circles show experimental data [2], solid curves represent the approximation by equations (2), and dashed curves are calculated by the conservation equations (3).

profiles measured in [3] by the curves calculated within the framework of a model described by equations (2) with the parameters listed in the table. Here, $\Gamma$ characterizes the vortex circulation, $r_0$ is the median radius of the ring layer of concentrated vorticity, $2\varepsilon$ is the width of this circular region, $2\pi l$ is the pitch of the vortex lines, $w_0$ and $p_0$ are the velocity and pressure at the axis, and $r$ is the current radius measured from the axis. As seen from this figure, the model agrees well with the averaged experimental velocities in the cross-sections at maximum distance from the reign of breakdown–despite the fact that equations (2) represent an exact solution to the Euler equations. As expected, the character of flow in front of the breakdown region is well described by the model of the slender vortex ($r_0 = 0$).

Following the approach developed in [4, 5], we will consider the possibility of vortex breakdown from the standpoint of existence of various vortex structures having the same integral characteristics of the flow:

(*flow rate*)

$$Q = 2\pi\rho\int_0^R w_z r\,dr$$

(*rate circulation*)

$$G = Rw_\varphi(R)$$

(*axial flux of momentum moment*)

$$L = 2\pi\rho\int_0^R w_\varphi w_z r^2\,dr$$

(*axial flux of momentum*)

$$J = 2\pi\rho\int_0^R\left(w_z^2 + \left(\int_0^r \frac{w_\varphi^2}{\sigma}d\sigma + \frac{p_0}{\rho}\right)\right)r\,dr \qquad (3)$$

(*axial flux of energy*)

$$E = 2\pi\rho\int_0^R\left(\frac{w_z^2 + w_\varphi^2}{2} + \left(\int_0^r \frac{w_\varphi^2}{\sigma}d\sigma + \frac{p_0}{\rho}\right)\right)w_z r\,dr.$$

Due to insufficient experimental data for evaluation of the energy losses for viscous effects and turbulent pulsations according to the conservation laws (3), the consideration below will be restricted to the case of ideal fluid. However, because the number of vortex parame-

Parameters of velocity profiles described by equations (2)

| Vortex structure parameters | | Γ | $w_0$ | $l$ | ε | $r_0$ | $p_0$ |
|---|---|---|---|---|---|---|---|
| Before breakdown | Approximation and calculation | 0.18 | 2.6 | 0.10* | 0.5 | 0 | 0 |
| After breakdown | Approximation | 0.05 | 0.02 | −0.20* | 0.19 | 0.24 | – |
| | Calculation | 0.03 | −0.69 | −0.08* | 0.24 | 0.44 | 5.46 |

Note: *Positive and negative $l$ values refer to the left- and right-hand helical vortex, respectively.

ters increased in comparison with that used previously [4, 5], even this simplification would require one more equation to be added to the conservation laws for $Q$, $G$, $L$, $J$, and $E$. This equation was derived by taking into account that the Bernoulli constant of the steady-state flow in a nonviscous fluid remains unchanged, both along the current lines (providing conservation of the axial energy flux component $E$) and along the vortex lines. Therefore, the additional characteristic is provided by the corresponding axial energy flux component

$$B = 2\pi\rho\int_0^R\left(\frac{w_\varphi^2 + w_z^2}{2} + \left(\int_0^r \frac{w_\varphi^2}{\sigma}d\sigma + \frac{p_0}{\rho}\right)\right)w_z r dr. \quad (4)$$

Thus, we have the necessary number of conservation laws and may solve the task of determining the possible vortex structure parameters for the same values of $Q$, $G$, $L$, $J$, $E$, and $B$. Substituting (1) and (2) into (3) and (4), we obtain a system of equations with respect to the vortex variables Γ, $l$, ε, $r_0$, $w_0$, and $p_0$. Expressing $w_0$, $l$, Γ, and $p_0$ explicitly as functions of ε and $r_0$,

$$w_0(\varepsilon, r_0) = \frac{Q\Gamma(\varepsilon, r_0)k2(\varepsilon, r_0) - Lk1(\varepsilon, r_0)}{\pi\Gamma(\varepsilon, r_0)(k2(\varepsilon, r_0) - k1(\varepsilon, r_0)^2)},$$

$$l(\varepsilon, r_0) = \pi\Gamma(\varepsilon, r_0)^2\frac{k2(\varepsilon, r_0) - k1(\varepsilon, r_0)^2}{L - Q\Gamma(\varepsilon, r_0)k1(\varepsilon)},$$

$$\Gamma(\varepsilon, r_0) = \frac{G}{k0(\varepsilon)},$$

$$p_0(\varepsilon, r_0) = \frac{J}{\pi} - \frac{1}{\pi}$$
$$\times\left[w_0(\varepsilon, r_0)Q + \frac{L}{l(\varepsilon, r_0)} + 2\pi\Gamma(\varepsilon, r_0)^2K1(\varepsilon, r_0)\right],$$

we reduce the initial system to two equations with respect to these parameters:

$$\begin{cases} w_0(\varepsilon, r_0)\left[J - \dfrac{w_0(\varepsilon, r_0)}{2}Q + \dfrac{\pi}{2}\dfrac{\Gamma(\varepsilon, r_0)^2}{l(\varepsilon, r_0)^2}k2(\varepsilon, r_0)\right. \\ \left. + \pi\Gamma(\varepsilon, r_0)^2k4(\varepsilon, r_0)\right] + \pi\dfrac{\Gamma(\varepsilon, r_0)}{l(\varepsilon, r_0)} \\ \times\left[p_0(\varepsilon, r_0)k1(\varepsilon, r_0) + \Gamma(\varepsilon, r_0)^2k5(\varepsilon, r_0)\right. \\ \left. + \dfrac{\Gamma(\varepsilon, r_0)^2}{2l(\varepsilon, r_0)^2}k3(\varepsilon, r_0) + 2\Gamma(\varepsilon, r_0)^2K2(\varepsilon, r_0)\right] = E, \\ 2\pi\Gamma(\varepsilon, r_0)\varepsilon^2\left[(w_0^2(\varepsilon, r_0) + 2p_0(\varepsilon, r_0))k6(\varepsilon, r_0)\right. \\ \left. + 2w_0(\varepsilon, r_0)\dfrac{\Gamma(\varepsilon, r_0)}{l(\varepsilon, r_0)}k7(\varepsilon, r_0) + \dfrac{\Gamma(\varepsilon, r_0)^2}{l(\varepsilon, r_0)^2}k8(\varepsilon, r_0)\right] \\ + 2\pi\Gamma(\varepsilon, r_0)\varepsilon^2[\Gamma(\varepsilon, r_0)^2(k9(\varepsilon, r_0) \\ + 2K3(\varepsilon, r_0))] = B. \end{cases} \quad (5)$$

Here

$$k0(\varepsilon, r_0) = f(1, \varepsilon, r_0);\ k1(\varepsilon, r_0) = 2\int_0^1 x f(x, \varepsilon, r_0)dx;$$

$$k2(\varepsilon, r_0) = 2\int_0^1 x f(x, \varepsilon, r_0)^2dx;$$

$$k3(\varepsilon, r_0) = 2\int_0^1 x f(x, \varepsilon, r_0)^3dx;$$

$$k4(\varepsilon, r_0) = \int_0^1 \frac{f(x, \varepsilon, r_0)^2}{x}dx;$$

$$k5(\varepsilon, r_0) = \int_0^1 \frac{f(x, \varepsilon, r_0)^3}{x} dx;$$

$$k6(\varepsilon, r_0) = \int_0^1 \frac{x}{[\varepsilon^2 + (x - r_0)^2]^2} dx;$$

$$k7(\varepsilon, r_0) = \int_0^1 \frac{x f(x, \varepsilon, r_0)}{[\varepsilon^2 + (x - r_0)^2]^2} dx;$$

$$k8(\varepsilon, r_0) = \int_0^1 \frac{x f(x, \varepsilon, r_0)^2}{[\varepsilon^2 + (x - r_0)^2]^2} dx;$$

$$k9(\varepsilon, r_0) = \int_0^1 \frac{f(x, \varepsilon, r_0)^2}{x[\varepsilon^2 + (x - r_0)^2]^2} dx;$$

$$K1(\varepsilon, r_0) = \int_0^1 xP(x, \varepsilon, r_0) dx;$$

$$K2(\varepsilon, r_0) = \int_0^1 xP(x, \varepsilon, r_0) f(x, \varepsilon, r_0) dx;$$

$$K3(\varepsilon, r_0) = \int_0^1 \frac{xP(x, \varepsilon, r_0)}{[\varepsilon^2 + (x - r_0)^2]^2} dx;$$

$$P(x, \varepsilon, r_0) = \int_0^x \frac{f(s, \varepsilon, r_0)^2}{s^3} ds,$$

and $f(r, \varepsilon, r_0)$ is the function determined by equation (1). By the quantities $\Gamma$, $l$, $\varepsilon$, and $r_0$ we imply their dimensionless combinations $(\Gamma/R)U$, $l/R$, $\varepsilon/R$, $r_0/R$, $w_0/U$, $(\rho_0/\rho)U^2$, where $R$ is the tube cross-section at the entrance of the working region, $U$ is the rate-average flow velocity in this cross-section, and $\rho$ is the fluid density. Dimensionless integrals $Q$, $G$, $L$, $J$, $E$, and $B$ are represented by the quantities $(Q/\rho)UR^2$, $(G/R)U$, $(L/\rho)U^2R^3$, $(J/\rho)U^2R^2$, $(E/\rho)U^3R^2$, and $(B/\rho)U^3R$.

Analysis of the system of equation (5) showed that there are two roots in the permissible variation range of the parameters $\varepsilon$ $(0 \le \varepsilon \le 1)$ and $r_0$ $(0 \le r_0 \le 1)$. The vortex parameters calculated for the first root coincide with the values before breakdown, and the second root corresponds to the structure after breakdown (see table). The calculated and experimental profiles of the axial and azimuthal velocity components are compared in Fig. 2. The results of the calculation show a satisfactory agreement with the experiment, taking into account that the model employed did not allow either for variations of the integral flow characteristics related to small changes of the tube geometry in the working region nor for the losses due to viscosity (friction) or turbulent pulsations.

Thus, we have established for the first time the presence of helical symmetry for the vorticity field in the flows featuring turbulent vortex breakdown. The new type of breakdown was modeled by the transition from a right-handed column-like helical slender vortex to the left-handed divergent annular vortex under conditions of fixed integral flow characteristics. The results of modeling qualitatively agree with experiment [2, 3] and confirm interpretation of the vortex breakdown [4] as a sudden mirror change in orientation of the helix lines forming a core of the vortex structure.

## REFERENCES

1. J. H. Faler and S. Leibovich, Phys. Fluids **20**, 1385 (1977).
2. T. Sarpkaya, Phys. Fluids **7**, 2301 (1995).
3. T. Sarpkaya and F. Novak, AIAA Pap. **99-0135**, 1 (1999).
4. V. L. Okulov, Pis'ma Zh. Tekh. Fiz. **22**, 47 (1996) [Tech. Phys. Lett. **22**, 798 (1996)].
5. V. L. Okulov, S. V. Alekseenko, J. Legrand, and P. Legentilhomme, Russ. J. Eng. Thermophys. **7** (3–4), 149 (1997).
6. S. V. Alekseenko, P. A. Kuibin, V. L. Okulov, and S. I. Shtork, J. Fluid Mech. **382**, 195 (1999).

*Translated by P. Pozdeev*

*Technical Physics Letters, Vol. 26, No. 5, 2000, pp. 436–438. Translated from Pis'ma v Zhurnal Tekhnicheskoĭ Fiziki, Vol. 26, No. 10, 2000, pp. 73–79.*


# Effect of Mechanical Activation on the Sintering of a Titanium–Nickel Alloy and a Bioceramic TiNi Composition

**V. I. Itin, O. G. Terekhova, T. E. Ul'yanova, V. A. Kostikova, N. A. Shevchenko, and D. V. Berdnikova**

*Siberian Physicotechnical Institute, Tomsk State University, Tomsk, Russia*
*Tomsk Branch, Institute of Structural Macrokinetics and Materials Science, Siberian Division, Russian Academy of Sciences, Tomsk, Russia*
Received August 12, 1999; in final form, December 7, 1999

**Abstract**—Mechanical activation strongly influences the sintering of pressed articles made of a powdered titanium–nickel alloy and its compositions with dental porcelain. Preliminary treatment of the powdered mixtures in a planetary ball mill suppresses the martensite transformation and removes anisotropy in the variation of linear dimensions of the pressings. The resulting samples exhibit, instead of a volume expansion related to the rupture of contacts between particles in the course of the reverse martensite transformation, a sintering-induced shrinkage whose extent increases with the sintering temperature and the duration of mechanical activation treatment. *© 2000 MAIK "Nauka/Interperiodica".*

Porous (permeable) materials and articles made of titanium–nickel (TiNi) alloys are now frequently used in medicine as materials replacing defects in human tissues, matrices for xenotransplantation, etc. [1]. These materials and articles are usually obtained by self-propagating high-temperature synthesis or by methods of powder metallurgy [1, 2].

However, the sintering of porous materials made of TiNi powders encounters certain problems related to a considerable volume expansion of pressings with increasing sintering temperature: the article volume increases on heating to 400°C, remains unchanged in the 400–1000°C interval, and begins to decrease only at 1100°C and above [3, 4]. Moreover, variation of the linear dimensions of cylindrical TiNi pressings upon sintering was characterized by a sharp anisotropy: an increase in the diameter of samples was several times smaller than a growth in their height. These features are explained by the reverse martensite transformation beginning at room temperature immediately upon the load release after pressing and continuing in the course of heating (sintering). As a result, the contacts between powder particles are broken in the course of an intensive volume increase. This behavior significantly complicates the obtaining of porous materials and articles with a preset shape for medical purposes.

As is known, a strong plastic deformation leading to the formation of submicrocrystalline or amorphous structure is capable of suppressing the martensite transformation in TiNi alloys [5, 6]. It was expected that the mechanical activation of these materials in high-energy apparatuses, resulting in a considerable plastic deformation of the TiNi powder particles, would also suppress the martensite transformation and lead to considerable shrinkage of the pressings.

In order to verify this hypothesis, we have studied the effect of mechanical activation on the sintering behavior of pressed articles made of a 45% Ti–55% Ni alloy powder (PN55T45 grade, TU 14-127-104-78 standard, Tulachermet Company, Tula, Russia) with a particle size of 10–45 μm and of a mixture of this material with dental porcelain (Gamma composition, TU 64-2-268-78 standard, Medical Polymer Plant, St. Petersburg, Russia).

The initial powders were mechanically activated by treatment in planetary ball mills of the MPV (water cooled; gasoline medium) and M-3 (air cooled; air atmosphere) types. Both mills have 1000 $cm^3$ steel drums filled with 0.3–0.4-cm-diam steel balls. The ball to powder weight ratio was 20 : 1. The effective energy stress factor was 12, 30, or 60 g in the MPV mill and 45 g in the M-3 mill. The activation treatment duration was varied within 1–30 min.

Pressings made of the mechanically activated powders had the shape of cylinders with a diameter of 7–8 mm, a height of 10–11 mm, and an initial porosity of 41–44%. For the comparison, control samples were made of the initial (nonactivated) powders. The pressings were mounted in the working chamber of an SNVE 1.3.1/16ICh furnace and sintered in a vacuum of $133 \times 10^{-4}$ Pa for 2 h at various temperatures in the 1000–1170°C interval.

Changes in the volume and linear dimensions of pressings upon sintering were characterized by the fol-

lowing parameters: $\frac{\Delta V}{V_0} = \frac{V_0 - V}{V_0}$; $\frac{\Delta h}{h_0} = \frac{h_0 - h}{h_0}$; $\frac{\Delta d}{d_0} = \frac{d_0 - d}{d_0}$, where $V_0$, $h_0$, and $d_0$ are the initial volume, height and diameter of samples and *V*, *h*, and *d* are the final values of these parameters. Positive and negative values of the parameters correspond to shrinkage and expansion of the pressings upon sintering, respectively.

The X-ray diffraction measurements were performed in a 10–110° range of angles on a DRON-3 diffractometer using filtered $CuK_\alpha$ radiation (accelerating voltage, 32 kV; anode current, 22 mA).

Sintering of the pressings made of a nonactivated TiNi powder led to a growth in the material porosity (see table). This resulted in increasing volume (18–20%), diameter (2–2.5%), and height (14–15%) of the cylindrical samples (see Figs. 1, 2, and the table). The sharply anisotropic change of the linear dimensions of sintered samples is related to a considerable expansion of the material in the direction of pressing.

As the effective energy stress factor increases, the volume expansion of samples pressed from a powder activated for a short time (0.5 or 1 min) decreases and changes to shrinkage (Fig. 1, curves *1* and *2*), while the samples made of powders treated for a sufficiently log time (10 and 15 min) exhibit shrinkage from the very beginning of sintering (Fig. 1, curves *3* and *4*). The extent of shrinkage continuously increases with the duration of mechanical activation and sintering temperature (see Figs. 1, 2, and the table). Moreover, the anisotropy in the change of linear dimensions also disappears, as indicated by the anisotropy factor $\frac{\Delta h}{h_0} / \frac{\Delta d}{d_0}$ approaching unity (table).

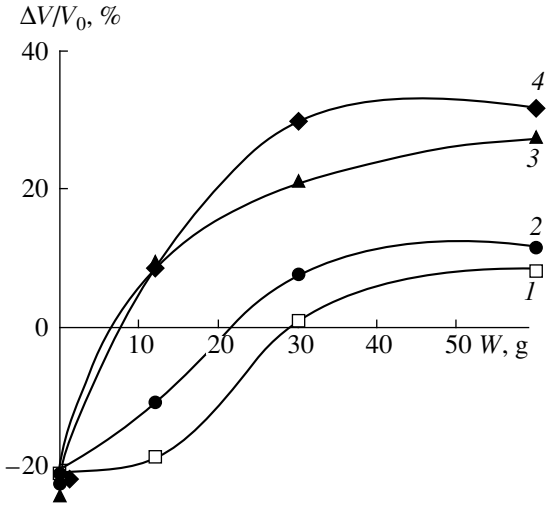


**Fig. 1.** Plots of the relative sample volume change $\Delta V/V_0$ upon a 2-h sintering at 1150°C versus effective energy stress factor *W* for the pressings of TiNi powder mechanically activated for (*1*) 0.5, (*2*) 1, (*3*) 10, and (*4*) 15 min.

Similar results were observed upon mechanical activation of a porcelain Gamma–50 wt % TiNi composition (table). In contrast to a considerable increase in porosity and linear dimensions of the initial (and the more so, of the activated) porcelain powder upon sintering, the samples made of the activated porcelain–TiNi composition exhibited considerable shrinkage at a virtually zero anisotropy of changes in the linear dimensions (table).

Effect of mechanical activation on the porosity and linear dimensions of samples pressed from a TiNi powder and a porcelain Gamma–50 wt % TiNi mixture

| Material | Sintering temperature, °C | Initial porosity, % | Final porosity, % | $\frac{\Delta h}{h_0}$, % | $\frac{\Delta d}{d_0}$, % | Anisotropy factor $\frac{\Delta h}{h_0} / \frac{\Delta d}{d_0}$ |
|---|---|---|---|---|---|---|
| TiNi (initial) | 1000 | 45 | 55 | –15 | –2.5 | 6.0 |
| | 1100 | 46 | 55.5 | –14.5 | –2.2 | 6.6 |
| | 1150 | 44 | 54 | –14 | –2 | 7.0 |
| TiNi (activated in gasoline at 60 g, 15 min) | 1000 | 45.1 | 42.7 | 1.4 | 1.6 | 0.9 |
| | 1100 | 45.2 | 41.2 | 2.0 | 2.6 | 0.8 |
| | 1150 | 44.8 | 19.5 | 11 | 12.4 | 0.9 |
| Gamma (initial) | 1000 | 41.1 | 59.2 | –21.4 | –7.8 | 2.7 |
| Gamma (activated at 45 g, 30 min) | 1000 | 39.5 | 77.9 | –47.7 | –33.6 | 1.4 |
| Gamma–50 wt % TiNi (activated at 45 g, 30 min) | 1000 | 35 | 13.5 | 9.3 | 9.8 | 0.95 |

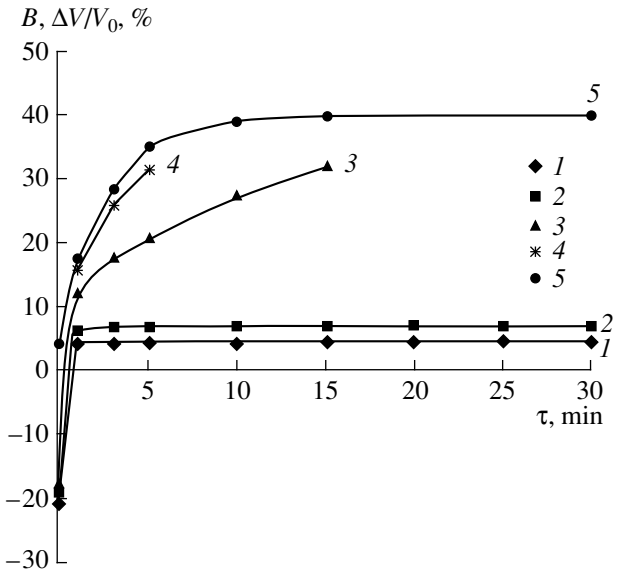


**Fig. 2.** Effect of the duration of mechanical activation τon the (110)B2 X-ray diffraction line width *B* (curve *5*) and the relative volume change $\Delta V/V_0$ of TiNi powder pressings sintered at (*1*) 1000, (*2*) 1100, (*3*) 1150, and (*4*) 1170°C.

Analysis of the X-ray diffraction patterns showed that increase in the duration of mechanical treatment was accompanied by increasing width of the lines of TiNi reflections (Fig. 2, curve *5*). For the large activation times, the X-ray diffraction profile broadening was so large that the lines raised only slightly above the background. A coarse estimate of the coherent scattering domain size by the Selyakov–Scherrer formula indicated that a 5–30-min mechanical treatment led to the formation of a submicroscopic structure with a crystallite size of about 25 nm. This estimate agrees quite well with the results reported in [7], where a 24-h treatment of a TiNi powder in a ball mill led to the structure with a crystallite size of 5–12 nm. Such a fine-crystalline structure is usually observed in the samples upon strong plastic deformation (exceeding 90%), which completely suppresses the martensite transformation.

Thus, it was established that the absence of reverse martensite transformation and a highly defective structure formed upon the mechanical treatment significantly activate the sintering process, provide considerable shrinkage of the pressings made of a TiNi alloy and a porcelain Gamma–50 wt % TiNi mixture, and fully eliminate anisotropy in the change of linear dimensions. This facilitates the obtaining of porous implants substituting damaged tissues with a preset shape, size, and porosity.

## REFERENCES

1. V. É. Gunter, V. I. Itin, L. A. Monasevich, *et al.*, *Shape Memory Effects and Their Application in Medicine* (Nauka, Novosibirsk, 1992).
2. V. I. Itin, V. É. Gunter, S. A. Shabalovskaya, and R. L. C. Sachdeva, Mater. Charact. **32**, 179 (1994).
3. V. V. Skorokhodov, S. M. Solonin, I. F. Martynova, *et al.*, Poroshkov. Metall., No. 4, 17 (1990).
4. N. A. Shevchenko and V. I. Itin, Poroshkov. Metall., Nos. 7/8, 31 (1998).
5. A. A. Klopotov, V. M. Kushnarenko, and Yu. A. Sazanov, Izv. Vyssh. Uchebn. Zaved., Fiz., No. 2, 3 (1992).
6. V. É. Gunter, T. Yu. Maletkina, and A. A. Klopotov, Pis'ma Zh. Tekh. Fiz. **22**, 7 (1996) [Tech. Phys. Lett. **22**, 999 (1996)].
7. E. Hellstern, H. J. Fecht, Z. Fu, and W. L. Johnson, J. Mater. Res. **4**, 1292 (1989).

*Translated by P. Pozdeev*

*Technical Physics Letters, Vol. 26, No. 5, 2000, pp. 439–442. Translated from Pis'ma v Zhurnal Tekhnicheskoĭ Fiziki, Vol. 26, No. 10, 2000, pp. 80–87.*


# Nonlinear Current–Voltage Characteristics of the Cross-Shaped Microstructures Based on Thin Bismuth Films

**A. I. Il'in, A. I. Aparshina, S. V. Dubonos, and B. N. Tolkunov**

*Institute of Microelectronic Technologies and Special-Purity Materials, Russian Academy of Sciences, Chernogolovka, Russia*

Received December 22, 1999

**Abstract**—The deposition of bismuth films under a residual gas pressure $10^{-6}$ Pa results in the "metal-type" variation of conductivity at low temperatures. Conductivity of the cross-shaped microstructures based on these films exhibits the properties analogues to those of the ballistic electron transport in 2D systems. © *2000 MAIK "Nauka/Interperiodica".*

Bismuth exhibits a long natural mean free path of electrons, which makes it a promising material for the investigation of quantum electric and magnetic phenomena. The de Haas–van Alphen and Shubnikov–de Haas effects, as well as the quantum effects in mesoscopic thin-film conductors, were discovered in bismuth [1]. However, in contrast to the samples made from thick crystals, bismuth films with a thickness of 20–100 nm exhibit considerable (sometimes severalfold) increase in resistance upon cooling from room temperature down to 4.2 K. Such films do not allow one to use the natural advantages of bismuth in nanostructures.

As is known, the mean free path of electrons in microstructures obtained under certain conditions can be as high as 1500 nm at 4.2–100 K [2, 3]. Microstructures involving metal and semimetal films with such long mean free paths of electrons are suitable for investigating ballistic transport and quantum electric phenomena. However, realizing this possibility necessitates the study of the electric conductivity of bismuth films obtained under different conditions. This situation is similar to that with the heterostructures based on $A_3B_5$ materials, where the long extensive complex studies of the mechanisms of growth and the relationships between the real structure and the electronic properties resulted in achieving the levels of electron mobility and electric conductivity close to the theoretically predicted ones. In this paper, we report on studies of the dependence of the electric resistance and current–voltage (*I–V*) characteristics of microstructures based on bismuth films on the conditions of film preparation in high vacuum and on the technology of production of the microstructures.

We used a commercially available VI-0000 bismuth (the content of bismuth being not less than 99.9999%) after degassing and remelting in vacuum at $10^{-8}$ Pa. Bismuth films with a thickness of 40–60 nm were produced by thermal evaporation in vacuum with various residual gas pressures ($10^{-6}$–$10^{-3}$ Pa) during the course of deposition at a rate of 1.5–3 nm/min. The films were deposited onto $SiO_2$ or $Si_3N_4$ surfaces on silicon that were preliminarily cleaned by oxygen plasma. The residual gas pressure before deposition was not worse than $10^{-8}$ Pa. In addition, the substrates were annealed at 200°C for 2 h in the same chamber under an ultrahigh vacuum prior to deposition of the sample structures through a mask. The temperature of annealing before deposition was 100°C when the microstructures were produced by the "lift off" electron lithography method. The widths of the working area of the microstructures produced by deposition through a mask and by the electron lithography were 300 and 0.2–2 μm, respectively. Each sample of the microstructures produced by means of lithography contained strips of different thickness for the comparative estimation of the influence of free surfaces on the electron transport. A digital voltmeter and a differential amplifier with an input resistance of $10^3$ Ω measured the electric resistance in the temperature interval 4.2–298 K at the current densities not exceeding $10^3$ A/cm$^2$.

In order to produce the samples for transmission electron microscopy (TEM), the substrates were subjected to one-side penetrating anisotropic etching until the formation of 100-nm-thick $SiO_2$ membranes on one side of the silicon plate. The structure of deposited films was studied by electron microscopy with the use of the bright- and dark-field images [4].

Figure 1 shows the results of measurements of the temperature dependence of the electric resistance of bismuth microstructures with a thickness of 25–100 nm. The samples were grown under different residual pressures of gases ($10^{-6}$–$10^{-3}$ Pa) in a chamber of the ultrahigh vacuum device by means of deposition

1063-7850/00/2605-0439$20.00 

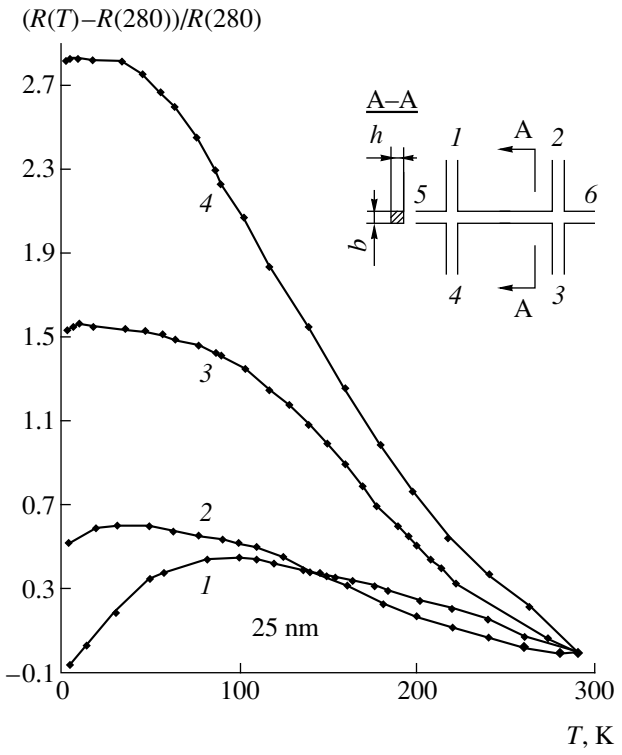


**Fig. 1.** Temperature dependence of the relative electric resistance in the structures of bismuth films with 300-μm width of the working part of the strip obtained by deposition through a mask onto a substrate heated to 80–100°C under different residual pressures of gases: (*1*) $10^{-6}$ Pa; $h$ = 25 nm; (*2*) $10^{-6}$ Pa, $h$ = 60 nm; (*3*) $10^{-4}$ Pa, $h$ = 60 nm; (*4*) $>10^{-3}$ Pa, $h$ = 60 nm. Inset shows a scheme of the sample: $h$ is the thickness of the film and $b$ is the width of the working part of the strip.

through a mask onto a substrate heated to 80–110°C. The electric resistance of the films grown at high residual gas pressure increases with decreasing temperature (Fig. 1, curve *4*), showing a temperature dependence of the activation type that is typical of semiconductors and dielectrics. A qualitatively similar dependence was obtained for the films grown under a pressure of $10^{-4}$ Pa (Fig. 1, curve *3*). The submicron films deposited under a higher vacuum (Fig. 1, curves *1* and *2*) exhibit nonmonotonic temperature dependence of the electric resistance. The decrease of the electric resistance at low temperatures was stronger for the films of lesser thicknesses (Fig. 1, curve *1*).

A similar temperature dependence of the electric resistance was also observed for bismuth films deposited onto acetate lacquer or mica [2]. In the latter case the deposition of bismuth onto the (00.1) crystallographic plane of mica leads to the formation of epitaxial films with the $(00.1)_{Bi}$ plane parallel to the substrate and a grain size of 3 μm. However, the decrease of the relative resistance was not as pronounced as in our experiments, presumably due to higher residual gas pressure in the deposition chamber (not less than $10^{-4}$ Pa). It is seen from Fig. 1 that a high vacuum is necessary for an increase in the electric conductivity. It is possible that the coincidence boundaries, at which the atoms belonging to both of the neighboring grains transfer the translation periodicity of the lattice almost without distortions, also contribute to the increase of the electric conductivity of thin films deposited on hot substrates [5]. It is possible that the adsorption of impurities is smaller at such interfaces than at the arbitrary boundaries of the so-called general type.

The phenomenon of the coarse-grained structure formation in the films is quite common. It takes place possibly due to a decrease in the energy of the film–substrate system. Indeed, a similar structure was observed in gold, silver, aluminum, and some other metals deposited onto the oxidized silicon [6, 7]. The grain boundaries, the free surface, and the film–substrate interface play an important role in the scattering of conduction electrons in the films. An idea of the structure of the bismuth films can be based on the general features typical of the formation of the films of metals such as gold, silver, and aluminum on $SiO_2$ substrates. The melting points of these metals are higher than that of bismuth and their structures degrade to a lower extent than that of bismuth when the sections for TEM are prepared. For example, the aluminum film with a thickness of 100 nm exhibits monocrystalline grains growing through the whole film and has neither peculiarities at the interface with a $SiO_2$ substrate nor roughnesses at the free surface [8]. It is possible that the same structure is typical of the section of a bismuth film with a grain size of 0.2–0.4 μm in the film plane.

We prepared several samples with the thicknesses of conducting strips 2, 0.5, 0.3, and 0.2 μm by means of electron lithography under the regimes providing for the obtaining of bismuth films with high conductivity at low temperatures. Estimates of the mean free path of electrons were obtained for these samples, after calculation of their resistivity ($r$) between crossings of the working strips (for example, contacts *1* and *2* in Fig. 1), with the use of the formula:

$$l = m^* v / n e^2 r, \qquad (1)$$

where $m^*$ is the effective mass of electron, $e$ is the charge of electron, $n$ is the concentration of charges, and $v$ is the mean velocity of electrons. This formula yields a value of 0.2 μm for the mean value of resistivity $r \sim 900$ μΩ cm (temperature dependence of $r$ corresponds to curve *3* in Fig. 1). The same estimation procedure applied to the best samples with $r \sim 200$ μΩ cm produced by deposition through a mask yields a value of about 1 μm (for the curve *2* or *1* in Fig. 1). Such a difference between resistivities of the samples produced by different methods is possible, as was mentioned earlier, due to the high sensitivity of the electric conductivity of bismuth films to the presence of impurities. The contamination is more likely in the case of a more complicated technology of manufacturing the

microstructures based on the electron lithography. This lithographic process introduces additional structural defects and impurities in comparison to the case when the microstructures are manufactured by deposition through a mask.

We measured the current–voltage characteristics in microstructures at the bridges between crossings of the conducting strips (see inset in Fig. 1, where *1–2* and *3–4* are the potential contacts and *5–6* are the current contacts) and also at the crossings, taking neighboring contacts as the potential ones and the opposite contacts as the current ones (e.g., *1–5* and *4–6* in Fig. 1) for all the neighboring ends of the crossing in turn. For the width of the conducting strips 300 and 2 μm at the crossings and also between them, the *I–V* curves were always linear to comply with the Ohm law $u = iR$, where $u$ is the voltage, $i$ is the electric current, and $R$ is the resistance of the microstructure. We calculated the values of the bending resistance $R$ for all the neighboring contacts based on the results of the *I–V* measurements at the crossings. Thus, four values of $R$ correspond to each crossing. If the potential contacts were used instead of the current ones for the symmetric crossing, the dispersion of the values of the bending resistance did not exceed 2–3% and coincided with the final accuracy of the measurements. The technology of manufacturing of the microstructures allows a certain spread of the widths of the working parts of the strips. That is why the measurements of 20–30 crossings with the strip width smaller than 2 μm showed that the strip width ranged from 0.17 to 0.7 μm. About half of the measurements were performed on the structures with golden contact areas, whereas the other measurements were carried out on the structures with chromium contacts providing a better adhesion of bismuth to chromium. At the temperature of liquid helium, about half of the microstructures exhibited nonlinear *I–V* characteristics regardless of the contact material. Curves *1* and *2* in Fig. 2a correspond to the microstructures measured at 4.2 and 77 K, respectively; the width of the working part of the strip is $b = 0.6$ μm. Figure 2b shows the maximum bending of the *I–V* curve for one of the structures at 4 K and $b = 0.2$ μm.

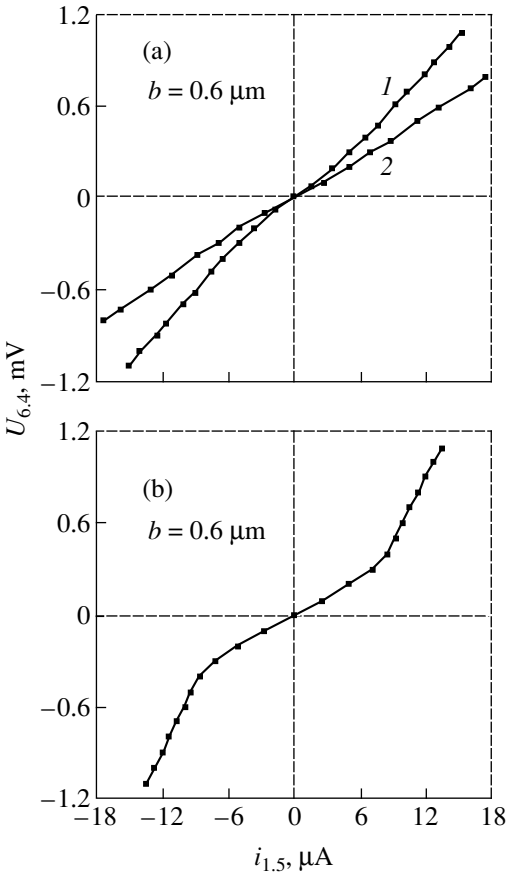


**Fig. 2.** The *I–V* curves of the microstructures with different widths of the conducting strips. Curve *1* in Fig. 2a and the curve in Fig. 2b were measured at 4.2 K; curve *2* in Fig. 2a was measured at 77 K.

It is obvious that the Ohm law does not explain a decrease of the slope of the *I–V* curves in the vicinity of zero (Fig. 2). Monocrystalline semiconductor heterostructures with a mean free path of electrons exceeding the size of the structure itself exhibit similar changes of their *I–V* curves characteristics [9]. The mean grain size in the bismuth films (0.2–0.4 μm) is comparable with the width of the working part of the strips of the cross-shaped structures. That is why the working part of the strip can be considered as consisting (in the transverse direction) of 1–2 monocrystals with different orientations relative to the substrate. Since the size of the monocrystalline segments is comparable with the strip width, the bending resistance must depend on the crystallographic orientation, size of the monocrystals, and the structure of interfaces between them. In the case of the ballistic transport of electrons through the cross-shaped intersection of the strips, the bending resistance is given by a formula that allows negative values of $R$ [9], which, however, was not the case in this work presumably because of the diffusion–ballistic rather than purely ballistic motion of electrons. A decrease of the *I–V* curve bending with temperature increasing to 77 K (Fig. 2a) also proves the diffusion–ballistic type of the electron transport. However, additional experiments on the determination of the density and mobility of the charge carriers are necessary for the complete understanding of nonlinearity of the *I–V* characteristics of bismuth films.

Therefore, the technology of bismuth deposition through a mask under ultrahigh vacuum conditions allows one to obtain the samples with the mean free path of electrons of 1 μm; use of the electron lithography makes it possible to produce the structures with a mean free path of 0.2–0.3 μm. The nonlinearity of the *I–V* curves in the cross-shaped microstructures of semimetallic bismuth result from the diffusion–ballistic motion of electrons.

## REFERENCES

1. V. T. Petrashov, Mikroélektronika **23**, 3 (1994).
2. Yu. F. Komnik, E. I. Bukhshtab, Yu. B. Nikitin, *et al.*, Zh. Éksp. Teor. Fiz. **60**, 669 (1971) [Sov. Phys. JETP **33**, 364 (1971)].
3. A. I. Il'in, A. B. Andreeva, and B. N. Tolkunov, J. Adv. Mater. **3**, 33 (1996).
4. S. S. Gorelik, L. N. Rastorguev, A. Yu. Skakov, in *X-Ray and Electron Diffraction Analysis of Metals* (Moscow, 1963), pp. 206–215.
5. A. I. Il'in and A. V. Andreeva, Fiz. Met. Metalloved. **80**, 132 (1995).
6. C. V. Thompson and J. E. Floro, J. Appl. Phys. **67**, 4099 (1990).
7. C. C. Wong, Y. I. Smith, and C. V. Thompson, Appl. Phys. Lett. **48**, 335 (1986).
8. A. I. Il'in, E. E. Glikman, V. V. Starkov, *et al.*, Poverkhnost' **4**, 77 (1991).
9. Y. Hirayama, T. Saku, S. Tarucha, *et al.*, Appl. Phys. Lett. **58**, 2672 (1991).

*Translated by A. Chikishev*

*Technical Physics Letters, Vol. 26, No. 5, 2000, pp. 443–445. Translated from Pis'ma v Zhurnal Tekhnicheskoĭ Fiziki, Vol. 26, No. 10, 2000, pp. 88–94.*


# Long-Wavelength Emission in InGaAsN/GaAs Heterostructures with Quantum Wells

**B. V. Volovik[1], A. R. Kovsh[1], W. Passenberg[2], H. Kuenzel[2], N. N. Ledentsov[1], and V. M. Ustinov[1]**

[1] *Ioffe Physicotechnical Institute, Russian Academy of Sciences, Politekhnicheskaya 26, St. Petersburg, 194021 Russia*

[2] *Heinrich Hertz-Institut für Nachrichtentechnik Berlin GmbH, Einsteinufer 37, 10587 Berlin, Germany*

Received January 18, 2000

**Abstract**—The properties of InGaAsN/GaAs heterostructures with quantum wells on GaAs substrates were studied. The GaAsN layers containing InGaAsN quantum wells with a high (exceeding 1%) nitrogen concentration were obtained. The long-wavelength emission in the InGaAsN quantum wells is obtained in the wavelength range up to 1.32 μm at room temperature. The effect of the InGaAsN quantum parameters on the optical properties of heterostructures is studied. © *2000 MAIK "Nauka/Interperiodica".*

Lasers emitting at a wavelength of about 1.3 μm are among the major components of optical-fiber communication systems. At present, these lasers are made with the use of heterostructures based on solid solutions in the InGaAsP or InGaAlAs systems on InP substrates. However, these devices have a number of disadvantages in comparison with the structures grown on GaAs substrates. First, the threshold current has a low temperature stability because of small band gaps in the conduction band [1] (the typical characteristic temperatures range within 50–80 K). Moreover, development of the surface emitting lasers is also complicated by the problems encountered in obtaining distributed Bragg reflectors with high reflection coefficients due to a small difference in the refractive indices of the constituent layers. Thus, the creation of lasers operating in the 1.3 μm range on GaAs substrates is one of the most pressing of modern microelectronics. The best results were obtained for the structures with InGaAs/GaAs quantum dots [2, 3] and the InGaAsN/GaAs structures [4–8]. It was shown that, because of a large value of the bowing parameter, the incorporation of nitrogen into (In)GaAs results in a considerable decrease of the bandgap width. Also, a GaAsN/GaAs layer experiences considerable tensile stresses, whereas the InGaAs/GaAs layers are subject to considerable compressive stresses, and, therefore, the incorporation of nitrogen compensates stresses in the InGaAsN/GaAs layer. A high temperature stability predicted theoretically for the threshold current in InGaAsN-based lasers is explained by a considerable discontinuity in the conduction band [4]. It is also possible to design vertically emitting lasers using the AlGaAs/GaAs distributed Bragg reflectors. At present, there are lasers emitting at a wavelength of 1.3 μm based on the InGaAsN/GaAs quantum wells [5, 6], which are characterized by low threshold current density and a high (2.7 W) output power in the continuous mode [6]. A high value of the characteristic temperature $T_0$ was obtained for a generation wavelength of 1.2 μm [7]. Creation of a laser vertically emitting at a wavelength of 1.18 μm was reported in [8].

The major difficulty encountered in the development of InGaAsN/GaAs-based devices is deterioration of the optical quality of these structures with increasing molar fraction of nitrogen [9, 10]. To obtain devices with efficient lasing in the 1.3 μm range, one has to optimize the growth conditions and the structure parameters. Below, we report on the study of the properties of heterostructures with InGaAsN/GaAs quantum wells and show the possibility of obtaining a long-wavelength shift of the photoluminescence line toward the region of 1.3 μm.

The structures studied were grown by the molecular beam epitaxy (MBE) method on semi-insulating GaAs(100) substrates with the use of standard solid-state sources of the third group elements. A large-volume solid-state source with the cracking zone provided the flux of antimony molecules. The flux of active nitrogen radicals was obtained by passing gaseous nitrogen through a standard high-frequency plasma source. The source power varied from 75 to 150 W. Two types of samples were grown: 0.2-μm-thick bulky GaAsN layers and InGaAsN/GaAs quantum wells located in the middle of an 0.2-μm-thick GaAs layer bounded by short-period AlAs/GaAs superlattices providing a more efficient carrier collection in the quantum wells. The samples were grown under the standard MBE conditions providing the layer enrichment with antimony. The growth temperature of N-containing layers was 500°C. Photoluminescence was excited with an $Ar^+$

1063-7850/00/2605-0443$20.00 © 2000 MAIK "Nauka/Interperiodica"

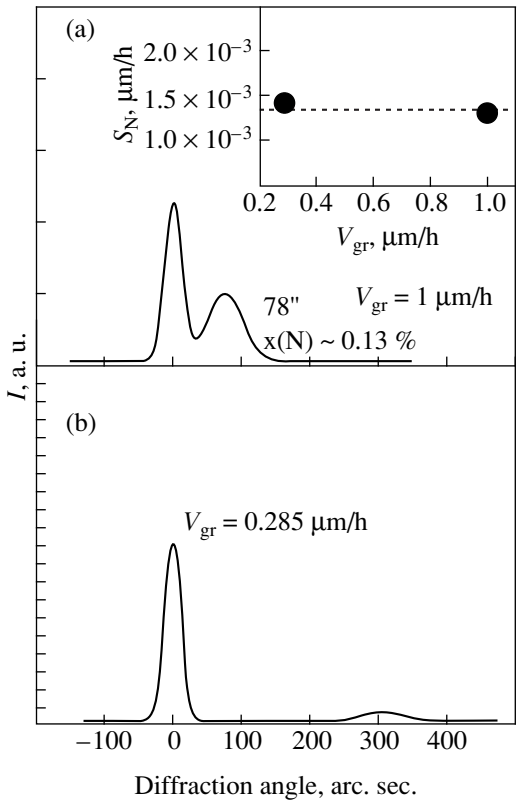


**Fig. 1.** The X-ray rocking curves of two GaAsN layers grown at different rates. Both samples were grown with the use of 75-W nitrogen source. In the inset: the rate of nitrogen incorporation $S_N$ versus growth rate of layers $V_{gr}$.

laser ($\lambda$ = 514.5 nm) and was detected with the aid of a cooled Ge-photodiode.

Figure 1 shows the X-ray rocking curves for two GaAsN layers grown at different rates. The plasma source power was maintained at a level of 75 W for both samples. The nitrogen concentration in the layer was calculated by the method described elsewhere [11] with the use of elastic constants reported in [12]. The nitrogen concentrations in the two layers studied were determined as 0.13 and 0.5%. It is seen that a decrease of the growth rate results in a higher nitrogen concentration in the GaAsN layer. Moreover, the rate of nitrogen incorporation into the lattice (determined as $S_N = V_{gr}[N]$, where $V_{gr}$ is the growth rate and [N] is the molar fraction of nitrogen in the layer) remained constant (see the inset in Fig. 1). These data are consistent with the results obtained in [13], where it was shown that the rate of nitrogen incorporation is almost independent of the growth rate.

We studied the properties of the structures with InGaAsN quantum wells characterized by different nitrogen content. Figure 2 shows the photoluminescence spectra of the samples with $In_{0.25}Ga_{0.75}AsN$ quantum wells grown with the use of nitrogen plasma sources of a different power. It is seen that the long-wavelength shift of the photoluminescence line with respect to the emission line of InGaAs quantum well equals 80 meV for the sample grown at the source power 75 W. Assuming that the nitrogen concentrations in the InGaAsN quantum well and in the GaAsN layer grown with the use of plasma sources of the same power are equal, we came to the conclusion that this shift of the photoluminescence line corresponds to the incorporation of ~0.5% of nitrogen. This value corresponds to a linear approximation of the bandgap width dependence on the nitrogen concentration in InGaAsN with the slope of 160 meV/(%N) that is close to the values indicated in [14]. Using this approximation, we

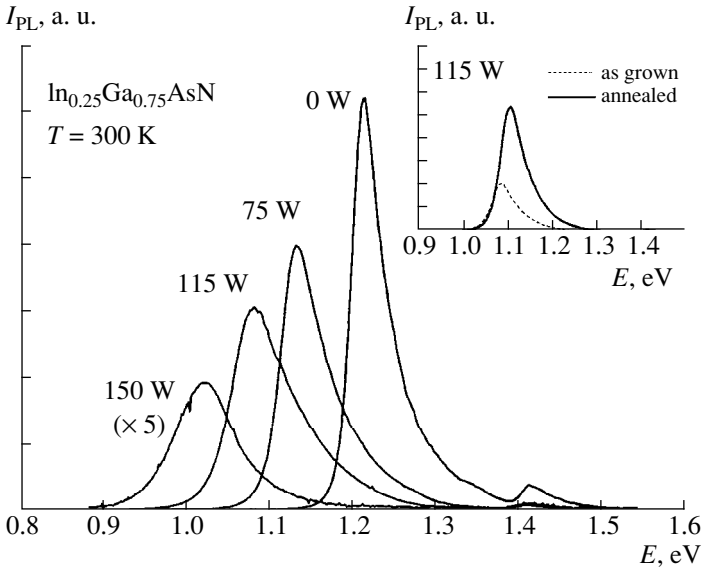


**Fig. 2.** Photoluminescence spectra of the structures with InGaAsN quantum wells grown with the use of the nitrogen plasma sources of different power (indicated at each spectrum). In the inset: the photoluminescence spectra of the structure grown with the use of a 115-W source prior to sample annealing and upon one-hour sample annealing at 700°C.

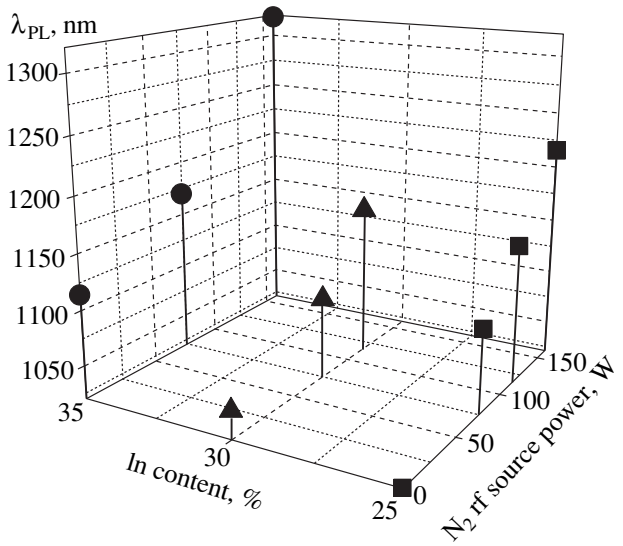


**Fig. 3.** Position of the maximum of the room-temperature photoluminescence line as function of the indium concentration in the quantum well and the nitrogen source power.

estimated the maximum nitrogen concentration in the samples as ~1.3%.

Thus, we managed to achieve a considerable longwavelength shift of the photoluminescence line of the InGaAs quantum well due to the incorporation of nitrogen. To provide for the emission at a wavelength of 1.3 μm, we have grown several series of samples with InGaAsN quantum wells having different indium and nitrogen concentrations. Figure 3 shows the dependence of the room-temperature emission wavelength on the indium and nitrogen concentrations in the quantum well. It is seen that, irrespective of the indium concentration in the quantum well, an increase of the plasma source power (and, hence, of the molar fraction of nitrogen in the quantum well) results in a monotonic longwave shift of the photoluminescence line. At the maximum nitrogen source power and a 35% indium concentration in the quantum well, the emission line is located at a wavelength of 1.32 μm. An increase of the molar fraction of nitrogen also results in the corresponding reduction in the room-temperature photoluminescence line intensity. This behavior is characteristic of InGaAsN and can be explained by the destruction of the surface by high-energy ions from the plasma source and also by an increase of the nonradiative recombination rate in the layers with high nitrogen concentrations [15].

The emission intensity in the InGaAsN structures can be increased by post-growth annealing of the samples [15]. We also studied the effect of post-growth annealing on the photoluminescence intensity. The samples were annealed in an antimony flow in the growth chamber. Our study showed that one-hour annealing at 650°C changes neither the photoluminescence intensity nor the emission wavelength. At the same time, annealing at 700°C resulted in an almost threefold increase of the photoluminescence intensity and a slight short-wavelength shift (by 20–25 meV for different structures) of the photoluminescence line (see the inset in Fig. 2). Thus, the photoluminescence can be intensified by the post-growth annealing, which is also necessary for the further improvement of the lasing characteristics of lasers based on InGaAsN/GaAs-structures [6].

Thus, we have studied the (In)GaAsN/GaAs heterostructures and managed to grow the structures with InGaAsN quantum wells characterized by the nitrogen concentration of about 1%. The emission at a wavelength of 1.32 μm was achieved at room temperature. It was also shown that post-growth annealing of the structure intensifies photoluminescence.

## ACKNOWLEDGMENTS

This study was supported by the State Program "Physics of Solid-State Nanostructures" of the Ministry of Science and Technologies of the Russian Federation (project no. 99-2034), the Russian Foundation for Basic Research, and the NATO Program "Science for Peace" (project no. SFP-972484).

## REFERENCES

1. A. F. Phillips, S. J. Sweeney, A. R. Adams, and P. J. A. Thijs, IEEE J. Sel. Top. Quantum Electron. **5**, 401 (1999).
2. D. L. Huffaker, G. Park, Z. Zou, *et al.*, Appl. Phys. Lett. **73**, 2564 (1998).
3. A. E. Zhukov, A. R. Kovsh, V. M. Ustinov, *et al.*, IEEE Photonics Technol. Lett. **11**, 1345 (1999).
4. M. Kondow, K. Uomi, A. Niwa, *et al.*, Jpn. J. Appl. Phys. **35**, 1273 (1996).
5. K. Nakahara, M. Kondow, T. Kitatani, *et al.*, IEEE Photonics Technol. Lett. **10**, 487 (1998).
6. A. Yu. Egorov, D. Bernklau, D. Livshits, *et al.*, Electron. Lett. **35**, 1643 (1999).
7. M. C. Larson, M. Kondow, T. Kitatani, *et al.*, IEEE Photonics Technol. Lett. **10**, 188 (1998).
8. M. Kondow, S. Nakatsuka, T. Kitatani, *et al.*, Jpn. J. Appl. Phys. **35**, 5711 (1996).
9. H. P. Xin and C. W. Tu, Appl. Phys. Lett. **72**, 2442 (1998).
10. S. Sato and S. Satoh, J. Cryst. Growth **192**, 381 (1998).
11. M. P. C. M. Krijn, Semicond. Sci. Technol. **6**, 27 (1991).
12. M. Kondow, K. Uomi, A. Niwa, *et al.*, Solid-State Electron. **41**, 209 (1997).
13. T. Kitatani, M. Kondow, K. Nakahara, *et al.*, J. Cryst. Growth **201**–**202**, 351 (1999).
14. G. Pozina, I. Ivanov, B. Monemar, *et al.*, J. Appl. Phys. **84**, 3830 (1998).
15. D. E. Mars, D. I. Babic, Y. Kaneko, *et al.*, J. Vac. Sci. Technol. B **17**, 1272 (1999).

*Translated by L. Man*